Can mesoscale eddy kinetic energy sources and sinks be inferred from sea surface height in the Agulhas Current region?

P. Tedesco[1,2], J. Gula[1,3], P. Penven[1], C. Ménesguen[1], Q. Jamet[4], C. Vic[1]

[1]Univ. Brest, CNRS, IRD, Ifremer, Laboratoire d'Océanographie Physique et Spatiale (LOPS), IUEM, 29280, Brest, France.
[2]University of Cambridge, Cambridge, UK.
[3]Institut Universitaire de France (IUF), Paris, France.
[4]INRIA, ODYSSEY group, Ifremer, Plouzané, France.

Key Points:

- We assess whether the mesoscale eddy energy flux divergence can be calculated from sea surface height in the Agulhas Current region
- Geostrophy allows a qualitative estimate of eddy energy advection, but not of eddy pressure work
- This favours the use of sea surface height, but challenges the founding approximations of an earlier paradigm

Corresponding author: Pauline Tedesco, `pfmt2@cam.ac.uk`

Abstract

Western boundaries have been suggested as mesoscale eddy graveyards, using a diagnostic of the eddy kinetic energy (EKE) flux divergence based on sea surface height (η). The graveyard's paradigm relies on the approximation of geostrophy — required by the use of η — and other approximations that support long baroclinic Rossby waves as the dominant contribution to the EKE flux divergence. However, a recent study showed an opposite paradigm in the Agulhas Current region using an unapproximated EKE flux divergence. Here, we assess the validity of the approximations used to derive the η-based EKE flux divergence using a regional numerical simulation of the Agulhas Current. The EKE flux divergence consists of the eddy pressure work (EPW) and the EKE advection ($AEKE$). We show that geostrophy is valid for inferring $AEKE$, but that all approximations are invalid for inferring EPW. A scale analysis shows that at mesoscale (L > $O(30)$ km), EPW is dominated by coupled geostrophic-ageostrophic EKE flux and that Rossby waves effect is weak. There is also a hitherto neglected topographic contribution, which can be locally dominant. $AEKE$ is dominated by the geostrophic EKE flux, which makes a substantial contribution (54%) to the net regional mesoscale EKE source represented by the EKE flux divergence. Other contributions, including topographic and ageostrophic effects, are also significant. Our results support the use of η to infer a qualitative estimate of the EKE flux divergence in the Agulhas Current region. However, they invalidate the approximations on mesoscale eddy dynamics that underlie the graveyard's paradigm.

Plain Language Summary

In the ocean, the most energetic motions are large-scale eddies with horizontal scales ranging from tens to hundreds of kilometers. These are major components of the ocean energy budget, and unravelling their lifecycles is crucial to improving our understanding of ocean dynamics. Although the generation of large-scale eddies is well documented, how their energy is dissipated remains uncertain. Based on satellite observations of the sea surface and approximations to the dynamics of large-scale eddies, it has been suggested that they decay at western boundaries of oceanic basins, thereby closing their lifecycle. However, based on different data and approximations, a recent study has suggested that large-scale eddies are predominantly generated in a specific western boundary region, such as the Agulhas Current. Our study explains which of the data (sea surface observations) or the assumed leading order dynamics (approximations) explains the opposite eddy energy sources and sinks shown by the two studies in the Agulhas Current region. Our results show that the use of sea surface observations is valid for qualitatively inferring the regional eddy energy source, but not the assumed leading order dynamics. This has implications for (1) our understanding and (2) study strategies of the energetics of large-scale eddies.

1 Introduction

Mesoscale eddies account for 80 % of the surface kinetic energy and are a key component of the global ocean energy budget (Wunsch, 2007; Ferrari & Wunsch, 2009; Müller et al., 2005). They have horizontal scales of the order of the 1^{st} Rossby deformation radius (Rd) or larger (Chelton et al., 2011). At these scales, the velocity field can be decomposed into a leading order geostrophic and a weaker ageostrophic component, following the quasi-geostrophic theory (Gill, 1982). Geostrophic flows are horizontally divergence-free flows — in a local approximation — dominated by the effects of rotation compared to advection (Rossby number : $Ro \ll 1$) and stratification compared to vertical shear (Richardson number : $Ri \gg 1$). Ageostrophic flows account for variations in the geostrophically balanced system. They are characterized by a large vertical component and the increasing effects of advection.

Mesoscale eddies are easily tracked by satellite altimetry, which measures sea surface height (η) and whose low-frequency component is an indirect measure of surface geostrophic currents. Satellite altimetry has shown that mesoscale eddies are ubiquitous in the oceans and that they are most energetic in western boundary currents and in the Antarctic Circumpolar Current (Ducet et al., 2000; Chelton et al., 2007, 2011). This identifies these regions as key to the global ocean energy budget.

Using satellite altimetry data, Zhai et al. (2010) suggested western boundaries as mesoscale eddy kinetic energy (EKE) sinks. In the energy budget, sources and sinks of eddy kinetic energy (EKE) are accounted for by the EKE flux divergence term (Harrison & Robinson, 1978). This term represents the rate of EKE transport done by: the work of pressure fluctuations (eddy pressure work; usually interpreted as the linear contribution from waves) and the nonlinear advection of EKE by mean and eddy flows. When ocean dynamics are in equilibrium, the EKE flux divergence indicates a net EKE source (>0) or sink (<0).

Zhai et al. (2010) explicitly developed a η-based diagnostic of the mesoscale eddy pressure work (linear component of the EKE flux divergence) using several approximations. Their diagnosis reduces to the linear contribution of the β-effect, corresponding in particular to the propagation of long Rossby waves. Figure 1a shows Zhai et al. (2010)'s version of the eddy pressure work in the Agulhas Current region, which they suggested to be the largest mesoscale EKE sink. The approximated η-based eddy pressure work indicates an almost uniform mesoscale EKE sink (<0) at the western boundary (WB; black domain), whose cumulative value is of $O(1)$ GW (Figure 1a).

Their result would establish the following paradigm: mesoscale eddies originate almost everywhere in the ocean, propagate westward at about the speed of long baroclinic Rossby waves, and decay at western boundaries, probably through direct energy routes to dissipation, channeled by topography (Gill et al., 1974; Zhai et al., 2010; Chelton et al., 2011; Evans et al., 2022). This scenario is supported in regions free of western boundary currents, by *in situ* measurements and idealized numerical simulations (Evans et al., 2020; Z. Yang et al., 2021; Evans et al., 2022). However, in regions containing western boundary currents, model-based studies suggest more complex mesoscale eddy dynamics. Western boundaries are hotspots for mesoscale eddy generation due to instabilities of the western boundary currents (Halo et al., 2014; Kang & Curchitser, 2015; Gula et al., 2015; Y. Yang & Liang, 2016; Yan et al., 2019; Li et al., 2021; Jamet et al., 2021; Tedesco et al., 2022).

In particular, a recent study has shown that the Agulhas Current region is a mesoscale EKE source using an unapproximated EKE flux divergence performed from a model (Tedesco et al., 2022). Figure 1d,e shows the unapproximated eddy pressure work and advection of EKE (forming the EKE flux divergence) computed from 3-dimensional modeled mesoscale velocities (Tedesco et al., 2022). Both unapproximated terms differ significantly from the approximated η-based eddy pressure work, with their magnitudes being larger of an order and their scale patterns smaller (Figure 1d,e). In the WB region of the Agulhas

Current, the two unapproximated terms are the most intense on the shelf — over a band narrower than the WB width — and have locally comparable magnitudes. Their cumulative value represents a mesoscale EKE source (>0), whose main contribution is due to the advection of EKE.

The opposite mesoscale EKE sources and sinks supported in the Agulhas Current region by the different versions of the EKE flux divergence (Figure 1a,d,e reproducing Zhai et al., 2010; Tedesco et al., 2022), challenge (1) the hypothesis that long baroclinic Rossby waves are the main contributors to the mesoscale EKE flux divergence, and thus (2) the approximations used to derive the η-based term. In this study, we focus on explaining the differences between the approximated η-based and the unapproximated model-based EKE flux divergence in the Agulhas Current region. We discuss below the approximations used by Zhai et al. (2010) and their implications:

(i) **Mesoscale EKE flux divergence is mainly due to geostrophic flows**
The geostrophic approximation is required when using satellite altimetry data. Geostrophy is a good approximation to infer mesoscale eddy velocities, which have small Rossby numbers ($Ro = O(\ll 0.05)$; Chelton et al., 2011). However, the use of geostrophic velocities to infer the mesoscale EKE flux divergence — a tendency term of the EKE budget that represents the rate of spatial redistribution of the mesoscale EKE reservoir (Harrison & Robinson, 1978) — is a separate issue.

(ii) **The vertical structure of mesoscale eddies is represented by the 1st baroclinic mode**
The sea surface height (η) is usually interpreted as primarily reflecting surface-intensified vertical structures represented by the 1st baroclinic mode. However, the mesoscale EKE reservoir is represented by the combination of the barotropic and 1st baroclinic modes (Wunsch, 1997; Smith & Vallis, 2001; Venaille et al., 2011). The partitioning between the two vertical modes varies regionally, from being close to equipartition to being dominated by one of the modes (Tedesco et al., 2022; Yankovsky et al., 2022). The contributions of the barotropic and 1st baroclinic modes to the mesoscale EKE flux divergence remain unknown to our knowledge. Their individual contributions can possibly transport EKE in a decoupled (coupled) manner, which would then compensate (accumulate) when considering the EKE flux divergence for the mesoscale reservoir.

(iii) **Mesoscale EKE flux interactions with topography are weak**
The approximation of weak topographic interactions is equivalent to assuming that the mesoscale EKE flux has spatial variations larger than those of topography (Zhai et al., 2010). This approximation is challenged by (1) the large topographic gradients at western boundaries ($1 \cdot 10^{-2} \pm 2 \cdot 10^{-2}$ in the Agulhas Current region) and (2) the strong topographic control on mesoscale eddy dynamics at western boundaries. Topography controls the triggering of current' instabilities that generate mesoscale eddies (Lutjeharms, 2006; Gula et al., 2015) and helps to channel energy transfers between mesoscale eddies and other types of flow (Adcock & Marshall, 2000; Nikurashin & Ferrari, 2010; Evans et al., 2020; Perfect et al., 2020; Tedesco et al., 2022). The contribution of topography to the mesoscale EKE flux divergence remains, to our knowledge, an open question.

In summary, opposing paradigms of mesoscale eddy dynamics are supported by two versions of the diagnosis of the EKE flux divergence in the western boundary region of the Agulhas Current (Zhai et al., 2010; Tedesco et al., 2022). The two diagnoses differ in method (η field measured by satellite altimetry *vs.* modeled 3-dimensional velocities) and assumed leading order contribution to the EKE flux divergence (long baroclinic Rossby waves as a result of approximations (i), (ii) and (iii) *vs.* no approximations to account for geostrophic, ageostrophic and topographic contributions acting on the barotropic and 1st

baroclinic mode). The two contradictory diagnoses of mesoscale EKE source and sink suggest that either the method or the approximations lead to a misestimation of the mesoscale EKE flux divergence. This raises questions about the main contributions to the dynamics of the mesoscale eddy energy reservoir, and consequently, about strategies for studying mesoscale eddies. Open questions include: What are the main contributions – among geostrophic and ageostrophic effects, barotropic and 1^{st} baroclinic modes, and topographic contribution – to the eddy pressure work and advection of EKE? What are the implications for inferring the mesoscale EKE flux divergence using the η field? We focus in particular on determining whether approximation (i) of geostrophy is valid, as it is the only one formally required for the use of satellite altimetry to infer the mesoscale EKE flux divergence.

In the present study, we use a numerical simulation to evaluate the validity of approximation (i) for inferring the mesoscale EKE flux divergence in the region of the Agulhas Current. Our study is organized as follows. Unapproximated and η-based expressions of the eddy pressure work and advection of EKE (which form the EKE flux divergence) are presented in section 2. The regional numerical simulation is presented in section 3. The unapproximated and η-based versions of the eddy pressure work and advection of EKE are evaluated in sections 4, 5 and 6. Finally, we discuss our results in the larger context of altimetry-based diagnosis of mesoscale eddy dynamics at western boundaries in section 7.

2 Theory

In this section we present the modal EKE flux divergence. First, we present the theoretical framework of the vertical modes. Then, we define the unapproximated expression of the modal EKE flux divergence, which consists of the eddy pressure work (EPW) and the advection of EKE ($AEKE$). Finally, we define the η-based expressions of EPW and $AEKE$.

2.1 Vertical modes

A convenient approach to describe the vertical structure of mesoscale motions is the modal decomposition using traditional vertical modes (Gill, 1982). The vertical structure of the mesoscale EKE reservoir corresponds to the combination of the barotropic and 1^{st} baroclinic modes (Wunsch, 1997; Smith & Vallis, 2001; Venaille et al., 2011; Tedesco et al., 2022), which represents surface-intensified vertical structures energised to the bottom.

The vertical modes ϕ_n for the horizontal velocity ($\mathbf{u}$) and the dynamical pressure (p) are the eigenfunctions solution of the Sturm-Liouville problem (Eq. 1), using linearized free-surface ($|\frac{\partial}{\partial z}\phi_n|_{z=\eta} = |\frac{-\overline{N^2}}{g}\phi_n|_{z=\eta}$) and flat-bottom boundary conditions ($|\frac{\partial}{\partial z}\phi_n|_{z=-H} = 0$) :

$$\frac{\partial}{\partial z}\left(\frac{1}{N^2}\frac{\partial}{\partial z}\phi_n\right) + \frac{1}{c_n^2}\phi_n = 0 \tag{1}$$

with N^2 the time-averaged buoyancy frequency, g the acceleration of gravity and $c_n^2 = \frac{1}{n\pi}\int_{-H}^{\eta} N(\mathbf{x}, z)\ dz$ the eigenvalues of the vertical modes.
The modal base ϕ_n satisfies the orthogonality condition :

$$\int_{-H}^{\eta} \phi_m \phi_n \ dz = \delta_{mn} h \tag{2}$$

with δ_{mn} the usual Kronecker symbol and $h = \eta + H$ the water column depth.
The dynamical variables are projected onto n vertical modes as follows :

$$[\mathbf{u}_n(\mathbf{x}, t), \frac{1}{\rho_0}p_n(\mathbf{x}, t)] = \frac{1}{h}\int_{-H}^{\eta}[\mathbf{u}(\mathbf{x}, z, t), \frac{1}{\rho_0}p(\mathbf{x}, z, t)]\phi_n(\mathbf{x}, z)\ dz \tag{3}$$

with $\mathbf{u}_n$ and p_n the modal amplitudes of the horizontal velocity ($\mathbf{u}$) and dynamical pressure (p) and ρ_0 the reference density value.
The vertical modes are related to horizontal scales via c_n^2, which are good approximations of the Rossby baroclinic deformation radii : $Rd_{n\geq 1} = \frac{c_n}{|f|}$ (Chelton et al., 1998), with f the Coriolis parameter.

2.2 Unapproximated modal *EKE* flux divergence

2.2.1 *EKE* flux divergence in the *EKE* budget

The modal EKE flux divergence is a term of the modal EKE budget. A comprehensive modal EKE budget has been derived in Tedesco et al. (2022), inspired from the budget derived in the context of internal tides (Kelly, 2016). The modal EKE budget reads as follows:

$$\underbrace{\mathbf{u}'_n \cdot (\rho_0 h \frac{\partial}{\partial_t}\mathbf{u}'_n)}_{Time\ rate} + \underbrace{\underbrace{\nabla_H \cdot \int_{-H}^{\eta} \mathbf{u}'_n p'_n \phi_n^2 \ dz}_{Eddy-pressure\ work\ (EPW)} + \underbrace{\frac{\rho_0}{2}\nabla_H \cdot \int_{-H}^{\eta} \mathbf{u}_n \phi_n ||\mathbf{u}'_n \phi_n||^2 \ dz}_{Advection\ of\ EKE\ (AEKE)}}_{EKE\ flux\ divergence\ (EPW+AEKE)}$$
$$= \sum \left(\underbrace{S_n}_{EKE\ sources} + \underbrace{D_n}_{EKE\ sinks} \right) \tag{4}$$

Terms are time-averaged and the primes indicate fluctuations relative to the time-average. The dynamical pressure ($p(\mathbf{x}, z, t)$) is derived from the *in situ* density ($\rho(\mathbf{x}, z, t)$) from which the background density profile ($\widetilde{\rho}(z)$, defined as the spatial and temporal average of the *in situ* density) has been subtracted.

The EKE flux divergence corresponds to the rate of EKE spatial transport. When integrated over a domain, the EKE flux divergence corresponds to the transport across the domain boundaries. A positive (negative) sign indicates that outgoing (incoming) flux dominate the incoming (outgoing) flux. At equilibrium, the time rate of EKE (Eq. 4) is negligible. The EKE flux divergence is therefore equal to the sum of the EKE sources and sinks accounted for in the right-hand side of the modal EKE budget (S_n and D_n in Eq. 4). A positive (negative) EKE flux divergence thus represents a net EKE source (sink) that is then transported away (has been transported in).

The EKE flux divergence consists of two contributions: the eddy pressure work (EPW; Eq. 4) and the advection of EKE by the mean and eddy flows ($AEKE$; Eq. 4) (Harrison & Robinson, 1978). EPW is the only contribution to the EKE flux divergence in the context of linear theories of internal waves (Kelly et al., 2010, 2012; Kelly, 2016) and of Rossby waves (Masuda, 1978). It is also the main contribution for interior-ocean dynamics (Harrison & Robinson, 1978). $AEKE$ can contribute significantly to the EKE flux divergence and can be equivalent to EPW in regions of high variability (Harrison & Robinson, 1978; Capó et al., 2019; Tedesco et al., 2022).

Here, we study the EKE flux divergence for the mesoscale reservoir over the period 1995-2004. We define the mesoscale EKE flux divergence as the sum of the barotropic ($n = 0$) and 1^{st} baroclinic ($n = 1$) contributions: $EPW_{n=0-1}$ and $AEKE_{n=0-1}$. To simplify notations, we refer to the mesoscale terms as EPW and $AEKE$ in the following. The modeled mesoscale eddy dynamics over the period 1995-2004 is in equilibrium. The smallness of the time rate of EKE (Eq. 4) has been asserted for the period 1995-1999 in Tedesco et al. (2022). It is even smaller for the period 1995-2004 considered in this study.

2.2.2 Contributions to the EKE flux divergence

EPW and $AEKE$ (Eq. 4) can be written as the sum of the contributions of EKE flux ($A + B$ in Eq. 5, 6) and EKE flux interacting with topographic gradients (C in Eq. 5, 6) as follows:

$$\begin{aligned} EPW = & \underbrace{\underbrace{\int_{-H}^{\eta} p_n'\phi_n \nabla_H \cdot (\mathbf{u}_n'\phi_n)\, dz}_{velocity\ divergence\ (\mathbf{A})} + \underbrace{\int_{-H}^{\eta} (\mathbf{u}_n'\phi_n) \cdot \nabla_H (p_n'\phi_n)\, dz}_{work\ of\ eddy\ pressure\ shear\ (\mathbf{B})}}_{EKE\ flux\ (\mathbf{A+B})} \\ & + \underbrace{\nabla_H \eta \cdot \left|\mathbf{u}_n' p_n' \phi_n^2\right|_{z=\eta} + \nabla_H H \cdot \left|\mathbf{u}_n' p_n' \phi_n^2\right|_{z=-H}}_{topographic-contribution\ (\mathbf{C})} \end{aligned} \tag{5}$$

$$\begin{aligned} AEKE = & \underbrace{\underbrace{\frac{\rho_0}{2}\int_{-H}^{\eta} ||\mathbf{u}_n'\phi_n||^2 \nabla_H \cdot (\mathbf{u}_n\phi_n)\, dz}_{velocity\ divergence\ (\mathbf{A})} + \underbrace{\frac{\rho_0}{2}\int_{-H}^{\eta} (\mathbf{u}_n\phi_n) \cdot \nabla_H ||\mathbf{u}_n'\phi_n||^2\, dz}_{work\ of\ EKE\ shear\ (\mathbf{B})}}_{EKE\ flux\ (\mathbf{A+B})} \\ & + \underbrace{\frac{\rho_0}{2}\nabla_H \eta \cdot \left|\mathbf{u}_n\phi_n ||\mathbf{u}_n'\phi_n||^2\right|_{z=\eta} + \frac{\rho_0}{2}\nabla_H H \cdot \left|\mathbf{u}_n\phi_n ||\mathbf{u}_n'\phi_n||^2\right|_{z=-H}}_{topographic-contribution\ (\mathbf{C})} \end{aligned} \tag{6}$$

The EKE flux term ($A + B$; Eq. 5, 6) consists of a velocity divergence contribution (A) and an eddy pressure shear work for EPW (B in Eq. 5) and an EKE shear work for $AEKE$ (B in Eq. 6). From their analytical expressions, it can be deduced that the importance of geostrophic and ageostrophic effects varies between A and B. The velocity divergence contributions (A) mainly account for ageostrophic effects, since geostrophic velocities are horizontally divergent-free. The only geostrophic effects in A are due to geostrophic velocities expressed in the β-plan (Cushman-Roisin & Beckers, 2011). The geostrophic A-contributions acting on EPW and $AEKE$ are thus reduced to EKE flux driven by the β-effect. In the case of EPW (Eq. 5), the β-driven linear EKE flux corresponds to long baroclinic Rossby waves and was assumed by Zhai et al. (2010) to be the primary contributor to EPW, and subsequently to the EKE flux divergence. The work contribution (B) accounts for geostrophic and ageostrophic effects in different proportions for EPW and $AEKE$. For EPW (Eq. 5), the B-contribution is exclusively due to ageostrophic effects. Indeed, geostrophic velocities are orthogonal to the eddy pressure shear resulting in the cancellation of the eddy pressure shear work. For $AEKE$ (Eq. 6), the B-contribution accounts for both geostrophic and ageostrophic effects. Geostrophic velocities are in the same direction than the EKE shear, resulting in a non-null work.

The topographic-contribution (C; Eq. 5,6) acting on EPW and $AEKE$ represents the interactions of EKE flux with topography and sea surface height gradients. It can be reduced to the contribution of topography gradients, which are much larger than η gradients ($||\nabla_H \eta|| = O(10^{-4})||\nabla_H H||$). The analytical expression of C does not allow the contribution of geostrophic or ageostrophic effects to be readily separated.

2.3 Approximated η-based modal EKE flux divergence

In the following, we present the η-based expressions of EPW and $AEKE$ accounting for approximation (i). We also present two other η-based expressions of EPW accounting for approximations (ii) and (iii). The main expressions of EPW and $AEKE$ discussed in this study are listed in Tables 1 and 2.

2.3.1 Approximations (i) of geostrophic velocities ($EPW_{(i)}$ and $AEKE_{(i)}$)

Approximation (i) of geostrophy is required by the use of η to infer the EKE flux divergence. EPW and $AEKE$ are written as $EPW_{(i)}$ and $AEKE_{(i)}$ when using modal geostrophic velocities (Table 1, 2). Modal geostrophic velocities are expressed from η fields, modulated to account for the fraction of the different vertical modes with $\lambda_n = \frac{\eta_n}{\eta}$ and $\alpha_n = \frac{\eta'_n}{\eta'}$, as follows:

$$\mathbf{u}_{g,n}\phi_n = \mathbf{k} \wedge \frac{g}{f}\nabla_H \left(\frac{\phi_n}{|\phi_n|_{z=0}} \lambda_n \eta \right) \tag{7}$$

$$\mathbf{u}'_{g,n}\phi_n = \mathbf{k} \wedge \frac{g}{f}\nabla_H \left(\frac{\phi_n}{|\phi_n|_{z=0}} \alpha_n \eta' \right) \tag{8}$$

Approximation (i) of geostrophy has a larger impact on EPW than on $AEKE$. $EPW_{(i)}$ (Table 1) reduces to a linear EKE flux driven by the β-effect ($A1$) and two topographic contributions, one acting on the β-driven EKE flux ($A2$) and the other acting on geostrophic EKE flux (C). $AEKE_{(i)}$ (Table 2) includes the β-effect (A), the geostrophic EKE shear work (B) and a topographic contribution acting on the geostrophic EKE flux (C).

2.3.2 Approximations (ii) and (iii) ($EPW_{(i,ii)}$ and $EPW_{(i,ii,iii)}$)

The η-based version of EPW defined by Zhai et al. (2010) relies on the additional approximations (ii) and (iii), which are not formally required by the use of η to infer the EKE flux divergence. Approximations (ii) and (iii) therefore lead to approximated versions of the η-based EPW: $EPW_{(i,ii)}$ and $EPW_{(i,ii,iii)}$ (Table 1).

Table 1: Summary of the unapproximated and η-based versions of the eddy pressure work (EPW).

Acronyms	Analytical expressions	Descriptions
EPW	$\underbrace{\nabla_H \cdot \int_{-H}^{\eta} \mathbf{u}'_n p'_n \phi_n^2 \, dz}_{(A+B+C)}$	unapproximated mesoscale eddy pressure work
$EPW_{(i)}$	$\underbrace{-\frac{\beta \rho_0 g^2}{2f^2} \frac{\partial}{\partial x} \left(\frac{\int_{-H}^{\eta} \phi_n^2 \, dz}{\lvert\phi_n^2\rvert_{z=0}} \alpha_n^2 \eta'^2 \right)}_{\beta-contribution\ (A1)} + \underbrace{\frac{\beta \rho_0 g^2}{2f^2} \frac{\partial H}{\partial x} \frac{\lvert\phi_n^2\rvert_{z=-H}}{\lvert\phi_n^2\rvert_{z=0}} \alpha_n^2 \eta'^2}_{\beta-driven\ topographic-contribution\ (A2)}$ $+ \underbrace{\frac{\rho_0 g^2}{2f} \nabla_H H \cdot \mathbf{k} \wedge \nabla_H \left(\frac{\lvert\phi_n^2\rvert_{z=-H}}{\lvert\phi_n^2\rvert_{z=0}} \alpha_n^2 \eta'^2 \right)}_{topographic-contribution\ (C)}$, with $\alpha_n = \frac{\eta'_n}{\eta'}$	unapproximated η-based version of mesoscale eddy pressure work (use of approximation (i))
$EPW_{(i,ii)}$	$\underbrace{-\frac{\beta \rho_0 g^2}{2f^2} \frac{\partial}{\partial x} \left(\frac{\int_{-H}^{\eta} \phi_1^2 \, dz}{\lvert\phi_1^2\rvert_{z=0}} \eta'^2 \right)}_{\beta-contribution\ (A1)} + \underbrace{\frac{\beta \rho_0 g^2}{2f^2} \frac{\partial H}{\partial x} \frac{\lvert\phi_1^2\rvert_{z=-H}}{\lvert\phi_1^2\rvert_{z=0}} \eta'^2}_{\beta-driven\ topographic-contribution\ (A2)}$ $+ \underbrace{\frac{\rho_0 g^2}{2f} \nabla_H H \cdot \mathbf{k} \wedge \nabla_H \left(\frac{\lvert\phi_1^2\rvert_{z=-H}}{\lvert\phi_1^2\rvert_{z=0}} \eta'^2 \right)}_{topographic-contribution\ (C)}$	approximated η- based version of mesoscale eddy pressure work (use of approximations (i) and (ii))
$EPW_{(i,ii,iii)}$	$\underbrace{-\frac{\beta \rho_0 g^2}{2f^2} \frac{\partial}{\partial x} \left(\frac{\int_{-H}^{\eta} \phi_1^2 \, dz}{\lvert\phi_1^2\rvert_{z=0}} \eta'^2 \right)}_{\beta-contribution\ (A1)}$	approximated η-based version of mesoscale eddy pressure work defined by Zhai et al. (2010) (use of approximations (i), (ii) and (iii))

Table 2: Summary of the unapproximated and η-based versions of the advection of mesoscale EKE ($AEKE$).

Acronyms	Analytical expressions	Descriptions
$AEKE$	$\underbrace{\frac{\rho_0}{2}\nabla_H \cdot \int_{-H}^{\eta} \mathbf{u}_n\phi_n \lvert\lvert \mathbf{u}'_n\phi_n \rvert\rvert^2 \, dz}_{(A+B+C)}$	unapproximated advection of mesoscale EKE
$AEKE_{(i)}$	$\underbrace{-\frac{\beta\rho_0 g}{2f^2}\int_{-H}^{\eta} \lvert\lvert \mathbf{u}'_{g,n}\phi_n \rvert\rvert^2 \frac{\partial}{\partial x}\left(\frac{\phi_n}{\lvert\phi_n\rvert_{z=0}}\lambda_n\eta\right) \, dz}_{velocity\ divergence\ (A)} +$ $\underbrace{\frac{\rho_0}{2}\int_{-H}^{\eta} (\mathbf{u}_{g,n}\phi_n)\cdot\nabla_H \lvert\lvert \mathbf{u}'_{g,n}\phi_n \rvert\rvert^2 \, dz}_{work\ of\ EKE\ shear\ (B)}$ $+\underbrace{\frac{\rho_0}{2}\nabla_H H \cdot \left\lvert \mathbf{u}_{g,n}\phi_n \lvert\lvert \mathbf{u}'_{g,n}\phi_n \rvert\rvert^2 \right\rvert_{z=-H}}_{topographic-contribution\ (C)}$, with $\lambda_n = \frac{\eta_n}{\eta}$	unapproximated η-based version of advection of mesoscale EKE (use of approximation (i))

2.3.2.1 Approximation (ii) of sea surface height primarily reflecting the 1^{st} baroclinic mode ($EPW_{(i,ii)}$)

$EPW_{(i,ii)}$ is written as $EPW_{(i)}$, but assumes that modal geostrophic velocities expressed from η reflect only the 1^{st} baroclinic mode (Table 1), using $\alpha_n \sim \alpha_1 \sim 1$, as follows:

$$\mathbf{u}'_{g,1}\phi_1 = \mathbf{k} \wedge \frac{g}{f}\nabla_H \left(\frac{\phi_1}{|\phi_1|_{z=0}} \eta' \right) \tag{9}$$

2.3.2.2 Approximation (iii) of weak topographic-contributions ($EPW_{(i,ii,iii)}$)

$EPW_{(i,ii,iii)}$ ($A1$; Eq. 10) is derived from $EPW_{(i,ii)}$ ($A1 + A2 + C$), assuming that topographic contributions ($A2$ and C) are negligible:

$$EPW_{(i,ii,iii)} = \underbrace{-\frac{\beta\rho_0 g^2}{2f^2}\frac{\partial}{\partial x}\left(\frac{\int_{-H}^{\eta} \phi_1^2 \, dz}{|\phi_1^2|_{z=0}} \eta'^2 \right)}_{\beta-contribution\ (\mathbf{A1})} \tag{10}$$

$EPW_{(i,ii,iii)}$ ($A1$; Table 1) corresponds to a β-driven linear EKE flux acting on the 1^{st} baroclinic mode, which represents the contribution of long baroclinic Rossby waves to the EKE flux divergence. $EPW_{(i,ii,iii)}$ is the approximated η-based version of EPW used in Zhai et al. (2010), which established the paradigm of mesoscale eddies decay at western boundaries.

This study focuses on evaluating the main contributions to EPW and $AEKE$ (which form the EKE flux divergence) in the Agulhas Current region (Figure 1d,e). To do this, we evaluate the impacts of approximations (i), (ii) and (iii) on EPW and of approximation (i) on $AEKE$. We start our analysis by EPW, which is the term explicitly discussed in Zhai et al. (2010). We first evaluate the validity of approximations (ii) and (iii) to infer the η-based EPW (*cf.* section 4). This allows us to define $EPW_{(i)}$ — the unapproximated η-based EPW — which we then use to evaluate the validity of approximation (i) of geostrophy to infer the unapproximated EPW (*cf.* section 5). We next expand our analysis to $AEKE$ (*cf.* section 6). This term dominates the cumulative value of the EKE flux divergence in the WB region (Figure 1e) and is not explicitly discussed in Zhai et al. (2010).

Evaluation of the effects of approximations (i), (ii) and (iii) on EPW provides information on the elements of mesoscale eddy dynamics that invalidate the paradigm of mesoscale eddy graveyard in the Agulhas Current region. In addition, evaluation of the effect of approximation (i) of geostrophy on EPW and $AEKE$ provides information on the possibility of using η to infer EKE flux divergence.

3 Method

In this section, we present and evaluate the regional numerical simulation of the Agulhas Current. We first present the numerical set-up and observations used in this study. We then evaluate the modeled mesoscale eddy dynamics against observations. The modeled mesoscale EKE in the Agulhas Current region has already been evaluated against satellite altimetry data in Tedesco et al. (2022). Here, we evaluate the η-based version of EKE flux divergence defined by Zhai et al. (2010) ($EPW_{(i,ii,iii)}$) derived from our numerical simulation against one derived from observations. The computation of $EPW_{(i,ii,iii)}$ ($A1$; Table 1) requires the computation of vertical modes — based on the time-averaged stratification (N^2) — and η.

3.1 Numerical model

The regional numerical simulation of the Agulhas Current was performed using the Coastal and Regional COmmunity (CROCO) model. It is a free surface model, based on ROMS (Shchepetkin & McWilliams, 2005), which solves the primitive equations in the Boussinesq and hydrostatic approximations using a terrain following coordinate system (Debreu et al., 2012). The numerical simulation is presented in details in Tedesco et al. (2022). The simulation has a horizontal resolution of dx $\sim$ 2.5 km and 60 vertical levels. It encompasses the Agulhas Current region from its source (north of the Natal Bight at 27°S) to the Agulhas Retroflection (at $\sim$ 37°S), from where it becomes the Agulhas Return Current.Boundary conditions are supplied by two lower-resolution grids (dx $\sim$ 22.5 km and 7.5 km, respectively covering most of the South Indian Ocean and its western part).

Vertical modes are derived from the time-averaged stratification over the period 1995-2004, computed from the modeled daily-averaged temperature and salinity.

3.2 Observations

The WOCE (World Ocean Circulation Experiment) climatology provides *in situ* temperature and salinity fields at a global scale for monthly compositing means at the horizontal resolution of 1° (Gouretski & Koltermann, 2004).

Altimetric data are mapped on a regular 1/4°-grid by AVISO (Archiving, Validation and Interpretation of Satellite Oceanographic data) and provide global scale η field for weekly compositing means. We focus on a subset of data over the Agulhas Current region (15°E - 34°E and 27°S - 40°S) for the period 1995-2004.

3.3 Observed and modeled mesoscale EKE sources and sinks from $EPW_{(i,ii,iii)}$

Figure 1a-c shows $EPW_{(i,ii,iii)}$ (Table 1) in the Agulhas Current region calculated from observations and the model. Observed and modeled $EPW_{(i,ii,iii)}$ show patterns in fairly good agreement in the Agulhas Current region. $EPW_{(i,ii,iii)}$ is most intense at the Retroflection and along the Agulhas Return Current (O(0.1-0.5) W m^{-2}), where it has patterns alterning positive and negative signs. It is less intense along the Agulhas Current and in the Subgyre (O(0.01-0.1) W m^{-2}), where it has more uniform patterns.

We define the western boundary (WB) region as extending from north of the Natal Bight ($\sim$ 27°S) to the African tip ($\sim$ 37°S), over a typical width for a western boundary current of about 150 km (black region in Figure 1). In the WB region, $EPW_{(i,ii,iii)}$ is roughly uniformly negative, indicating an EKE sink of cumulative magnitude $O(1)$ GW. This is consistent with the EKE sink emphasised by Zhai et al. (2010) at the western boundary of the South Indian Ocean (poleward of $10°S$).

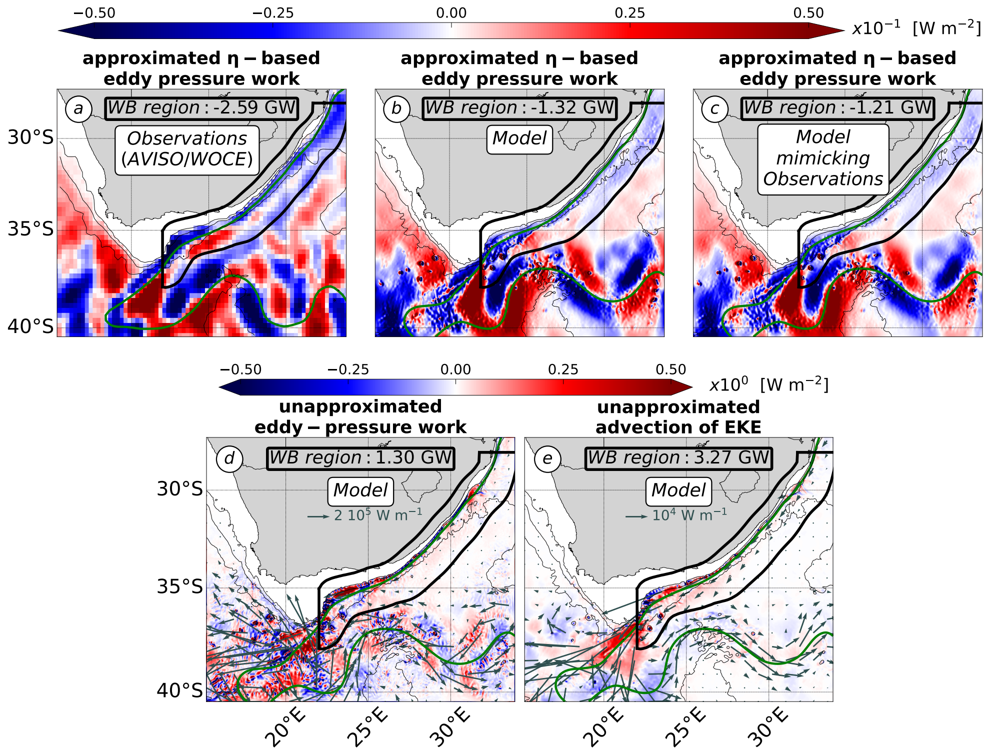

Figure 1: Different versions of the mesoscale EKE flux divergence (formed by eddy pressure work and advection of EKE) [W m^{-2}] in the Agulhas Current region. (a-c) Approximated η-based eddy pressure work performed from (a) observations (AVISO and WOCE data) following Zhai et al. (2010) and (b,c) a numerical simulation (built upon the CROCO model), at (b) the resolution of the simulation (dx $\sim$ 2.5 km) and (c) a coarsened resolution mimicking the resolution of observations.(d,e) Unapproximated model-based (d) eddy pressure work and (e) advection of EKE at the resolution of the simulation (dx $\sim$ 2.5 km). Note the different colorbar ranges between panels (a, b, c) and panels (d, e). Black area denotes the WB region. The cumulative terms in the WB region are in [GW] (10^9 W). Green contours denote the 0.25 m isoline of time-averaged η and black contours denote 1000 m and 3000 m isobaths.

Observed and modeled $EPW_{(i,ii,iii)}$s differ mainly in the magnitude of the EKE sinks that they depict in the WB region. There is about a twofold decrease in the model compared to the observations (Figure 1a-c). The difference in magnitude is not explained by the coarser horizontal resolution of AVISO data (effective horizontal resolution of $O(100)$ km; Chelton et al., 2011) compared to the model (effective horizontal resolution of 25 km; following Soufflet et al., 2016). The twofold decrease in the model is also present when using smoothed modeled η, with a length scale of 100 km to mimic the altimetry data processing done by AVISO (Figure 1c). This indicates that the net EKE sink in the WB region is robust to altimetry data processing and that horizontal scales $<$ $O(100)$ km do not contribute significantly to $EPW_{(i,ii,iii)}$. The difference in magnitude could be explained by too weak a forcing of remotely generated eddies in the model. The numerical simulation is forced at the boundaries by a parent simulation (dx $\sim$ 7.5 km), which resolves mesoscale eddies of scales 50 km–100 km, but underestimate their amplitude. See Appendix A for details of the evaluation of the amplitude of the modeled mesoscale eddy field against satellite altimetry data. This underestimation in the model is likely due to a too weak inverse cascade at smaller scales, which have been shown to substantially energize the mesoscale eddy energy reservoir in the Agulhas Current region (Schubert et al., 2020). Note that the magnitude of the cumulative EKE flux is sensitive to the definition of the WB region. Our definition of the WB region best captures the EKE sink shown by the modeled and observed $EPW_{(i,ii,iii)}$. However, the observed EKE sink extends further south of the WB region (Figure 1a), while the modeled one is fully encompassed by the WB region — with its southern face closely following the 0 W m^{-2} isoline — (Figure 1c,d).

The fairly good agreement between modeled and observed EKE reservoirs (Tedesco et al., 2022) and $EPWs_{(i,ii,iii)}$ (Figure 1a-c), indicates that our numerical simulation reliably represents the mesoscale eddy dynamics, at least as inferred from satellite altimetry data. Our numerical simulation is therefore suitable to evaluate the leading order contribution of the EKE flux divergence, and subsequently to explain the opposing paradigms between η-based and unapproximated diagnoses in this region.

4 Approximated and unapproximated η-based EPWs ($EPW_{(i,ii,iii)}$ and $EPW_{(i)}$)

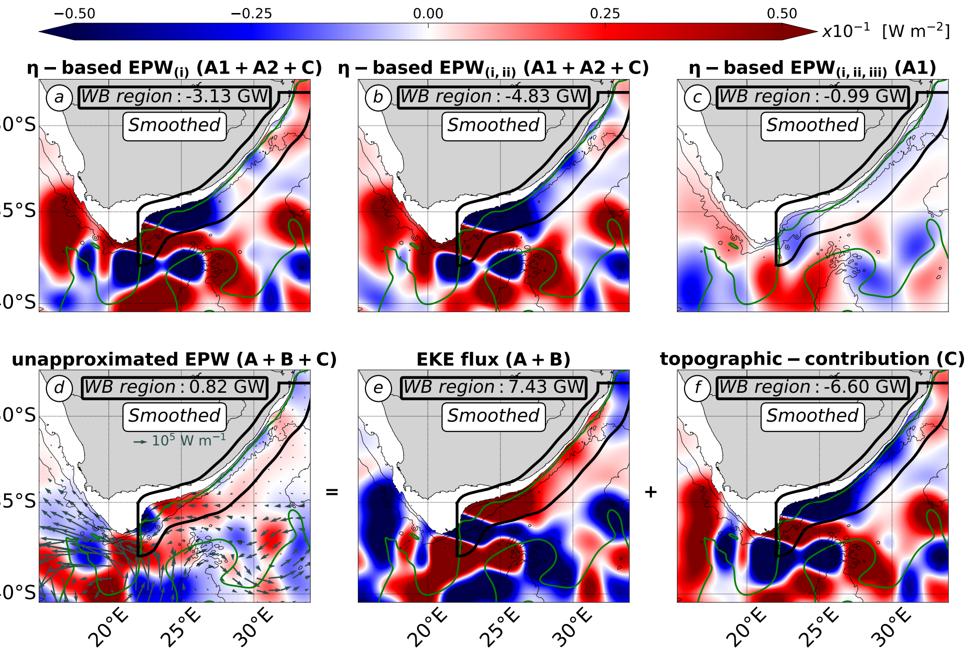

Figure 2: η-based and unapproximated EPWs [W m^{-2}] (Table 1). (a-c) Versions of η-based EPW, including (a) $EPW_{(i)}$, (b) $EPW_{(i,ii)}$, and (c) $EPW_{(i,ii,iii)}$. (d) Unapproximated EPW (A+B+C) split into the contributions of (e) EKE flux (A+B) and (c) topographic-contribution (C). Terms are smoothed with a 75 km-radius Gaussian kernel. (*cf.* Figure 1 for a detailed caption).

In this section, we evaluate the validity of approximations (ii) and (iii) to reliably infer the η-based $EPW_{(i)}$. We first compare $EPW_{(i)}$ (unapproximated η-based EPW) and $EPW_{(i,ii,iii)}$ (approximated η-based EPW used by Zhai et al., 2010). Next, we detail separately the differences due to approximations (ii) and (iii).

Note that most of the figures discussed in the study show smoothed terms (Figures 2, 4, B1). Smoothed terms highlight the large-scale patterns driving the cumulative contributions in the WB region. Smoothing also facilitates comparison between $EPW_{(i,ii,iii)}$ (Figure 1a-c) and the other EPW versions. The smoothing length scale corresponds to a typical mesoscale eddy radius at mid-latitudes (75 km), as inferred from satellite altimetry (Chelton et al., 2011). See Appendix B for details on the sensitivity of EPW to the smoothing length scale.

4.1 Mesoscale EKE sources and sinks from the unapproximated and approximated η-based EPWs ($EPW_{(i)}$ *vs.* $EPW_{(i,ii,iii)}$)

Figure 2a-c shows the different versions of the η-based EPW in the Agulhas Current region ($EPW_{(i)}$, $EPW_{(i,ii)}$ and $EPW_{(i,ii,iii)}$). $EPW_{(i)}$ and $EPW_{(i,ii,iii)}$ have different local patterns and magnitudes in the Agulhas Current region (Figure 2a,c). In the WB region, $EPW_{(i)}$ is predominantly negative, but shows patterns of varying magnitude and sign (Figure 2a). This contrasts with $EPW_{(i,ii,iii)}$ which is almost uniformly negative (Figure

2c). Both EPWs show an EKE sink in the WB region, but that of $EPW_{(i)}$ (-3.13 GW) is significantly larger than that of $EPW_{(i,ii,iii)}$ (-0.99 GW).

The differences between $EPW_{(i)}$ and $EPW_{(i,ii,iii)}$ show that $EPW_{(i,ii,iii)}$ — the approximated η-based version of EPW defined by Zhai et al. (2010) — is not a good estimate of the unapproximated η-based $EPW_{(i)}$ in the Agulhas Current region (Figure 2a,c). This indicates that one or both of the approximations (ii) and (iii) are not valid for inferring the η-based $EPW_{(i)}$.

4.2 Bias due to approximation (ii)

Approximation (ii) of η primarily reflecting the 1^{st} baroclinic mode can bias the η-based $EPW_{(i,ii)}$ in two ways. It can bias the accurate estimate of the contribution of the 1^{st} baroclinic mode to the η-based $EPW_{(i)}$. η does not exclusively reflect eddies (η variance) of the 1^{st} baroclinic mode. In the WB region of the Agulhas Current, the variance of the modeled η accounts for about 16 $\pm$ 4% of the barotropic mode, 38 $\pm$ 4% of the 1^{st} baroclinic mode and 36 $\pm$ 2% of a coupling between the first 10 vertical modes (Figure C1). See Appendix C for details on the partitioning of the η variance into the 10 first vertical modes in the Agulhas Current region. Approximation (ii) may also bias the estimate of the EKE flux divergence for the mesoscale reservoir, because $EPW_{(i,ii)}$ does not include the barotropic contribution. Contributions from the barotropic and 1^{st} baroclinic $EPW_{(i)}s$ can transport EKE in a decoupled (coupled) manner, which would then compensate (accumulate) when considering the EKE flux divergence for the mesoscale reservoir.

$EPW_{(i,ii)}$ and $EPW_{(i)}$ have similar local patterns and magnitudes in the Agulhas Current region (Figure 2a,b). However, their cumulative EKE sinks differ slightly in the WB region. $EPW_{(i,ii)}$ denotes a larger EKE sink (-4.83 GW; Figure 2b) than $EPW_{(i)}$ (-3.13 GW; Figure 2a). $EPW_{(i,ii)}$ includes only the contribution from the 1^{st} baroclinic mode, while $EPW_{(i)}$ can be split into the contributions of the barotropic mode (-1.01 GW in the WB region; not shown) and the 1^{st} baroclinic mode (-2.12 GW in the WB region; not shown).

The large similarities between $EPW_{(i)}$ and $EPW_{(i,ii)}$ patterns (Figure 2a,b) indicate that approximation (ii) is not the main reason for the large discrepancies between $EPW_{(i)}$ and $EPW_{(i,ii,iii)}$ in the Agulhas Current region (Figure 2a,c). However, approximation (ii) leads to an overestimation of (1) the EKE sink in the WB region (overestimation by 154%) and (2) the contribution of the 1^{st} baroclinic mode (overestimation by 228%).

4.3 Bias due to approximation (iii)

The topography acts on $EPW_{(i,ii)}$ ($A1 + A2 + C$; Table 1) via two contributions: the β-driven flux ($A2$) and the geostrophic EKE flux (C). Approximation (iii) of weak topographic contribution is equivalent to assuming that the mesoscale EKE flux ($A1$) has larger spatial variations than that of the topography ($A2$ and C) (Zhai et al., 2010).

$EPW_{(i,ii)}$ and $EPW_{(i,ii,iii)}$ have very different patterns and magnitudes in the Agulhas Current region (Figure 2b,c). These differences are the same as those for $EPW_{(i)}$ and $EPW_{(i,ii,iii)}$ (*cf.* section 4.1). This confirms that approximation (iii) is the one that limits the estimate of the η-based $EPW_{(i)}$ in the Agulhas Current region (Figures 2a,b,c). This also indicates that the topographic contributions ($A2$ and C in $EPW_{(i)}$ and $EPW_{(i,ii)}$; Table 1) dominate the η-based EPWs ($EPW_{(i)}$ and $EPW_{(i,ii)}$; Figures 2a,b). In particular, the topographic contribution to the geostrophic EKE flux (C: -4.54 GW in the WB region; not shown) is the dominant contribution, compared to the β-driven topographic contribution ($A2$: 0.70 GW in the WB region; not shown).

In summary, $EPW_{(i,ii,iii)}$ — the EPW version defined by Zhai et al. (2010) — is not a good estimate of $EPW_{(i)}$ — the unapproximated η-based EPW — in the Agulhas Current region, because approximation (iii) is not valid (Figure 2a-c). In other words, the β-driven linear EKE flux acting on the 1^{st} baroclinic mode ($EPW_{(i,ii,iii)}$) is not the leading order contribution to the η-based $EPW_{(i)}$. $EPW(i)$ ($A1 + A + 2 + C$; Figure 1a) is dominated by interactions between the geostrophic EKE flux of the barotropic and 1^{st} baroclinic modes with topographic gradients (C).

However, the η-based $EPW_{(i)}$ still shows an EKE sink in the WB region (<0; Figure 2a) in contrast with the unapproximated EPW (>0; Figure 1d). This suggests that approximation (i) of geostrophy is the one at the origin of the opposing paradigms supported by η-based and unapproximated EPW.

5 η-based $EPW_{(i)}$ and unapproximated EPW

In this section, we inform about the invalidity of approximation (i) of geostrophy for a reliable inference of the unapproximated EPW. We first evaluate the mesoscale EKE sources and sinks represented by the unapproximated EPW. We then characterize the main contributions to the unapproximated EPW.

5.1 Mesoscale EKE sources and sinks from the η-based $EPW_{(i)}$ and the unapproximated EPW

$EPW_{(i)}$ and EPW show no similarity over the whole Agulhas Current region (Figure 2a,d). In the WB region, they have similar patterns of locally opposite signs. These local differences are reflected in their cumulative values, which amount to an EKE sink ($<$ 0) and an EKE source ($>$ 0), for $EPW_{(i)}$ and EPW respectively. This confirms that approximation (i) of geostrophy is not valid for inferring EPW in the Agulhas Current region (Figure 2a,d).

The unapproximated EPW indicates a source of EKE in the WB region (0.82 GW; Figure 2d). The locally gained EKE is then exported downstream of the Agulhas Current, eventually towards the South Atlantic, or recirculated into the Indian Ocean along the Agulhas Return Current (vector field in Figure 2d). Locally, the unapproximated EPW shows patterns and magnitudes consistent with the documented variability of the Agulhas Current (Lutjeharms, 2006; Tedesco et al., 2022).

Along the northern branch of the WB region (31°E – 26°E), where the Agulhas Current is stable, the unapproximated EPW is weak compared to the rest of the domain and have patterns of contrasting sign (Figure 2d). EPW is negative upstream of the Natal Bight (31°E) and between the Natal Bight and the Agulhas Bank over a narrow band along the straight part of the shelf (26°E-30.5°E). In these areas, EPW ($<$0) therefore indicates that the eddy dynamics are mainly acting to deplete the mesoscale reservoir. This is consistent with the northern Agulhas Current being stable due to the topographic constraint (Lutjeharms, 2006; Tedesco et al., 2022). EPW is locally positive at the Natal Bight. This is consistent with the punctual generation (4–5 times per year) of Natal Pulses: mesoscale eddies that are the main source of variability of the Northern Agulhas Current (Lutjeharms, 2006; Elipot & Beal, 2015).

Along the southern branch of the WB region (26°E – 23°E), where the shelf curvature increases and the Agulhas Current is unstable, the mesoscale EPW is large and positive (Figure 2d). In this area, EPW shows the largest EKE source of the WB region. This shows that eddy dynamics are mainly energising the mesoscale reservoir there. This is consistent with the highly unstable nature of the southern Agulhas Current and the documented generation of quasi-permanent meanders there (Lutjeharms, Penven, & Roy, 2003; Lutjeharms, Boebel, & Rossby, 2003; Schubert et al., 2021). Note that the mesoscale EPW locally changes sign and becomes negative at the tip of the shelf (24°E – 23°E). There, the shelf curvature decreases and the current is constrained by the topography, locally enhancing EKE dissipation and preventing mixed barotropic-baroclinic instability to trigger (energy conversion terms of barotropic and baroclinic instability are negative, indicating a kinetic energy loss from mesoscale eddies in favor of the mean circulation; Tedesco et al., 2022).

5.2 Main contributions to the unapproximated EPW

Geostrophic effects are not the leading contribution to EPW in the Agulhas Current region. We therefore characterize the main contributions to the unapproximated mesoscale EPW below. We first evaluate the main contributions to the unapproximated EPW and then discuss their range of validity.

5.2.1 Contributions of ageostrophic and topographic effects

The unapproximated EPW ($A + B + C$; Table 1; Figure 2d) consists of an EKE flux contribution ($A + B$; Figure 2b) and a topographic contribution (C; Figure 2c). Both are large and largely compensate in the Agulhas Current region. In the WB region, the cumulative value of EPW is dominated by the positive EKE flux contribution ($A + B$). However, it can be locally dominated by the negative topographic contribution (C), as for example along the straight part of the shelf, where a narrow band of negative EPW is visible (30.5°E – 26°E; Figure 2d).

The EKE flux contribution ($A + B$) and the topographic contribution (C) do not account for geostrophic and ageostrophic effects to the same extent. Approximation (i) of geostrophy limits the estimate of the EKE flux contribution ($A + B$), because the unapproximated $A + B$ (Figure 2e) is very different from its geostrophic analogue ($A1$; Figure 2c). The velocity divergence contribution to the EKE flux (A) accounts for ageostrophic effects and the β-effect. While the eddy pressure shear work (B) exclusively accounts for ageostrophic effects (*cf.* section 2.2.2). The geostrophic EKE flux is thus reduced to a linear β-effect ($A1$; Figure 2c), which we have shown to be negligible for the η-based $EPW_{(i)}$ ($A1 + A2 + C$; Figure 2a).

On the other hand, approximation (i) of geostrophy allows to derive a qualitatively good estimate of the topographic contribution (C). The unapproximated C-contribution (Figure 2f) is similar to the η-based $EPW_{(i)}$ ($A1 + A2 + C$; Figure 2a), which we have seen to be dominated by the geostrophic C-contribution (*cf.* section 4).

Note that the EKE source shown by the unapproximated EPW in the WB region (0.82 GW; Figure 2d) is mainly due to the barotropic EPW (1.56 GW; not shown), while the 1^{st} baroclinic EPW represents an EKE sink (-0.74 GW; not shown) and acts against the barotropic EPW. This emphasises the importance of properly defining the unapproximated mesoscale EPW as the sum of barotropic and 1^{st} baroclinic EPWs. In the case of the unapproximated EPW, both vertical modes compensate each other, while in the case of the η-based $EPW_{(i)}$, both vertical modes amplify each other (*cf. section 4*). The different contributions of barotropic and 1^{st} baroclinic modes to the different versions of EPW is therefore non-trivial.

In summary, the η-based $EPW_{(i)}$ and the unapproximated EPW support opposite paradigms in the Agulhas Current region, because they have different leading order contributions. We first showed that the η-based $EPW_{(i)}$ is dominated by the topographic contribution acting on the geostrophic EKE flux. We then showed that the unapproximated EPW is dominated overall by ageostrophic effects and locally by the topographic contribution. In the following section, we characterize the range of validity for the dominance of ageostrophic effects.

5.2.2 Scale analysis argument for large ageostrophic effects and weak β-effect

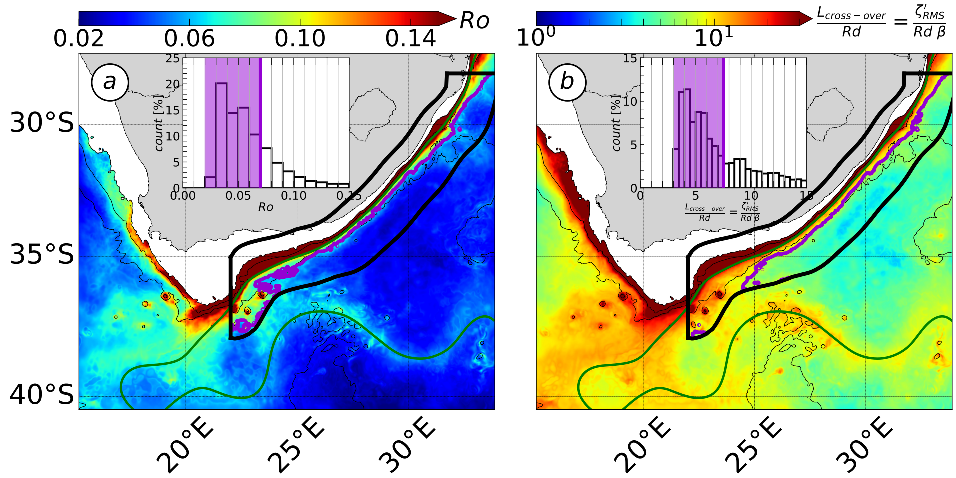

Figure 3: Adimensional metrics measuring the contribution of ageostrophic effects to EPW. (a) Rossby number for mesoscale eddies ($Ro = \frac{\zeta'_{RMS}}{f}$) and (b) ratio between the cross-over scale ($L_{g,ag} = \frac{\zeta'}{\beta}$; Eq. 15) and the characteristics length scale of mesoscale eddies (Rossby deformation radius; Rd). In the barplots, counts of (a) and (b) in the WB region are expressed in [%] and shaded areas show the 70 % percentile. In the maps, purple contours show (a) and (b) 70 % percentiles in the physical space. (*cf.* Figure 1 for a detailed caption)

5.2.2.1 Definition of a cross-over scale

The founding hypothesis of the paradigm of mesoscale eddies graveyard at western boundaries was that long baroclinic Rossby waves are the main contributor to the EKE flux divergence (Zhai et al., 2010). This hypothesis favours one contribution of EPW — the β-effect ($A1$ in $EPW_{(i)}$; Table 1) — over others, which include ageostrophic effects and the topographic contribution. We have seen that for the EKE flux contribution ($A + B$) acting on the unapproximated EPW (Table 1), ageostrophic effects overcome the β-effect in the WB region of the Agulhas Current (*cf.* section 5). Here, we use a scale analysis to evaluate in which regimes we can expect ageostrophic effects to dominate over the β-effect for the unapproximated EPW.

Ageostrophic effects acting on the EKE flux contribution ($A+B$; Table 1) take the form either of (1) both ageostrophic velocities and pressure ($EPW_{(ag)}$) or (2) coupled ageostrophic velocities to geostrophic pressure ($EPW_{(g,ag)}$). Using quasi-geostrophic scalings of velocity and pressure, we perform the scaling of $EPW_{(ag)}$ (Eq. 11), $EPW_{(g,ag)}$ (Eq. 12), and of the β-effect (Eq. 13), as follows:

$$\left|\int_{-H}^{\eta} \nabla_H \cdot \left(\mathbf{u}'_{ag,n} p'_{ag,n} \phi_n^2\right)\ dz\right| \sim \frac{Ro^2 U'_g P'_g H}{L} \tag{11}$$

$$\left|\int_{-H}^{\eta} \nabla_H \cdot \left(\mathbf{u}'_{ag,n} p'_{g,n} \phi_n^2\right)\ dz\right| \sim \frac{Ro U'_g P'_g H}{L} \tag{12}$$

$$\left|\frac{\beta \rho_0 g^2}{2f^2} \int_{H}^{\eta} \frac{\partial}{\partial x}\left(\frac{\phi_n^2}{|\phi_n^2|_{z=0}} \alpha_n^2 \eta'^2\right)\ dz\right| \sim \frac{\widehat{\beta} P' U'_g H}{\widehat{f}} \tag{13}$$

We use the following adimensionalized variables $\left|\nabla_H, \frac{\partial}{\partial x}\right| \sim \frac{1}{L}$, $\left|\int_{-H}^{\eta} <.> dz\right| \sim H$, $|\beta| \sim \widehat{\beta}$, $|f| \sim \widehat{f}$. Using the expansion of velocity and eddy pressure with Ro the small parameter, we define $\left|\mathbf{u}'_{ag,n}\right| \sim RoU'_g$ and $\left|p'_{ag,n}\right| \sim RoP'_g$, with $Ro = \left|\frac{1}{H}\int_{-H}^{\eta}\left(\frac{\zeta'_{RMS}}{f}\right)\ dz\right| \sim \widehat{\frac{\zeta'_{RMS}}{f}}$ the vertical average of the root mean square of the normalized relative vorticity for mesoscale eddies ($\zeta' = \partial_x v' - \partial_y u'$). Using geostrophy, we define $|p'_{g,n}| \sim P'_g \sim \rho_0 \widehat{f} U'_g L$. Using the hydrostatic approximation and geostrophy, we define $\left|\frac{\phi_n^2 \alpha_n^2 \eta'^2}{|\phi_n^2|_{z=0}}\right| \sim \frac{P'_g U'_g L \widehat{f}}{\rho_0 g^2}$.

The scale analysis is used to define two cross-over scales ($L_{g,ag}$ in Eq. 15 and L_{ag} in Eq. 14), at which the contributions to EPW of the two forms of ageostrophic EKE flux ($EPW_{(g,ag)}$ and $EPW_{(ag)}$) have the same order of magnitude as the contribution of the β-effect:

$$\frac{(11)}{(13)} = \frac{Ro^2 \widehat{f}}{L\widehat{\beta}} = \frac{\widehat{\zeta'_{RMS}}^2}{L\widehat{f}\widehat{\beta}} = \frac{L_{ag}}{L}, \text{ with } L_{ag} = \frac{\widehat{\zeta'_{RMS}}^2}{\widehat{f}\widehat{\beta}} \tag{14}$$

$$\frac{(12)}{(13)} = \frac{Ro\widehat{f}}{L\widehat{\beta}} = \frac{\widehat{\zeta'_{RMS}}}{L\widehat{\beta}} = \frac{L_{g,ag}}{L}, \text{ with } L_{g,ag} = \frac{\widehat{\zeta'_{RMS}}}{\widehat{\beta}} \tag{15}$$

$L_{g,ag}$ is the ratio of the eddy vorticity and of the β parameter (Eq. 15). $L_{g,ag}$ is greater than L_{ag} if the eddy Rossby number is <1, which is the case for mesoscale eddies. $L_{g,ag}$ will thus generally impose the most restrictive condition. Note that the definition of the cross-over scales is not unique. An equivalent definition involving the Rhines scale can be defined using another scaling of the eddy Rossby number($Ro = \frac{U'}{fL}$). See appendix D for details on the alternative definition of $L_{g,ag}$ for the mesoscale EPW in the Agulhas Current region.

5.2.2.2 *Cross-over scale performed in the Agulhas Current region*

We compare $L_{g,ag}$ (Eq. 15) with the characteristic length scale of mesoscale eddies — the Rossby deformation radius (Rd) of about 30 km in the region of the Agulhas Current — (Figure 3). The typical values of Ro confirm that mesoscale eddies are mainly geostrophic in the WB region (Ro in $O(0.02$–$0.07)$ in 70% of the WB region and Ro in $O(0.07$–$0.65)$ at the inner front; Figure 3a). However, the typical values of $L_{g,ag}$ show that coupled geostrophic-ageostrophic effects dominate over the β-effect at mesoscale ($L_{g,ag}$ in $O(3$–$7)Rd$ in 70% of the WB region and $L_{g,ag}$ in $O(7$–$19)Rd$ at the inner front; Figure 3b). On the other hand, the purely ageostrophic effects are weaker than the contribution of the β-effect (L_{ag} in $O(0.1$–$0.5)Rd$ in the WB region; not shown).

Typical values of $L_{g,ag}$ (Eq. 15) are about $O(105$-$256)$ km in the region of the Agulhas Current (not shown). This sets the upper limit of the scale range where coupled geostrophic-ageostrophic effects are expected to dominate over the β-effect. This scale range is consistent with the result of the idealized numerical simulations shown in Zhai et al. (2010), where an eddy of 500 km-diameter was used to illustrate the validity of the approximated η-based version of EPW.

In summary, approximation (i) of geostrophy is not valid to infer the unapproximated EPW in the Agulhas Current region, because the coupled geostrophic-ageostrophic EKE flux overall dominate the EPW at the mesoscale range (105 km>L> $Rd \sim$ 30 km). We evaluate in the next section, the use of approximation (i) of geostrophy to infer $AEKE$ (Table 2), the nonlinear component of EKE flux divergence.

6 η-based $AEKE_{(i)}$ and unapproximated $AEKE$

We first evaluate the mesoscale EKE sources and sinks represented by the η-based and the unapproximated $AEKE$. We then characterize the main contributions of the two $AEKE$s.

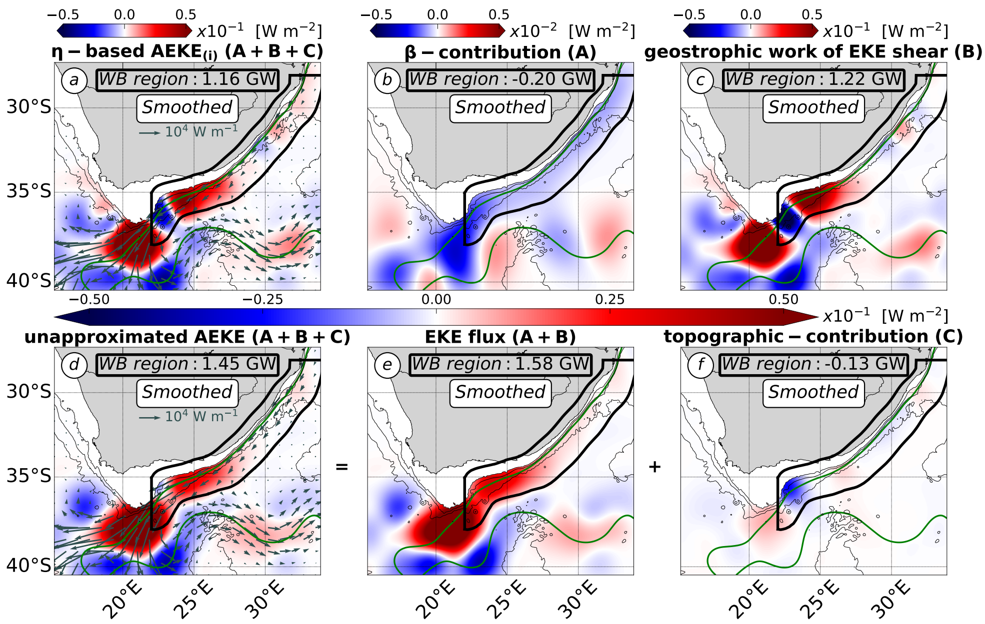

Figure 4: η-based $AEKE_{(i)}$ and unapproximated $AEKE$ [W m^{-2}] (Table 2). (a) η-based $AEKE_{(i)}$ $(A+B+C)$ split into the contributions of (b) β-effect (A) and (c) work of EKE shear (B). (d) Unapproximated $AEKE$ $(A+B+C)$ split into the contributions of (e) EKE flux $(A+B)$ and (f) topographic-contribution (C). (a,d) Vector fields show (a) geostrophic EKE flux $(\frac{\rho_0}{2}\int_{-H}^{\eta}\mathbf{u}_{g,n}\phi_n||\mathbf{u}'_{g,n}\phi_n||^2\;dz$, with $n=0-1)$ and (b) unapproximated EKE flux $(\frac{\rho_0}{2}\int_{-H}^{\eta}\mathbf{u}_n\phi_n||\mathbf{u}'_n\phi_n||^2\;dz$, with $n=0-1)$ [W m^{-1}]. Note the different colorbar ranges between (b) and the other panels. All terms are smoothed with a 75 km-radius Gaussian kernel. (*cf.* Figure 1 for a detailed caption).

6.1 Mesoscale EKE sources and sinks from the η-based $AEKE_{(i)}$ and the unapproximated $AEKE$

Figure 4a,d shows the η-based $AEKE_{(i)}$ and unapproximated $AEKE$ in the Agulhas Current region. In the WB region, $AEKE_{(i)}$ and $AEKE$ are in fairly good agreement. Both $AEKE$s show a net EKE source (>0; Figure 4a,d). The η-based $AEKE_{(i)}$ accounts for 73% of the cumulative EKE source shown by the unapproximated $AEKE$ (the remaining 27% being accounted for by ageostrophic effects). The locally gained EKE is then exported out of the WB region, eventually into the South Atlantic Ocean or recirculated in the South Indian Ocean (vector field in Figure 4a,d). The large similarities between $AEKE_{(i)}$ and $AEKE$ indicate that approximation (i) of geostrophy is valid for qualitatively inferring $AEKE$.

The two $AEKE$s show patterns and magnitudes consistent with the documented variability of the Agulhas Current (Lutjeharms, 2006; Tedesco et al., 2022). Along the northern branch of the WB region (31°E – 26°E), where the Agulhas Current is stable, both $AEKE$s are weak (one order of magnitude smaller than in the rest of the domain; Figure 4a,d). Along the southern branch of the WB region (26°E – 23°E), both $AEKE$s are large and generally positive where the shelf curvature increases and the current is documented to be unstable (Lutjeharms, 2006; Tedesco et al., 2022) (Figure 4a,d). In this area, the $AEKE$s indicate that the eddy dynamics mainly act to energise the mesoscale reservoir, similar to the unapproximated EPW (Figure 2d). Note that $AEKE_{(i)}$, and $AEKE$ in a lesser extend, locally change sign and becomes negative at the tip of the shelf (24°E – 23°E), where the topographic constraint on the current is large. This local magnitude difference between the EKE sinks shown by $AEKE_{(i)}$ and $AEKE$ suggests that ageostrophic effects substantially contribute to the mesoscale eddy dynamics at this location.

6.2 Main contributions to the η-based $AEKE_{(i)}$

The η-based $AEKE_{(i)}$ ($A + B + C$; Table 2; Figure 4a) consists of a geostrophic EKE flux contribution ($A+B$; Figures 4b,c) and a topographic contribution acting on the geostrophic EKE flux (C; not shown), which are of different importance in the Agulhas Current region. The geostrophic $A+B$-contribution accounts for 61% of the net $AEKE_{(i)}$, while the geostrophic topographic contribution accounts for the remaining 39% . Within the geostrophic EKE flux ($A+B$), the geostrophic EKE shear work (B) is the main contribution (Figure 4c). The geostrophic EKE shear work (B; Figure 4c) has locally similar patterns and magnitudes than $AEKE_{(i)}$ ($A+B+C$; Figure 4a) in the Agulhas Current region. The velocity divergence contribution (A) corresponds to a negligible nonlinear β-effect (Figure 4b). It represents a weak EKE sink in the WB region (<0; Figure 4b), similar to its linear analogue acting on $EPW_{(i)}$ ($A1$; Figure 2c). In a nutshell, the η-based $AEKE_{(i)}$ ($A + B + C$; Table 2) is dominated by geostrophic effects in the form of the EKE shear work (B).

6.3 Main contributions to the unapproximated $AEKE$

Similar to the η-based $AEKE_{(i)}$, the unapproximated $AEKE$ ($A + B + C$; Table 2) consists in an EKE flux contribution ($A + B$) and a topographic contribution (C), which are of different importance in the Agulhas Current region. In the WB region, $AEKE$ ($A+B+C$; Figure 4d) is overall dominated by the positive EKE flux contribution ($A+B$; Figure 4e), except at the shelf tip (24°E – 23°E) where it is locally dominated by the negative topographic contribution (C; Figure 4f).

The EKE flux contribution ($A + B$) and the topographic contribution (C) do not account for geostrophic and ageostrophic effects in the same proportions. Approximation (i) of geostrophy allows to infer a qualitative estimate of the patterns of the EKE flux contribution ($A + B$; the leading order contribution of $AEKE = A + B + C$). However, note that the ageostrophic effects acting on A and B are significant. The geostrophic EKE flux ($A + B$; Figure 4b,c) underestimates the EKE source shown by the unapproximated analogue ($A + B$; Figure 4e) (underestimation of 35%).

On the other hand, approximation (i) of geostrophy limits the estimation of the patterns and magnitude of the topographic contribution (C; a secondary contribution to $AEKE = A + B + C$). Geostrophic and unapproximated C-contributions have cumulative values of opposite sign in the WB region (geostrophic C: 0.65 GW, not shown and unapproximated C: -0.38 GW in Figure 4f). This indicates that the topographic contribution (C) acting on $AEKE$ is largely influenced by ageostrophic effects.

Note that the EKE source shown by the unapproximated $AEKE$ (2.29 GW; Figure 4d) is due to the accumulation of the barotropic $AEKE$ (0.79 GW; not shown) and 1^{st} baroclinic $AEKE$ (1.50 GW; not shown). This suggests that the mesoscale $AEKE$ could be approximated from the contribution of the 1^{st} baroclinic mode. Similar contributions of the barotropic and 1^{st} baroclinic modes are found for the η-based $AEKE_{(i)}$ (mesoscale $AEKE_{(i)}$: 1.67 GW in Figure 4a and barotropic $AEKE_{(i)}$: 0.57 GW and 1^{st} baroclinic $AEKE_{(i)}$: 1.10 GW; not shown).

In summary, the η-based $AEKE_{(i)}$ and the unapproximated $AEKE$ support similar paradigms in the Agulhas Current region, because geostrophic effects are a major contributor to $AEKE$ (via the EKE shear work B). However, the accurate estimation of its magnitude using η is less reliable. Indeed, ageostrophic effects also make a significant contribution to $AEKE$ $(A + B + C)$, via all its sub-contributions (A, B and C).

7 Summary and Discussion

In this study, we have investigated the main contributions to the mesoscale EKE flux divergence in the Agulhas Current region. Motivated by opposing η-based and model-based paradigms of mesoscale eddy dynamics, we aimed to evaluate the validity of the approximation (i) of geostrophy to infer the mesoscale EKE flux divergence in this region. Geostrophy is a good approximation for inferring mesoscale eddy velocities, but it is a different matter to use it to infer the EKE flux divergence (a tendency term of the EKE budget representing net EKE sources and sinks for ocean dynamics in equilibrium; Harrison & Robinson, 1978). Our analysis used a regional numerical simulation to evaluate the main contributions of the components of the EKE flux divergence, consisting of the eddy pressure work (EPW) and the advection of EKE ($AEKE$). In this section, we summarise our main findings and discuss their implications for the understanding of mesoscale eddy dynamics.

7.1 On the use of sea surface height (η) to infer the mesoscale EKE flux divergence

7.1.1 Eddy pressure work (EPW)

Based on an approximate calculation of EPW using sea surface height (η), Zhai et al. (2010) showed that western boundaries are mesoscale EKE sinks. The η-based diagnosis of EPW is by definition geostrophic. It reduces to the contribution of long baroclinic Rossby waves (linear β-contribution acting on the 1^{st} baroclinic mode) with additional approximations to (ii) the vertical structures of mesoscale eddies and (iii) the contribution of topography. Our results show that none of the approximations (i), (ii) and (iii) are valid to infer the mesoscale EPW in the Agulhas Current region.

We first showed that the η-based $EPW_{(i)}$ (considering only approximation (i); Table 1) is dominated by a topographic contribution acting on the barotropic and 1^{st} baroclinic modes (Figure 2a-d). While the Rossby waves contribution is negligible ($A1$; Figure 2c). This invalidates the use of approximations (ii) and (iii). We then showed that the unapproximated EPW (Table 1) is dominated overall by the coupled geostrophic-ageostrophic EKE flux and locally by topographic interactions (Figures 2d-f,3b). A scale analysis emphasised that the coupled geostrophic-ageostrophic EKE flux dominates EPW at mesoscale ($L > O(30)$ km), while the β-effect could potentially dominate EPW at larger scales ($L > O(105–256)$ km).

The dominance of ageostrophic effects explains the opposite paradigms supported by the η-based $EPW_{(i)}$ and the unapproximated EPW in the Agulhas Current region. This also invalidates the use of approximation (i) of geostrophy to infer the mesoscale EPW in this region.

7.1.2 Advection of eddy kinetic energy ($AEKE$)

We have defined and performed an unapproximated η-based version of the $AEKE$ component ($AEKE_{(i)}$; Table 2) in the Agulhas Current region. Our results show that approximation (i) of geostrophy is valid to infer a qualitative mesoscale $AEKE$. Unapproximated $AEKE$ and η-based $AEKE_{(i)}$ support similar paradigms in the Agulhas Current region (Figure 4a,d), because geostrophic effects largely contribute to $AEKE$ ($A+B+C$; Figure 4a), via the term of the EKE shear work (B; Figure 4c).

Our results support the use of η to qualitatively infer the mesoscale EKE source represented by the $AEKE$ component in the western boundary region of the Agulhas Current. This is furtherly supported by the η-based $AEKE_{(i)}$ performed using observations (Figure 5). The observed η-based $AEKE_{(i)}$ (Table 2) is calculated by combining: (1) η measured by satellite altimetry, (2) vertical modes calculated from time-averaged stratification derived from the WOCE climatology, and (3) $\lambda_n = \frac{\eta_n}{\eta}$ (Eq. 2.3.1) and $\alpha_n = \frac{\eta'_n}{\eta'}$ (Eq. 2.3.1) parameters — modulating η according to vertical modes — derived from our numerical simulation at each time step and spatially averaged over the WB region. The observed η-based $AEKE_{(i)}$ shows a mesoscale EKE source in the WB region in fairly good agreement with the modeled η-based $AEKE_{(i)}$ and the modeled unapproximated $AEKE$ (Figures 5a and 4a,d). It shows a large EKE source extending from about 26°E to the Retroflection (20°E), whose cumulative value is 43% and 32% of that of the modeled η-based $AEKE_{(i)}$ and the unapproximated $AEKE$, respectively.

Note that the fairly good qualitative agreement between observed η-based $AEKE$ and modeled versions of $AEKE$ (Figures 5a and 4a,d) highlights a reliable alternative to approximation (ii). The contribution of the barotropic and 1^{st} baroclinic modes to η, and hence to $AEKE$, can be reliably approximated in small regions using spatially averaged model-based partitioning of the modal η.

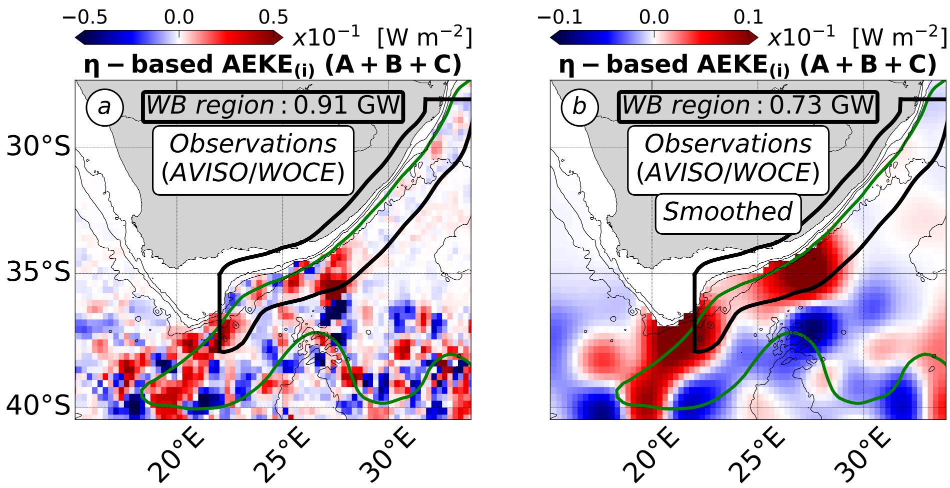

Figure 5: Observed η-based $AEKE_{(i)}$ [W m^{-2}] (Table 2). (a) Unsmoothed and (b) smoothed version of the observed η-based $AEKE_{(i)}$ performed using a combination of satellite altimetry data (AVISO), climatological data (WOCE) and model-based parameter (Eq. 7, 8). For (b), the smoothing radius is 75 km as for Figures 2, 4. Note the different colorbar range between the two panels. (*cf.* Figure 1 for a detailed caption).

7.1.3 *Conclusion on the mesoscale EKE flux divergence (EPW and $AEKE$)*

Our thorough analysis of the contributions to EPW and $AEKE$ (forming the EKE flux divergence) allows us to conclude on the use of η to infer mesoscale EKE sources and sinks in the Agulhas Current region. $AEKE$ represents the larger cumulative contribution ($AEKE$: 2.29 GW) to the EKE flux divergence in the WB region ($EPW + AEKE$: 3.12 GW; Figures 2d, 4d). Although, the approximation of geostrophy (i) does not allow to infer EPW (Figures 2a,d), it does allow to infer a qualitative estimate of $AEKE$ (73%; Figure 4a,d). This indicates that a qualitative estimate of the EKE flux divergence can be inferred from η, via the $AEKE$ component. In the model, using the η-based $AEKE_{(i)}$ as a proxy for the EKE flux divergence would lead to an underestimation of 46% of the EKE source in the WB region of the Agulhas Current (Figure 4a,d). From observations, however, the underestimation appears to be significantly larger (76%; Figure 5b and 4d).

Further investigation would therefore be required to conclude on the use of η measured by satellite altimetry to reliably infer the magnitude of the EKE source in this region.

Our results support the use of η to infer a qualitative estimate of the mesoscale $AEKE$, and subsequently of the mesoscale EKE flux divergence, but for fundamentally different reasons than Zhai et al. (2010). Zhai et al. (2010) used approximation (i) of geostrophy based on the hypothesis that long baroclinic Rossby waves are the main contributor to the EKE flux divergence. We show in this study that geostrophic effects make a significant contribution to the EKE flux divergence in the Agulhas Current region, via the advection of geostrophic EKE by geostrophic mean and eddy flows ($AEKE$).

7.2 On the mesoscale eddy energy budget at western boundaries

7.2.1 Main contributions acting on the mesoscale EKE flux divergence

The paradigm of a mesoscale eddies graveyard at western boundaries supported by Zhai et al. (2010) relies on long baroclinic Rossby waves (β-effect) as the main contributor to the mesoscale EKE flux divergence. Our results suggest that the mesoscale EKE flux divergence may not be dominated by the β-effect in western boundary regions.

Our scaling analysis showed that the magnitude of the linear β-contribution to EPW depends on metrics that provide a measure of dynamical and regional characteristics (Ro: mesoscale eddy Rossby number and the β parameter, respectively). The β parameter is usually low compared to Ro at mid-latitudes, resulting in a weak β-contribution to EPW. However, the β parameter is larger at low latitudes, suggesting that these regions may be more conducive to a large linear β-contribution to the EKE flux divergence. However, topographic interactions are large at western boundaries regardless of latitude. The topographic contribution may therefore be as large or larger than the β-effect contribution to the EKE flux divergence at western boundaries of all latitudes.

7.2.2 Main sources and sinks of EKE

The positive EKE flux divergence indicates that the mesoscale eddy dynamics in the WB region of the Agulhas Current are locally dominated by processes energising the mesoscale EKE reservoir. A recent study characterized the processes contributing to the mesoscale EKE source in this region (Tedesco et al., 2022). They showed that the local generation of mesoscale eddies — due to barotropic and mixed barotropic-baroclinic instabilities of the Agulhas Current — overcomes the local decay of locally- and remotely generated mesoscale eddies — mainly due to bottom stress and topographically channeled processes — . Our current study complements the process study of Tedesco et al. (2022), by showing (1) that the local mesoscale EKE source is largely redistributed in space by the advection done by geostrophic mean and eddy flows and (2) that this net spatial redistribution can be qualitatively inferred from η fields.

We suggest that the EKE flux divergence at western boundaries may vary with the presence or absence of a western boundary current. However, additional studies of other western boundary regions — with or without a western boundary current and for a broad latitudinal range — would be required to draw conclusions about the mesoscale eddy dynamics at each western boundary. The mesoscale EKE flux divergence could represent an EKE sink in the western boundary regions without a western boundary current, as topographically channeled processes damping mesoscale eddies would locally dominate. This is supported by studies based on *in situ* observations and idealized numerical simulations, for western boundary regions without a western boundary current (Evans et al., 2020; Z. Yang et al., 2021; Evans et al., 2022). The mesoscale EKE flux divergence could represent an EKE source in western boundary regions with a western boundary current, as the local generation of mesoscale eddies would dominate the damping effect of topographic interactions, similar to the Agulhas Current region (Tedesco et al., 2022). This is supported by the intense generation of mesoscale eddies by flow instabilities documented in several western boundary currents (Halo et al., 2014; Kang & Curchitser, 2015; Gula et al., 2015; Y. Yang & Liang, 2016; Yan et al., 2019; Li et al., 2021; Jamet et al., 2021; Tedesco et al., 2022). Furthermore, an exhaustive description of the processes contributing to mesoscale eddy decay in western boundary regions including a western boundary current, should include eddy-mean interactions in addition to topographic interactions (Holloway, 1987; Adcock & Marshall, 2000; Chen et al., 2014; Tedesco et al., 2022).

Appendix A Observed and modeled sea surface height (η) variance in the Agulhas Current region

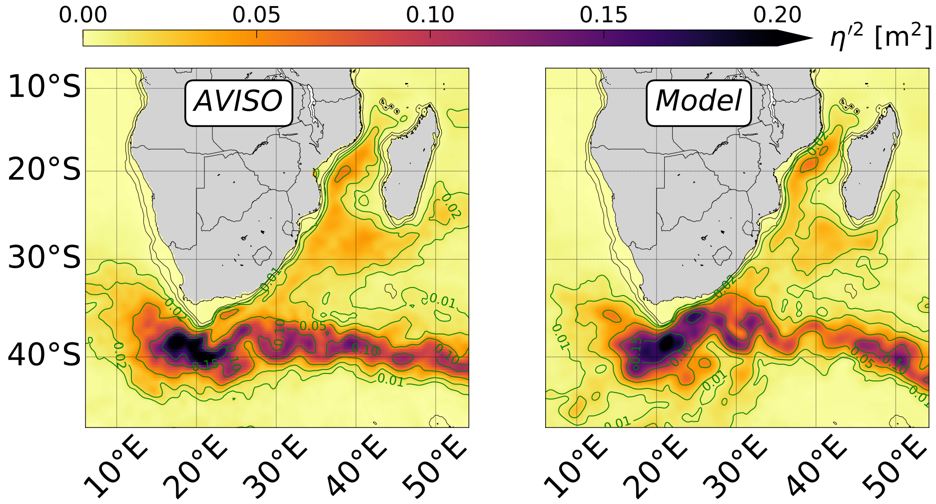

Figure A1: Observed and modeled mesoscale variability at the surface in the Agulhas Current system. η variance (η'^2) [m^2] performed from (a) a numerical simulation (dx $\sim$ 7.5 km) and (b) satellite altimetry data (AVISO). Green contours denote isolines of η variance and black contours denote 300 m and 1000 m isobaths.

The evaluation of the η-based version of the EKE flux divergence defined by Zhai et al. (2010) ($EPW_{(i,ii,iii)}$) in the model and observations, suggest that the modeled mesoscale eddy field might be weaker compared to observations (*cf.* section 3.3). The model of horizontal resolution of dx $\sim$ 2.5 km, used in this study, is forced at the boundaries at each time step by a parent model of dx $\sim$ 7.5 km. The parent simulation resolve mesoscale eddies of scales 50 km–100 km, but may underestimate their magnitude due to a too weak inverse turbulent cascade at smaller scales. This process has been shown to be of importance in the Subgyre regions of the Agulhas Current system (Schubert et al., 2020).

Based on this assumption, we evaluate the modeled mesoscale variability (η variance) simulated by the parent simulation (dx $\sim$ 7.5 km) against satellite altimetry data (Figure A1). The parent simulation covers the western part of the subtropical gyre of the Indian Ocean. The Agulhas Current originates from the lower end of the Mozambique Channel (32.5°E), where it feeds upon the Mozambique Current and the East Madagascar Current. The Agulhas Current flows along the South African coastline to the South African tip (20°E). From there, it Retroflects and become the Agulhas Return Current flowing eastward into the South Indian Ocean.

Modeled η variance represents the variability of the Agulhas Current system in overall good agreement with observations. The Mozambique Current, the East Madagascar Current and the Agulhas Current show moderate value of η variance ($O(0.02–0.03)$ m^2). The Agulhas Retroflection and the Agulhas Return Current show the largest η variance ($O(0.05–0.15)$ m^2). In the context of our study, a relevant difference is the weaker modeled η variance in the Subgyre region (35°E – 45°E and 25°S – 35°S). There, the model shows moderate value of smaller extend than in observations. This confirms that the modeled mesoscale eddies propagating westward through the Subgyre toward the Agulhas Current region have a weaker amplitude than in observations. This supports the weaker amplitude of the EKE sink in the WB region shown by the modeled $EPW_{(i,ii,iii)}$compared to observed one, to be due to a weaker modeled mesoscale eddy field forced at the boundaries.

Appendix B Sensitivity of the unapproximated *EPW* to spatial smoothing

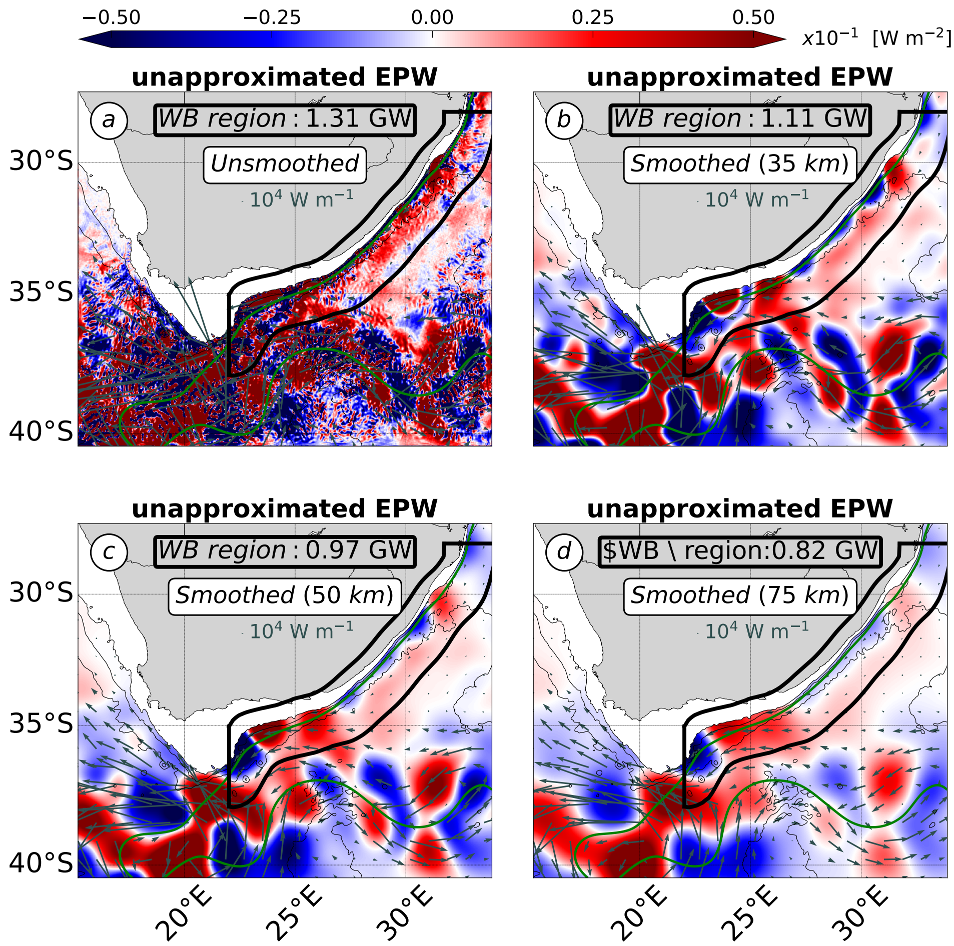

Figure B1: Sensitivity of the unapproximated EPW [W m^{-2}] (Table 1) to spatial smoothing. EPW shown for (a) no spatial smoothing and (b,c,d) spatial smoothing of different radius from (b) 35 km, (c) 50 km to (d) 75 km. Vector fields show the corresponding smoothed EKE flux ($\int_{-H}^{\eta} \mathbf{u}'_n p'_n \phi_n^2 \, dz$, with $n = 0 - 1$) [W m^{-1}]. (*cf.* Figure 1 for a detailed caption).

The unapproximated EPW (Table 1) is spatially smoothed to emphasise the large-scale patterns driving its cumulative contribution in the WB region (Figure B1). The unsmoothed EPW is characterized by small-scales patterns that are the most intense at topographic features — shelf slope (1000 m isobath), seamounts, canyons, roughness, among others — locally peaking at O(2.5 - 10) W m^{-2} (Figure B1a). In the WB region, the intense small-scales patterns of the unapproximated EPW are larger by one or two order of magnitude than the unsmoothed $EPW_{(i,ii,iii)}$ (O(0.01) W m^{-2}; Figure 2a). However, the magnitude of the cumulative contribution of EPW (1.31 GW; Figure B1a) is close to the one of $EPW_{(i,ii,iii)}$ (-1.32 GW; Figure 1b) in this region, regardless of the intense small-scale patterns. It indicates that the intense small-scale patterns locally compensate and do not significantly contribute to the cumulative EPW in the WB region.

The sensitivity of the unapproximated EPW to the smoothing is shown using a Gaussian kernel of progressively increasing length scale: from 35 km (the spatially-averaged Rossby deformation radius in region the modeled region) to 50 km and 75 km (two typical mesoscale eddies radii at mid-latitudes; Chelton et al., 2011). The patterns of EPW change with the different smoothing length scales, but the order of magnitude of the cumulative contribution in the WB region is reasonably unchanged ($\leq$ 30%; Figure B1). A similar sensitivity to the smoothing is found for the unapproximated $AEKE$ ($\leq$ 20%; not shown).

In the study, the label 'smoothed' in Figures refers to the Gaussian kernel using a 75 km-radius. The smoothings using 50 km- and 75 km-radius result in fairly close cumulative EPW in the WB region (Figures B1c,d). However, the 75 km-radius smoothing provides smoother patterns, emphasizing the most the large-scale patterns driving the EPW cumulative in the WB region, and facilitating the most its comparison with $EPW_{(i,ii,iii)}$ (Table 1; Figures 1b).

Appendix C Partitioning of sea surface height (η) variance into the barotropic and 9 first baroclinic vertical modes

In order to assess the validity of approximations (ii) and (iii) to infer EPW, we progressively relax the use of the approximations when inferring the η-based EPW term (*cf.* section 4). Relaxing the use of approximation (ii) of η primarily reflecting the 1^{st} baroclinic mode, requires to evaluate the partitioning of the η variance into the different vertical modes ($\alpha_n^2 = \frac{\eta_n'^2}{\eta'^2}$; Eq. 8 in section 2.3.1). η is a 2-dimensional field and cannot be straightforwardly projected onto the vertical mode base. However, the modal coefficient for η (η_n) can be inferred such as: $\eta_n' = \frac{p_n'(z=0)}{\rho_0 g}$, using the modal pressure at z =0 m and the hydrostatic relationship.

The modal expression of the η variance (η'^2) and α_n^2 are defined as follows:

$$\eta'^2 = \sum_{n=0}^{\infty} \eta_n' \sum_{m=0}^{\infty} \eta_m'$$

$$\eta'^2 = \sum_{n=0}^{\infty} \eta_n'^2 + \underbrace{\sum_{n=0}^{\infty} \sum_{m \neq n}^{\infty} \eta_n' \eta_m'}_{Intermodal\ coupling\ (C_{nm})}$$

$$\eta'^2 = \sum_{n=0}^{\infty} \eta_n'^2 + C_{nm} \tag{C1}$$

$$\alpha_n^2 = \frac{\eta_n'^2}{\eta'^2} \text{ and } \alpha_{nm} = \frac{C_{nm}}{\eta'^2} \tag{C2}$$

The modal expression of the variance of η (Eq. C1) involves an intermodal coupling term(C_{nm}). It corresponds to a phase-locked combination of vertical modes at the surface due to the modal correlation in time (Wunsch, 1997; Scott & Furnival, 2012). The degree of the surface modal correlation ($\frac{\sum_{n=0}^{9} \eta_n'^2}{\sum_{n=0}^{9} \eta_n'^2 + C_{nm}}$) is 1.8 in average in our numerical simulation, which is consistent with the 2-3 factor determined at global-scale from *in situ* data (Wunsch, 1997). However, it must be noted that the unapproximated EPW (Table 1) only accounts for the contribution of individual modes ($n = 0$ and $n = 1$). The coupling term C_{nm} is of importance for accurately decomposing η into vertical modes, but it does not contribute to the vertically-integrated form of the mesoscale EKE flux divergence considered in this study. Indeed, EPW involves the orthogonality condition resulting in canceling out the contribution of C_{nm} to EPW.

Using our numerical simulation of the Agulhas Current, we inferred α_n^2 the partitioning of the η variance into the barotropic and 9 first baroclinic modes (Figure C1). The barotropic and 10 first baroclinic modes account for 85-100% of the modeled η variance in the region (not shown).

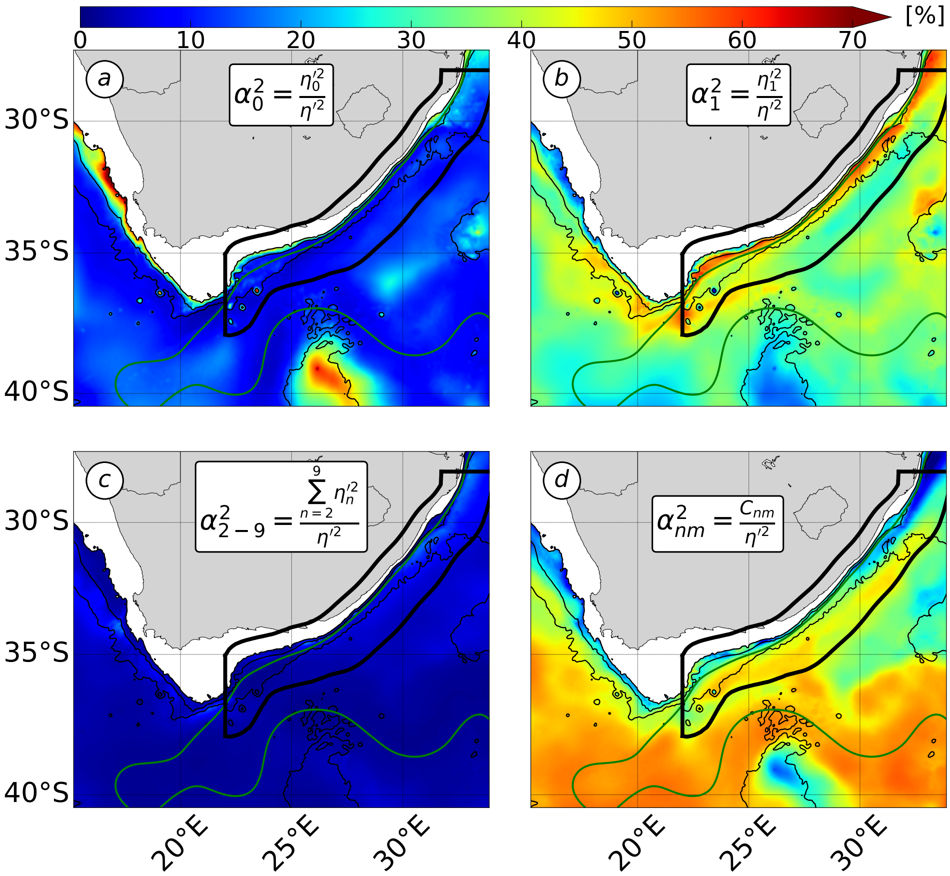

Figure C1: Partitioning of the sea surface height variance into categories of vertical modes ($\alpha_n^2 = \frac{\eta_n'^2}{\eta'^2}$) [%], including (a) the barotropic mode ($n = 0$), (b) the 1^{st} baroclinic mode ($n = 1$), (c) higher baroclinic modes ($n = 2 - 9$) and (d) the intermodal coupling at the surface (C_{nm}). (*cf.* Figure 1 for a detailed caption).

In the WB region, The η variance mainly partitions into the 1^{st} baroclinic mode (38 $\pm$ 2%; Figure C1b) and C_{nm} the intermodal coupling term (36 $\pm$ 2%; Figure C1d). It partitions more weakly, but still significantly into the barotropic mode (16 $\pm$ 4%) (Figure C1a). This is partially consistent with the usual interpretation of η primarily reflecting the 1^{st} baroclinic mode (Wunsch, 1997; Smith & Vallis, 2001). However, it also indicates that the vertical structure of mesoscale eddies — formally represented by the combination of the barotropic ($n = 0$) and 1^{st} baroclinic modes ($n = 1$) (Wunsch, 2007; Smith & Vallis, 2001; Venaille et al., 2011; Tedesco et al., 2022) — can be accurately inferred from η field. This enables us to relax approximation (ii) and compute the unapproximated η-based $EPW_{(i)}$ (defined as the sum of the barotropic and 1^{st} baroclinic contributions) from the modeled η field (*cf.* section 4).

Appendix D Alternative definition of the cross-over scale based on the Rhines scale

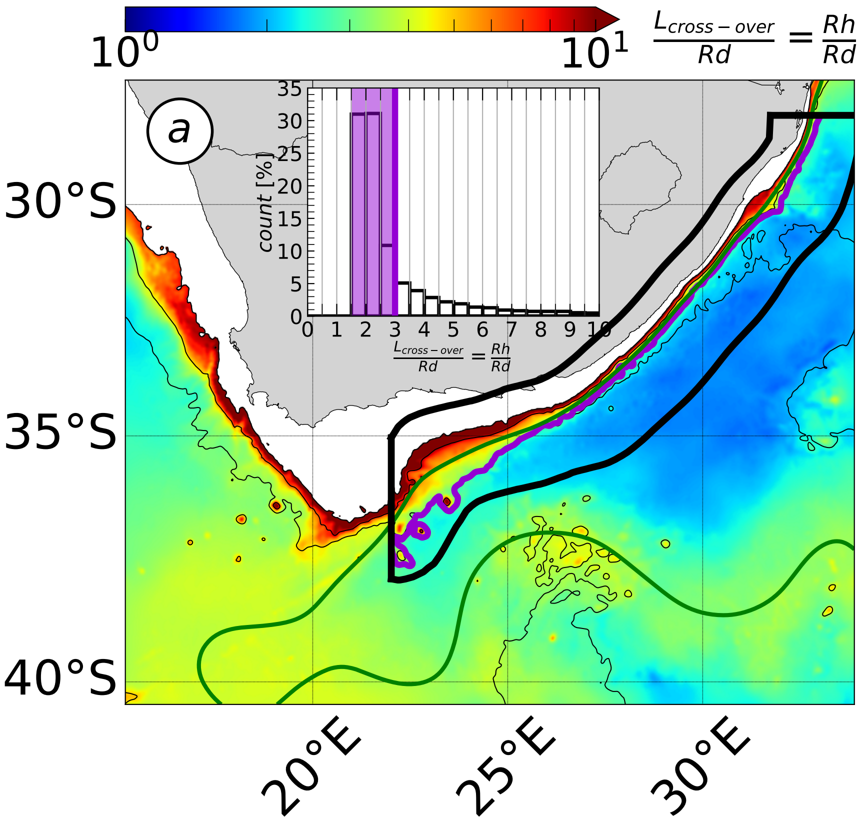

Figure D1: Alternative cross-over scale ($L_{g,ag} = Rh = \frac{1}{H}\int_{-H}^{\eta}\left(\sqrt{\frac{||\mathbf{u}'||}{\beta}}\right)\,dz$, with $||\mathbf{u}'||$ the magnitude of mesoscale eddies velocity) in the Agulhas Current region. (a) Ratio between the alternative cross-over scale and the characterisitc length scale of mesoscale eddies (Rossby deformation radius; Rd). In the barplot, counts of (a) in the WB region are in [%] and shaded area shows the 70 % percentile. In the map, purple contours show 70 % percentile of (a) in the physical space. (*cf.* Figure 1 for a detailed caption)

Our scale analysis allows us to define a cross-over scale, marking the transition between regimes of large ageostrophic effects and large β-effect acting on the unapproximated EPW (*cf.* section 5.2.2). Using quasi-geostrophic scalings for horizontal velocity and pressure, the cross-over scale is determined by the magnitude of the mesoscale eddies Rossby number (Ro) with respect to the β-parameter (Eq. 15). The definition of the cross-over scale is not unique and changes with the scaling of Ro. Using $Ro = \frac{U'}{fL}$ (instead of $Ro = \zeta'_{RMS}f$ in section 5.2.2), we define an alternative cross-over scale, which corresponds to the Rhines scale ($Rh = \frac{1}{H}\int_{-H}^{\eta}\left(\sqrt{\frac{||\mathbf{u}'||}{\beta}}\right)\,dz$, with $||\mathbf{u}'||$ the magnitude of mesoscale eddies velocity).

In the quasi-geostrophic theory, the Rhines scale marks the transition from an advectively-dominated (nonlinear) dynamical regime ($Rh >> L$; with L the characteristic length scale of eddies) to a Rossby waves-dominated (linear) dynamical regime ($Rh << L$) (Rhines, 1975). This definition of the cross-over scale shows that evaluating the dominant regime of the mesoscale EPW is therefore similar to evaluating the mesoscale eddies dynamical regime.

In the Agulhas Current region, the typical values of the Rhines scale support the conclusions arising from the version of the cross-over scale presented in the study (Eq. 15 and Figure 3b). The Rhines scale indicates that mesoscale eddies fall in the range of large coupled geostrophic-ageostrophic EPW with respect to the linear β-contribution (Rh in $O(1.5\text{–}3)Rd$ in 70% of the WB region and larger values at the inner front; Figure D1). This results shows that in the WB region of the Agulhas Current, mesoscale eddies fall in the range of large coupled geostrophic-ageostrophic flux — with respect to linear β-effect — as a result of mesoscale eddies being characterized by a nonlinear dynamical regime ($Rh >> Rd$) — and not a linear wave dynamical regime ($Rh << L$) —. Nonlinear dynamics of mesoscale eddies has been characterized from satellite altimetry data, as documented by Chelton et al. (2011).

Open Research Section

WOES36 model outputs are available online at http://dap.saeon.ac.za/thredds/catalog/SAEON.EGAGASINI/2019.Penven/DAILY_MEANS/1_36_degree/catalog.html The AVISO data are available at www.aviso.altimetry.fr, the WOA18 and WOCE climatologies are available at www.nodc.noaa.gov/OC5/woa18/ and https://icdc.cen.uni-hamburg.de/thredds/catalog/ftpthredds/woce/catalog.htm.

Acknowledgments

This work was granted access to the HPC resources of IDRIS under the allocation A0040107630 made by GENCI at Paris, France, and of the HPC facilities DATARMOR of “Pôle de Calcul Intensif pour la Mer” at Ifremer, Brest, France. This work was supported by the Ifremer and the Brittany region for PhD funding. We also gratefully acknowledge support from the French National Agency for Research (ANR) through the projects DEEPER (ANR-19-CE01-0002-01) and the project DIEGO of the CNES/TOSCA SWOT program.

References

Adcock, S., & Marshall, D. (2000). Interactions between geostrophic eddies and the mean circulation over large-scale bottom topography. *Journal of physical oceanography*, *30*(12), 3223–3238.

Capó, E., Orfila, A., Mason, E., & Ruiz, S. (2019). Energy conversion routes in the western mediterranean sea estimated from eddy–mean flow interactions. *Journal of Physical Oceanography*, *49*(1), 247–267.

Chelton, D., Deszoeke, R., Schlax, M., El Naggar, K., & Siwertz, N. (1998). Geographical variability of the first baroclinic Rossby radius of deformation. *Journal of Physical Oceanography*, *28*(3), 433–460.

Chelton, D., Schlax, M., & Samelson, R. (2011). Global observations of nonlinear mesoscale eddies. *Progress in oceanography*, *91*(2), 167–216.

Chelton, D., Schlax, M., Samelson, R., & de Szoeke, R. (2007). Global observations of large oceanic eddies. *Geophysical Research Letters*, *34*(15).

Chen, R., Flierl, G., & Wunsch, C. (2014). A description of local and nonlocal eddy–mean flow interaction in a global eddy-permitting state estimate. *Journal of Physical Oceanography*, *44*(9), 2336–2352.

Cushman-Roisin, B., & Beckers, J.-M. (2011). *Introduction to geophysical fluid dynamics: physical and numerical aspects*. Academic press.

Debreu, L., Marchesiello, P., Penven, P., & Chambon, G. (2012). Two-way nesting in split-explicit ocean models: Algorithms, implementation and validation. *Ocean Modelling*, *49-50*, 1-21.

Ducet, N., Traon, P.-Y. L., & Reverdin, G. (2000). Global high-resolution mapping of ocean circulation from TOPEX/Poseidon and ERS-1 and-2. *Journal of Geophysical Research: Oceans*, *105*(C8), 19477–19498.

Elipot, S., & Beal, L. M. (2015). Characteristics, Energetics, and Origins of Agulhas Current Meanders and Their Limited Influence on Ring Shedding. *Journal of Physical Oceanography*, *45*(9), 2294-2314. doi: 10.1175/JPO-D-14-0254.1

Evans, D., Frajka-Williams, E., & Garabato, A. N. (2022). Dissipation of mesoscale eddies at a western boundary via a direct energy cascade. *Scientific Reports*, *12*(1), 1–13.

Evans, D., Frajka-Williams, E., Garabato, A. N., Polzin, K., & Forryan, A. (2020). Mesoscale eddy dissipation by a 'zoo' of submesoscale processes at a western boundary. *Journal of Geophysical Research: Oceans*, e2020JC016246.

Ferrari, R., & Wunsch, C. (2009). Ocean circulation kinetic energy: Reservoirs, sources, and sinks. *Annual Review of Fluid Mechanics*, *41*.

Gill, A. (1982). *Atmosphere-ocean dynamics (international geophysics series)*. academic press.

Gill, A., Green, J., & Simmons, A. (1974). Energy partition in the large-scale ocean circulation and the production of mid-ocean eddies. *Deep sea research and oceanographic abstracts*, *21*(7), 499–528.

Gouretski, V., & Koltermann, K. (2004). WOCE global hydrographic climatology. *Berichte des BSH*, *35*, 1–52.

Gula, J., Molemaker, M., & McWilliams, J. (2015). Gulf Stream dynamics along the Southeastern U.S. Seaboard. *J. Phys. Oceanogr.*, *45*(3), 690-715.

Halo, I., Penven, P., Backeberg, B., Ansorge, I., Shillington, F., & Roman, R. (2014). Mesoscale eddy variability in the southern extension of the East Madagascar Current: Seasonal cycle, energy conversion terms, and eddy mean properties. *Journal of Geophysical Research: Oceans*, *119*(10), 7324–7356.

Harrison, D. E., & Robinson, A. R. (1978). Energy analysis of open regions of turbulent flows—Mean eddy energetics of a numerical ocean circulation experiment. *Dynamics of Atmospheres and Oceans*, *2*(2), 185–211.

Holloway, G. (1987). Systematic forcing of large-scale geophysical flows by eddy-topography interaction. *Journal of Fluid Mechanics*, *184*, 463–476.

Jamet, Q., Deremble, B., Wienders, N., Uchida, T., & Dewar, W. (2021). On wind-driven energetics of subtropical gyres. *Journal of Advances in Modeling Earth Systems*, *13*(4), e2020MS002329.

Kang, D., & Curchitser, E. (2015). Energetics of eddy–mean flow interactions in the Gulf Stream region. *Journal of Physical Oceanography*, *45*(4), 1103–1120.

Kelly, S. (2016). The vertical mode decomposition of surface and internal tides in the presence of a free surface and arbitrary topography. *Journal of Physical Oceanography*, *46*(12), 3777–3788.

Kelly, S., Nash, J., & Kunze, E. (2010). Internal-tide energy over topography. *Journal of Geophysical Research: Oceans*, *115*(C6).

Kelly, S., Nash, J., Martini, K., Alford, H. M., & Kunze, E. (2012). The cascade of tidal energy from low to high modes on a continental slope. *Journal of physical oceanography*, *42*(7), 1217–1232.

Li, J., Roughan, M., & Kerry, C. (2021). Dynamics of interannual eddy kinetic energy modulations in a western boundary current. *Geophysical Research Letters*, e2021GL094115.

Lutjeharms, J. (2006). *The Agulhas Current* (Vol. 2). Springer.

Lutjeharms, J., Boebel, O., & Rossby, H. (2003). Agulhas cyclones. *Deep Sea Research Part II: Topical Studies in Oceanography*, *50*(1), 13–34.

Lutjeharms, J., Penven, P., & Roy, C. (2003). Modelling the shear edge eddies of the southern agulhas current. *Continental Shelf Research*, *23*(11-13), 1099–1115.

Masuda, A. (1978). Group velocity and energy transport by Rossby waves. *Journal of Oceanography*, *34*(1), 1–7.

Müller, P., McWilliams, J., & Molemaker, M. (2005). *Routes to dissipation in the ocean: The 2D/3D turbulence conundrum.* Cambridge University Press Cambridge.

Nikurashin, M., & Ferrari, R. (2010). Radiation and dissipation of internal waves generated by geostrophic motions impinging on small-scale topography: Theory. *Journal of Physical Oceanography*, *40*(5), 1055–1074.

Perfect, B., Kumar, N., & Riley, J. (2020). Energetics of Seamount Wakes. Part I: Energy Exchange. *Journal of Physical Oceanography*, *50*(5), 1365–1382.

Rhines, P. (1975). Waves and turbulence on a beta-plane. *Journal of Fluid Mechanics*, *69*(3), 417–443.

Schubert, R., Gula, J., & Biastoch, A. (2021). Submesoscale flows impact Agulhas leakage in ocean simulations. *Communications Earth & Environment*, *2*(1), 1–8.

Schubert, R., Gula, J., Greatbatch, R., Baschek, B., & Biastoch, A. (2020). The Submesoscale Kinetic Energy Cascade: Mesoscale Absorption of submesoscale Mixed Layer Eddies and Frontal Downscale Fluxes. *Journal of Physical Oceanography*, *50*(9), 2573–2589.

Scott, R., & Furnival, D. (2012). Assessment of traditional and new eigenfunction bases applied to extrapolation of surface geostrophic current time series to below the surface in an idealized primitive equation simulation. *Journal of physical oceanography*, *42*(1), 165–178.

Shchepetkin, A., & McWilliams, J. (2005). The Regional Oceanic Modeling System (ROMS): A split-explicit, free-surface, topography-following- coordinate ocean model. *Ocean Modelling*, *9*, 347-404.

Smith, K., & Vallis, G. (2001). The scales and equilibration of midocean eddies: Freely evolving flow. *Journal of Physical Oceanography*, *31*(2), 554–571.

Soufflet, Y., Marchesiello, P., Lemarié, F., Jouanno, J., Capet, X., Debreu, L., & Benshila, R. (2016). On effective resolution in ocean models. *Ocean Modelling*, *98*, 36–50.

Tedesco, P., Gula, J., Penven, P., & Ménesguen, C. (2022). Mesoscale Eddy Kinetic Energy budgets and transfers between vertical modes in the Agulhas Current. *Journal of Physical Oceanography*.

Venaille, A., Vallis, G., & Smith, K. (2011). Baroclinic turbulence in the ocean: Analysis with primitive equation and quasigeostrophic simulations. *Journal of Physical Oceanography*, *41*(9), 1605–1623.

Wunsch, C. (1997). The vertical partition of oceanic horizontal kinetic energy. *Journal of Physical Oceanography*, *27*(8), 1770–1794.

Wunsch, C. (2007). The past and future ocean circulation from a contemporary perspective. *Geophysical Monograph-American Geophysical Union*, *173*, 53.

Yan, X., Kang, D., Curchitser, E., & Pang, C. (2019). Energetics of eddy–mean flow interactions along the western boundary currents in the North Pacific. *Journal of Physical Oceanography*, *49*(3), 789–810.

Yang, Y., & Liang, X. S. (2016). The instabilities and multiscale energetics underlying the mean–interannual–eddy interactions in the Kuroshio Extension region. *Journal of Physical Oceanography*, *46*(5), 1477–1494.

Yang, Z., X., Z., Marshall, D., & Wang, G. (2021). An Idealized Model Study of Eddy Energetics in the Western Boundary "Graveyard". *Journal of Physical Oceanography*, *51*(4), 1265–1282.

Yankovsky, E., Zanna, L., & Smith, K. (2022). Influences of Mesoscale Ocean Eddies on Flow Vertical Structure in a Resolution-Based Model Hierarchy. *Earth and Space Science Open Archive*, 60. Retrieved from `https://doi.org/10.1002/essoar.10511501.1` doi: 10.1002/essoar.10511501.1

Zhai, X., Johnson, H., & Marshall, D. (2010). Significant sink of ocean-eddy energy near western boundaries. *Nature Geoscience*, *3*(9), 608.

Figure 1.

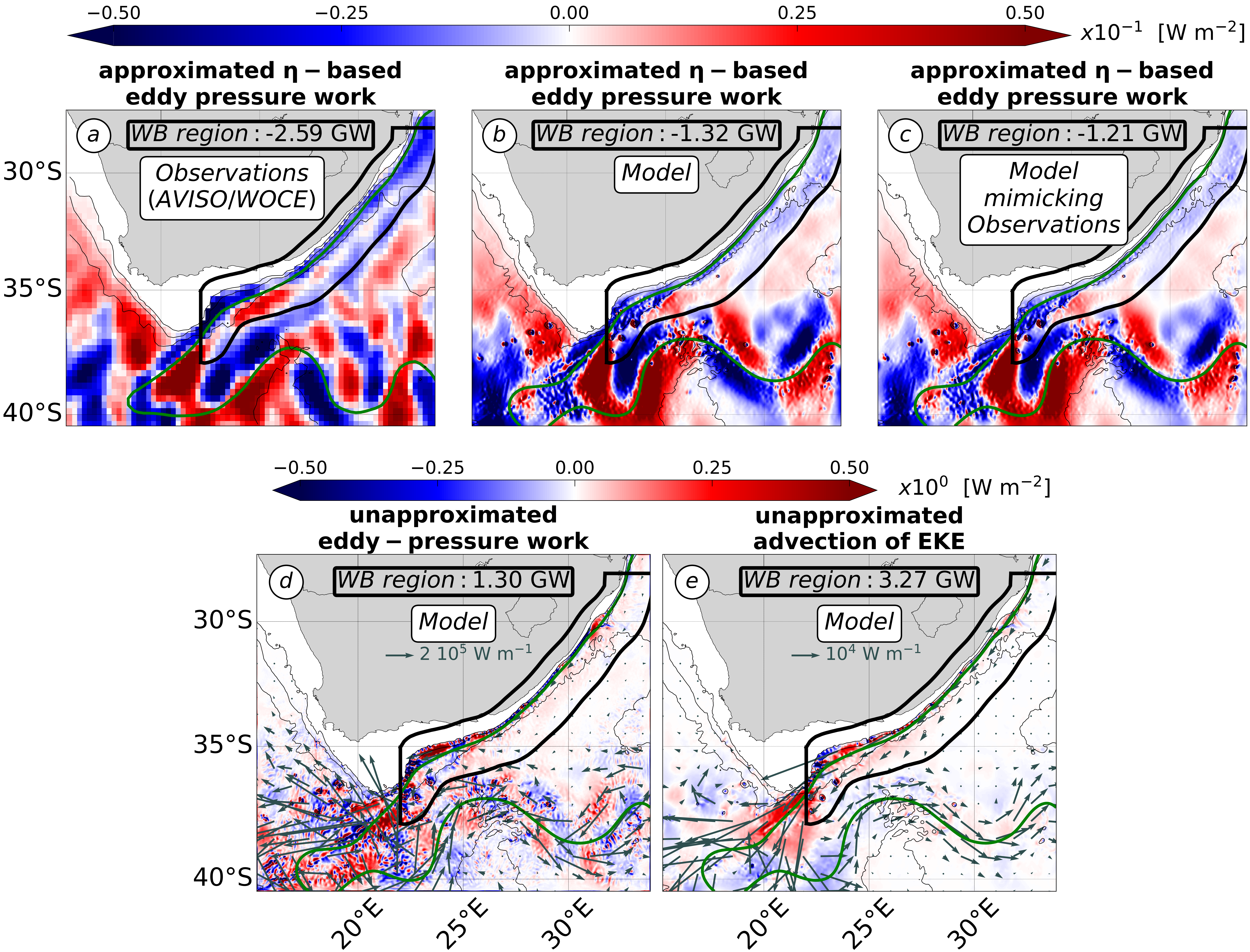

−0.50
−0.25
0.00
0.25
0.50
x10^{-1} [W m^{-2}]
approximated η − based eddy pressure work
WB region : -2.59 GW
Observations (AVISO/WOCE)
approximated η − based eddy pressure work
WB region : -1.32 GW
Model
approximated η − based eddy pressure work
WB region : -1.21 GW
Model mimicking Observations
30°S
35°S
40°S
a
b
c
−0.50
−0.25
0.00
0.25
0.50
x10^{0} [W m^{-2}]
unapproximated eddy − pressure work
WB region : 1.30 GW
Model
2 10^{5} W m^{-1}
unapproximated advection of EKE
WB region : 3.27 GW
Model
10^{4} W m^{-1}
d
e
20°E
25°E
30°E

Figure 2.

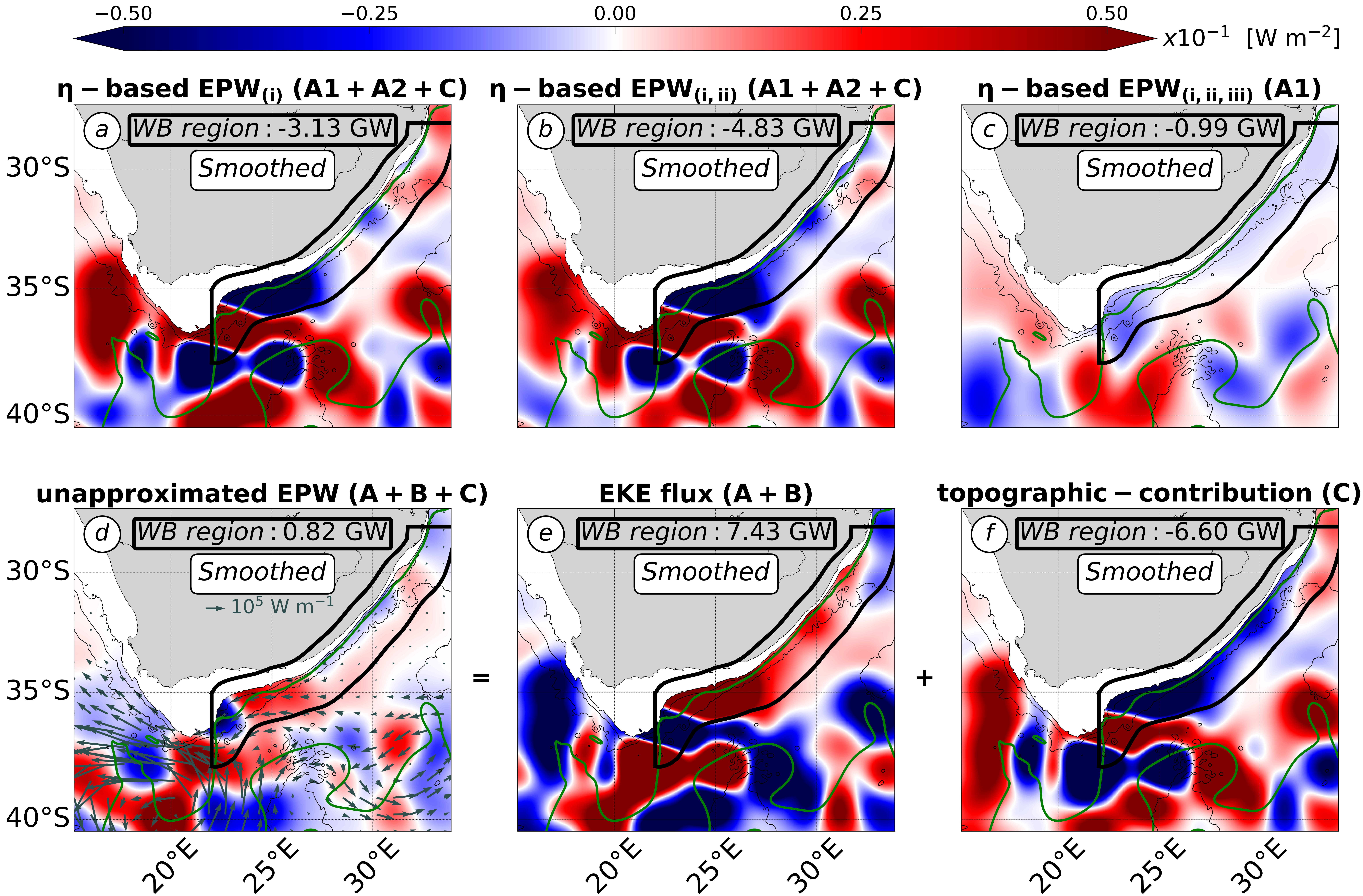
−0.50
−0.25
0.00
0.25
0.50
x10^{-1} [W m^{-2}]
η − based EPW$_{(i)}$ (A1 + A2 + C)
η − based EPW$_{(i, ii)}$ (A1 + A2 + C)
η − based EPW$_{(i, ii, iii)}$ (A1)
a
WB region : -3.13 GW
Smoothed
b
WB region : -4.83 GW
Smoothed
c
WB region : -0.99 GW
Smoothed
unapproximated EPW (A + B + C)
EKE flux (A + B)
topographic − contribution (C)
d
WB region : 0.82 GW
Smoothed
→ 10^5 W m^{-1}
e
WB region : 7.43 GW
Smoothed
f
WB region : -6.60 GW
Smoothed
=
+
30°S
35°S
40°S
20°E
25°E
30°E

Figure 3.

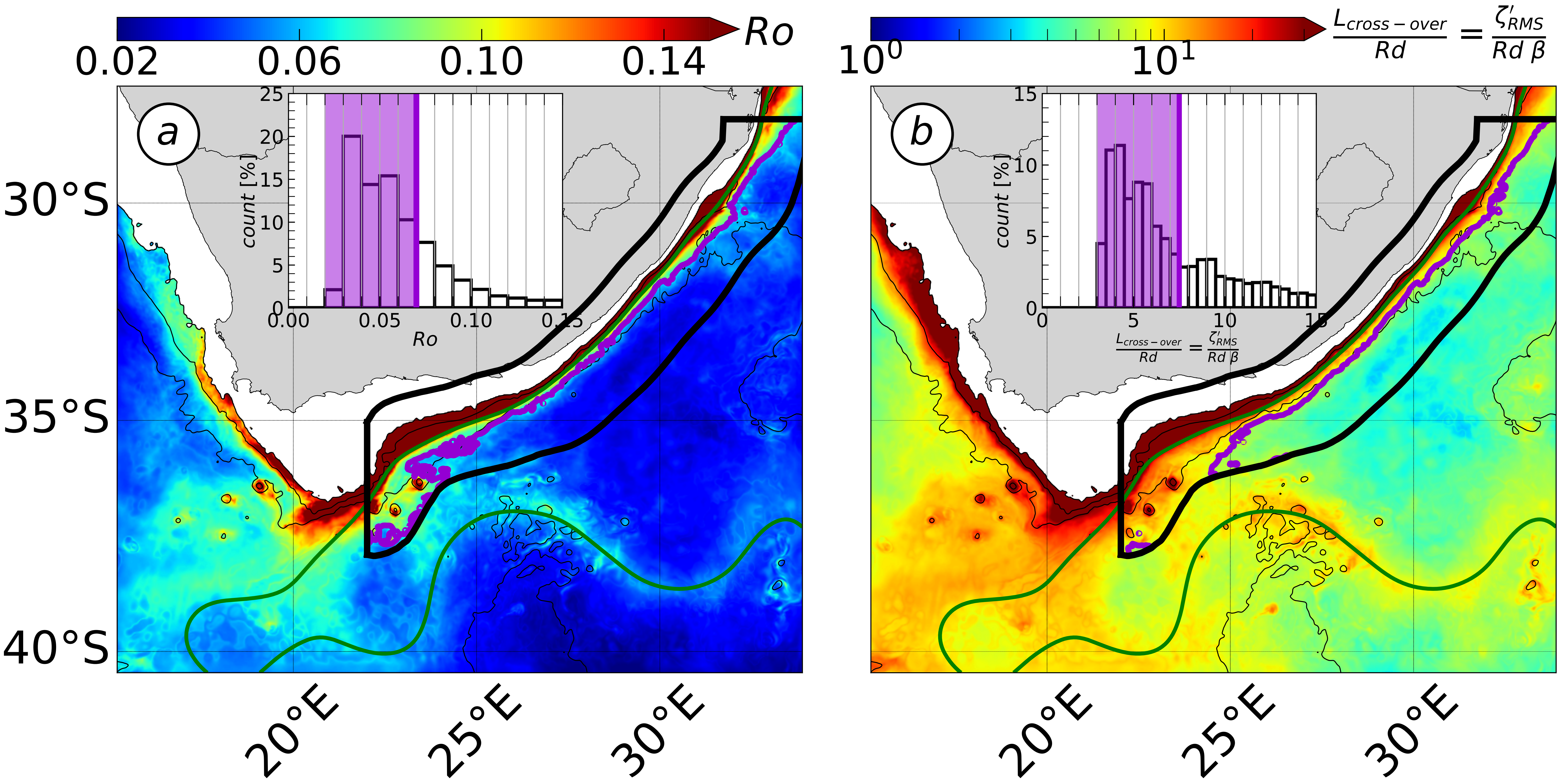

Ro
0.02
0.06
0.10
0.14
a
count [%]
Ro
30°S
35°S
40°S
20°E
25°E
30°E
$\frac{L_{cross-over}}{Rd} = \frac{\zeta'_{RMS}}{Rd\ \beta}$
10^0
10^1
b

Figure 4.

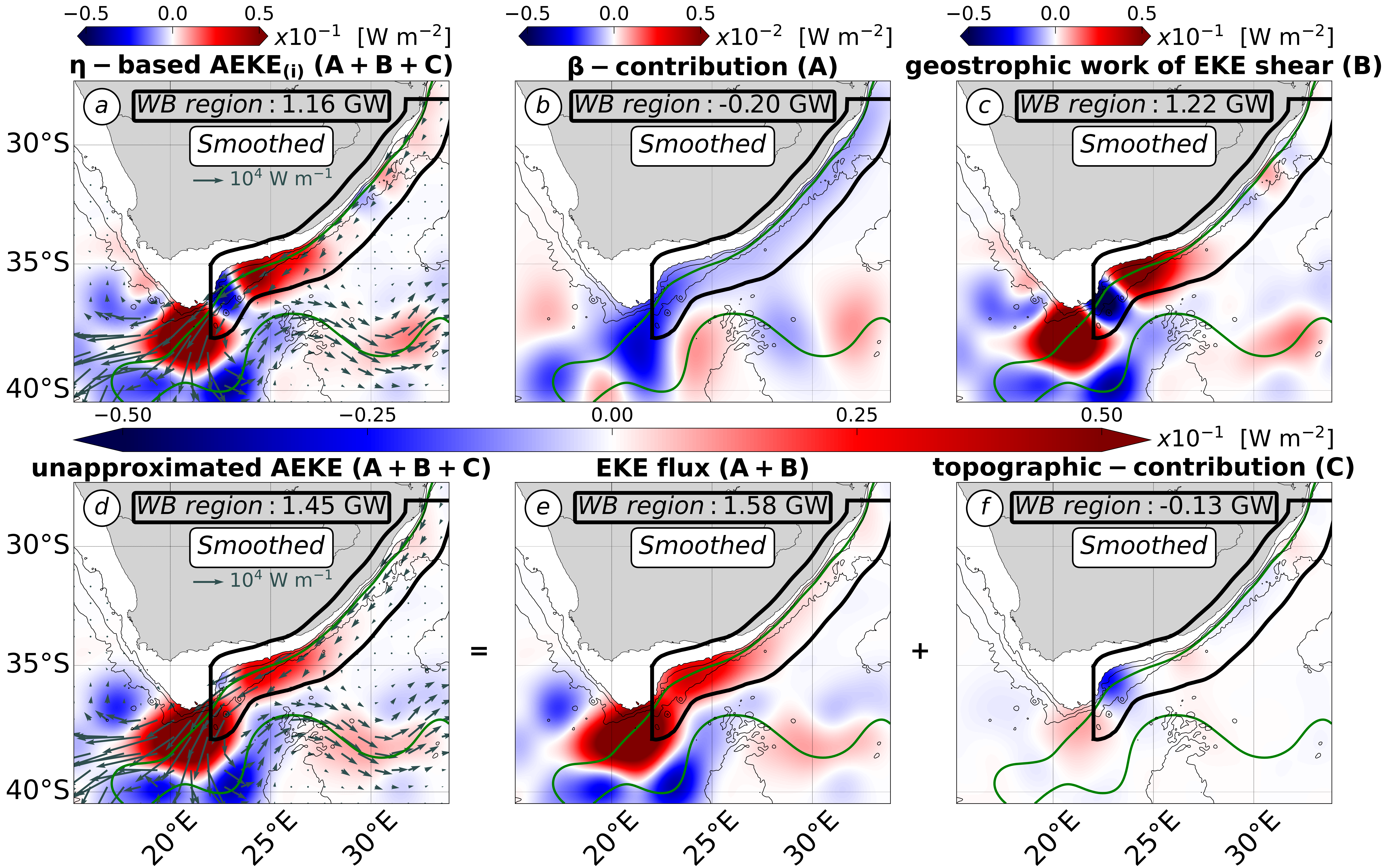

−0.5 0.0 0.5 x10−1 [W m−2]
η − based AEKE(i) (A + B + C)
−0.5 0.0 0.5 x10−2 [W m−2]
β − contribution (A)
−0.5 0.0 0.5 x10−1 [W m−2]
geostrophic work of EKE shear (B)
a
WB region : 1.16 GW
Smoothed
10^4 W m−1
b
WB region : -0.20 GW
Smoothed
c
WB region : 1.22 GW
Smoothed
30°S
35°S
40°S
−0.50 −0.25 0.00 0.25 0.50 x10−1 [W m−2]
unapproximated AEKE (A + B + C)
EKE flux (A + B)
topographic − contribution (C)
d
WB region : 1.45 GW
Smoothed
10^4 W m−1
=
e
WB region : 1.58 GW
Smoothed
+
f
WB region : -0.13 GW
Smoothed
20°E
25°E
30°E

Figure 5.

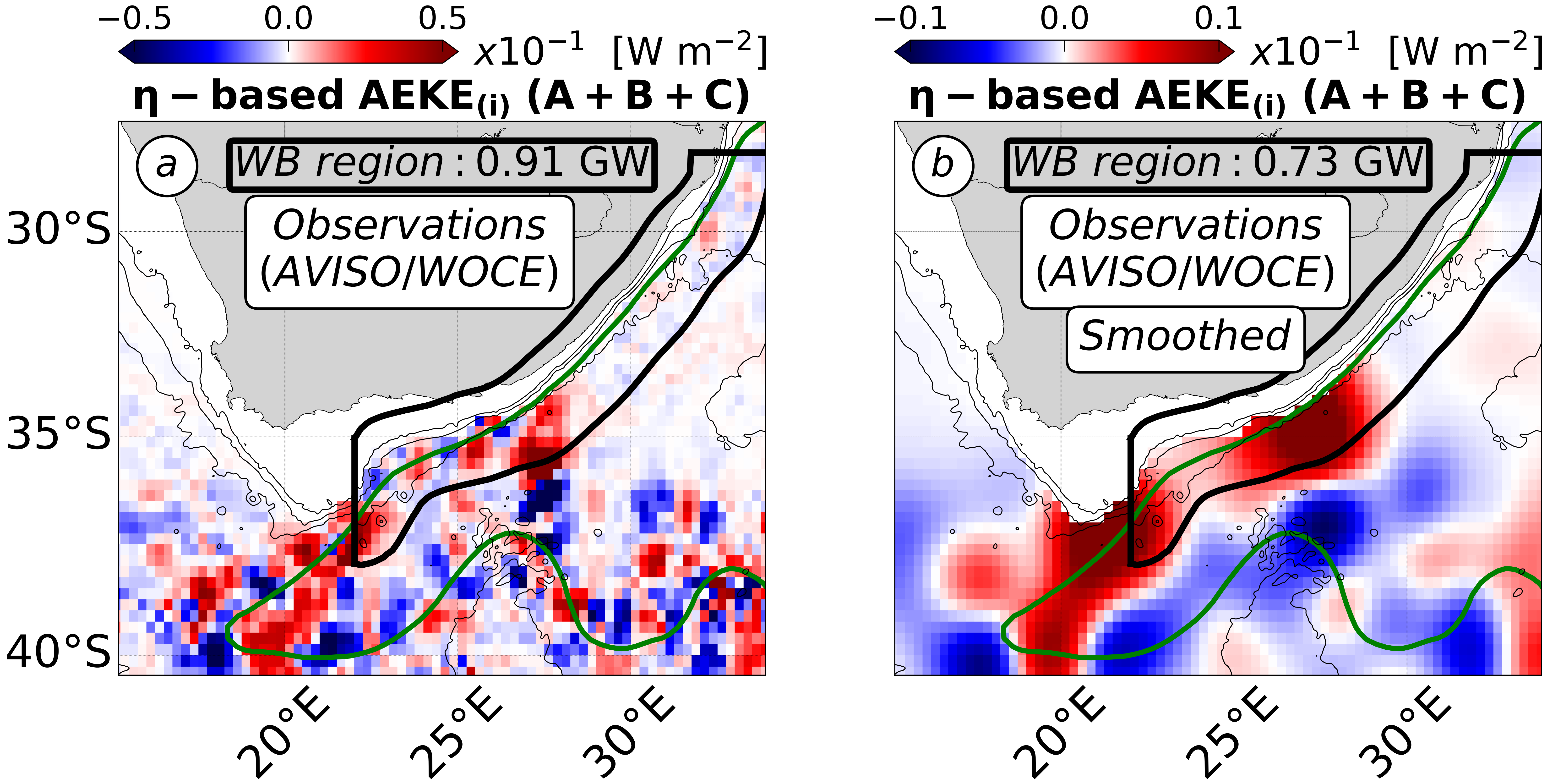

−0.5
0.0
0.5
x10^{-1} [W m^{-2}]
η − based AEKE(i) (A + B + C)
a
WB region : 0.91 GW
Observations (AVISO/WOCE)
30°S
35°S
40°S
20°E
25°E
30°E
−0.1
0.0
0.1
x10^{-1} [W m^{-2}]
η − based AEKE(i) (A + B + C)
b
WB region : 0.73 GW
Observations (AVISO/WOCE)
Smoothed
20°E
25°E
30°E

Figure A.

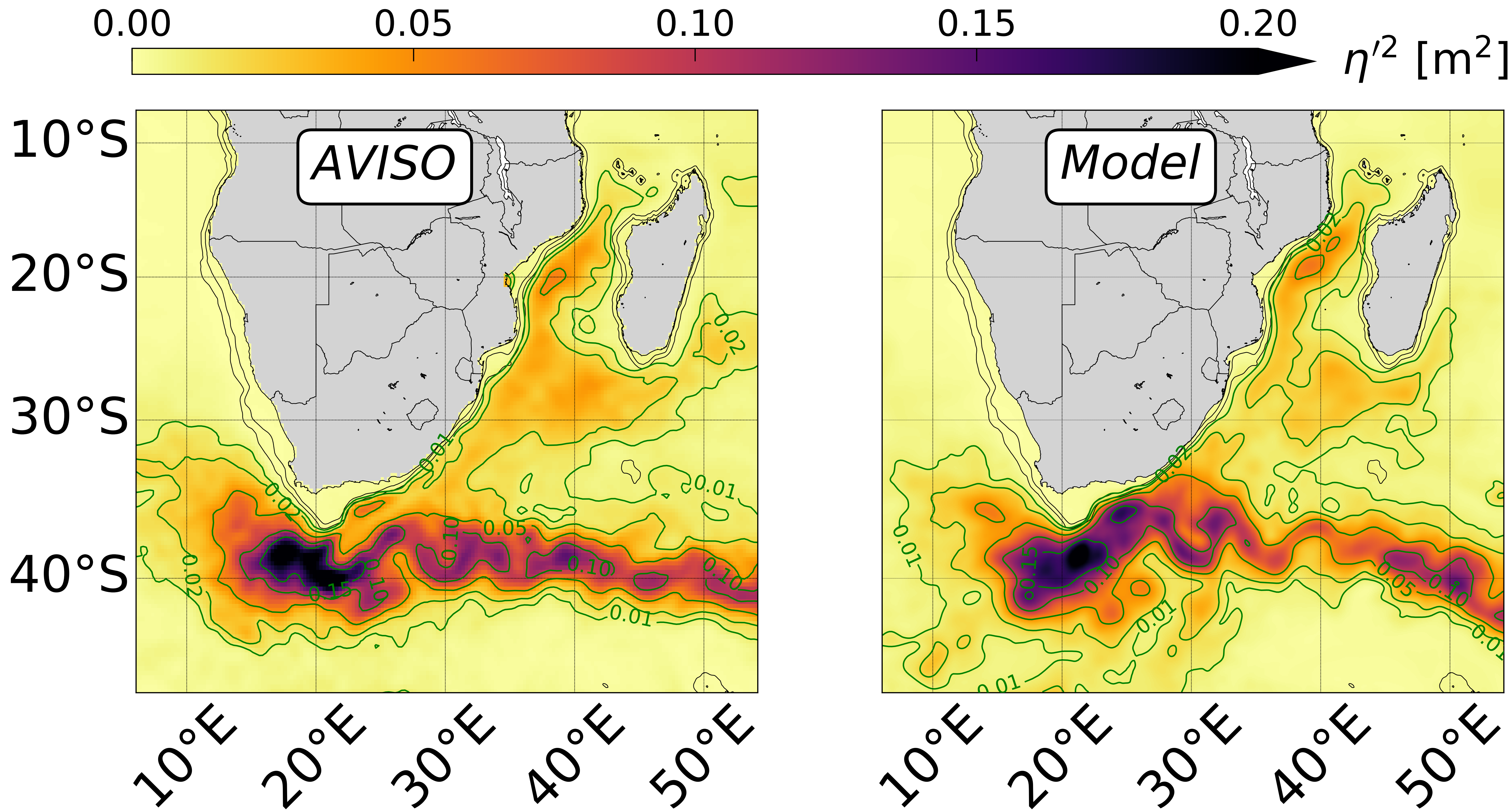

0.00
0.05
0.10
0.15
0.20
η'^2 [m^2]
AVISO
Model
10°S
20°S
30°S
40°S
10°E
20°E
30°E
40°E
50°E
0.01
0.02
0.05
0.10
0.15

Figure B.

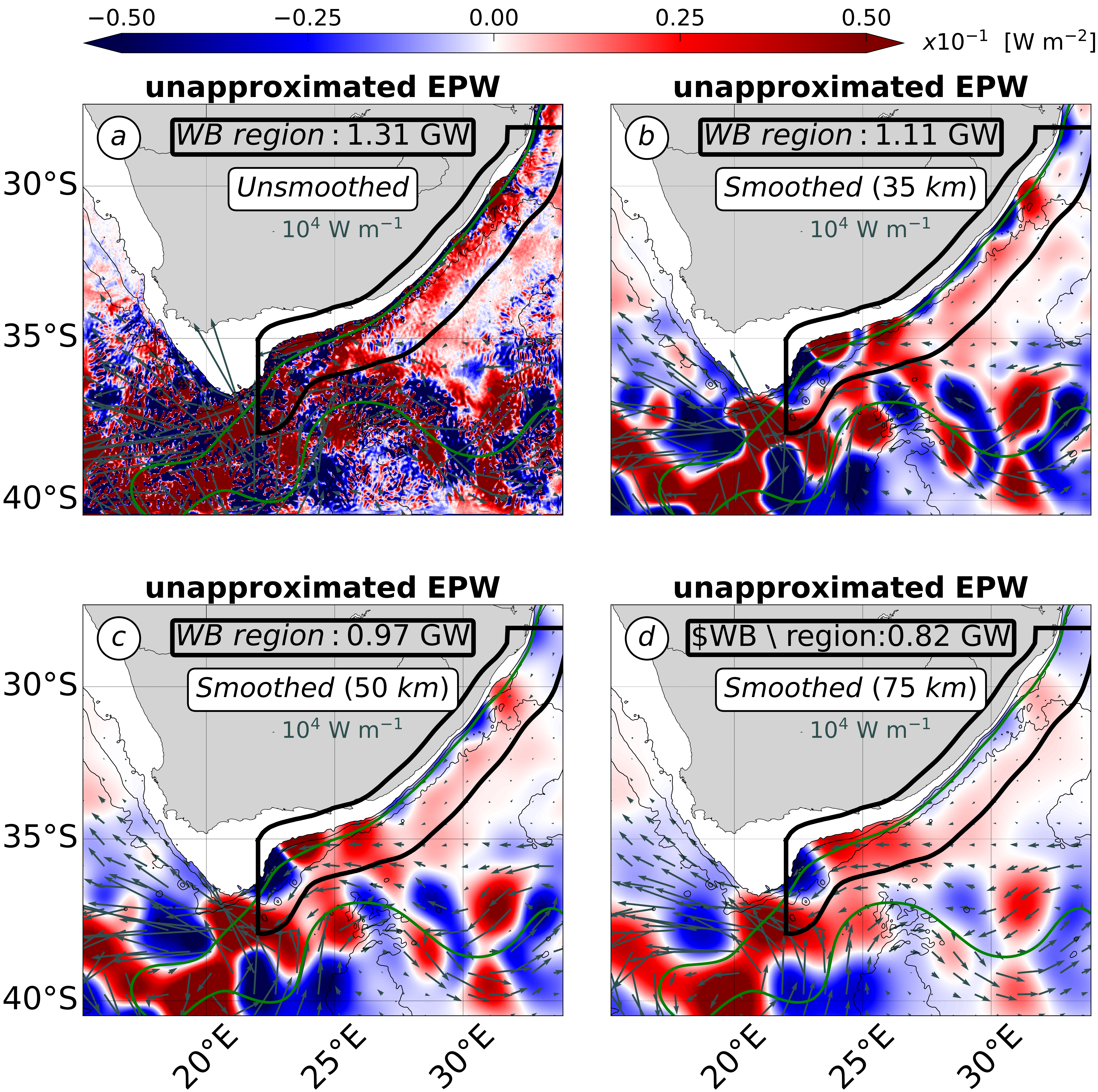
−0.50
−0.25
0.00
0.25
0.50
x10^−1 [W m^−2]
unapproximated EPW
a
WB region : 1.31 GW
Unsmoothed
10^4 W m^−1
unapproximated EPW
b
WB region : 1.11 GW
Smoothed (35 km)
10^4 W m^−1
unapproximated EPW
c
WB region : 0.97 GW
Smoothed (50 km)
10^4 W m^−1
unapproximated EPW
d
$WB \ region:0.82 GW
Smoothed (75 km)
10^4 W m^−1
30°S
35°S
40°S
20°E
25°E
30°E

Figure C.

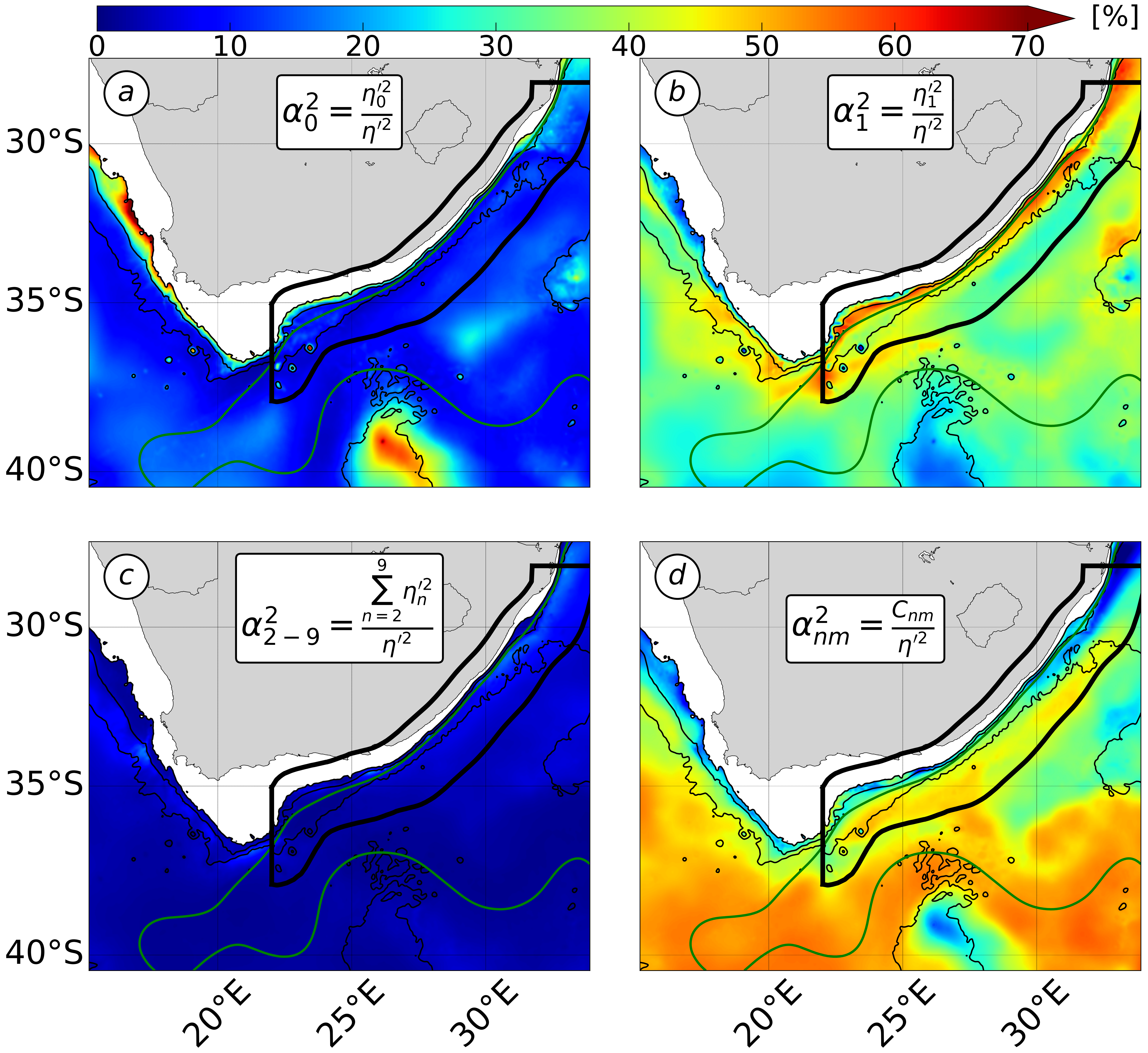

0
10
20
30
40
50
60
70
[%]
a
$\alpha_0^2 = \frac{\eta_0'^2}{\eta'^2}$
b
$\alpha_1^2 = \frac{\eta_1'^2}{\eta'^2}$
c
$\alpha_{2-9}^2 = \frac{\sum_{n=2}^{9} \eta_n'^2}{\eta'^2}$
d
$\alpha_{nm}^2 = \frac{C_{nm}}{\eta'^2}$
30°S
35°S
40°S
20°E
25°E
30°E

Figure D.

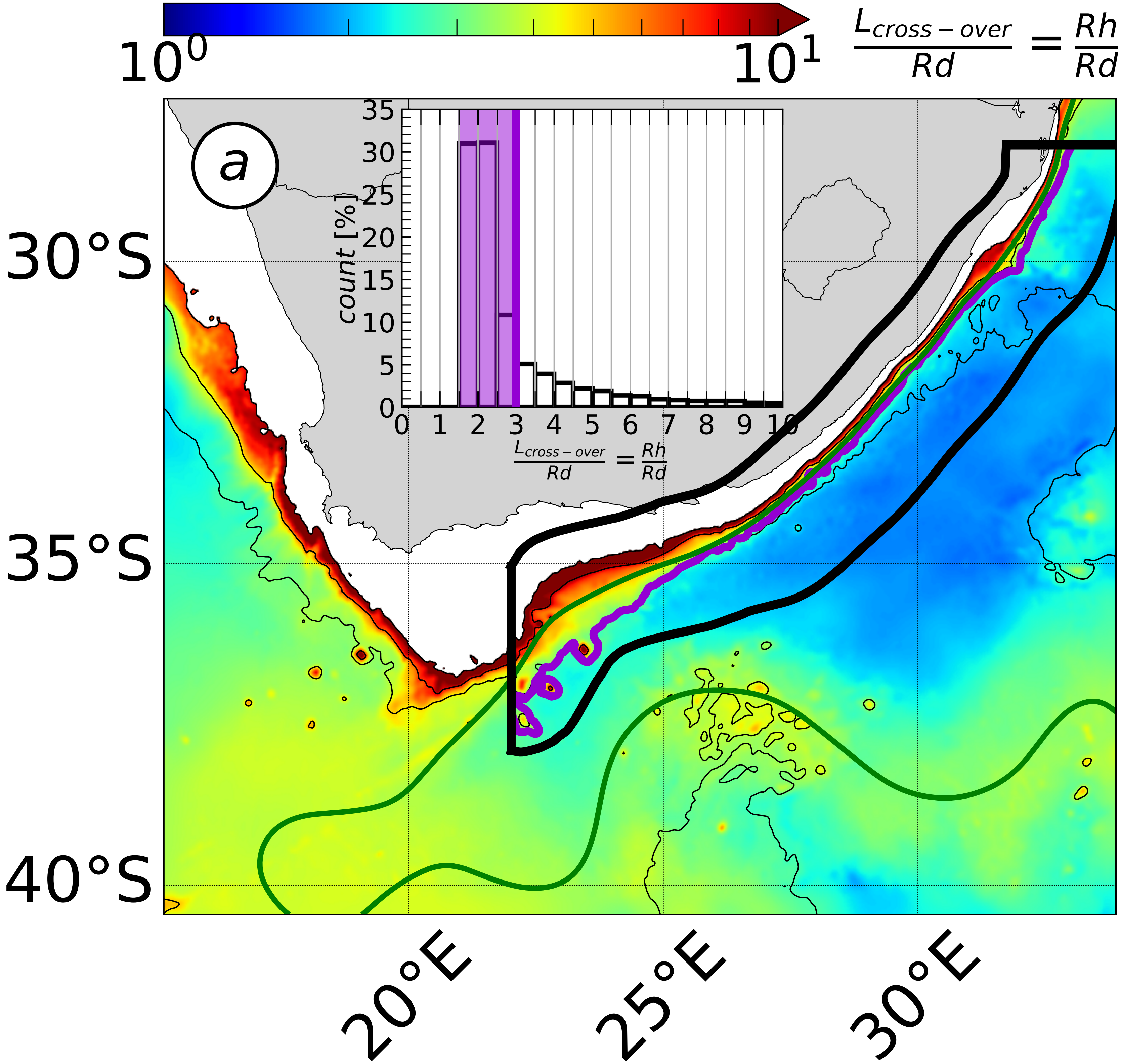

10^0
10^1
$\frac{L_{cross-over}}{Rd} = \frac{Rh}{Rd}$
a
30°S
35°S
40°S
20°E
25°E
30°E
count [%]
35
30
25
20
15
10
5
0
0 1 2 3 4 5 6 7 8 9 10
$\frac{L_{cross-over}}{Rd} = \frac{Rh}{Rd}$

Can mesoscale eddy kinetic energy sources and sinks be inferred from sea surface height in the Agulhas Current region?

P. Tedesco[1,2], J. Gula[1,3], P. Penven[1], C. Ménesguen[1], Q. Jamet[4], C. Vic[1]

[1]Univ. Brest, CNRS, IRD, Ifremer, Laboratoire d'Océanographie Physique et Spatiale (LOPS), IUEM, 29280, Brest, France.
[2]University of Cambridge, Cambridge, UK.
[3]Institut Universitaire de France (IUF), Paris, France.
[4]INRIA, ODYSSEY group, Ifremer, Plouzané, France.

Key Points:

- We assess whether the mesoscale eddy energy flux divergence can be calculated from sea surface height in the Agulhas Current region
- Geostrophy allows a qualitative estimate of eddy energy advection, but not of eddy pressure work
- This favours the use of sea surface height, but challenges the founding approximations of an earlier paradigm

Corresponding author: Pauline Tedesco, `pfmt2@cam.ac.uk`

Abstract

Western boundaries have been suggested as mesoscale eddy graveyards, using a diagnostic of the eddy kinetic energy (EKE) flux divergence based on sea surface height (η). The graveyard's paradigm relies on the approximation of geostrophy — required by the use of η — and other approximations that support long baroclinic Rossby waves as the dominant contribution to the EKE flux divergence. However, a recent study showed an opposite paradigm in the Agulhas Current region using an unapproximated EKE flux divergence. Here, we assess the validity of the approximations used to derive the η-based EKE flux divergence using a regional numerical simulation of the Agulhas Current. The EKE flux divergence consists of the eddy pressure work (EPW) and the EKE advection ($AEKE$). We show that geostrophy is valid for inferring $AEKE$, but that all approximations are invalid for inferring EPW. A scale analysis shows that at mesoscale (L > $O(30)$ km), EPW is dominated by coupled geostrophic-ageostrophic EKE flux and that Rossby waves effect is weak. There is also a hitherto neglected topographic contribution, which can be locally dominant. $AEKE$ is dominated by the geostrophic EKE flux, which makes a substantial contribution (54%) to the net regional mesoscale EKE source represented by the EKE flux divergence. Other contributions, including topographic and ageostrophic effects, are also significant. Our results support the use of η to infer a qualitative estimate of the EKE flux divergence in the Agulhas Current region. However, they invalidate the approximations on mesoscale eddy dynamics that underlie the graveyard's paradigm.

Plain Language Summary

In the ocean, the most energetic motions are large-scale eddies with horizontal scales ranging from tens to hundreds of kilometers. These are major components of the ocean energy budget, and unravelling their lifecycles is crucial to improving our understanding of ocean dynamics. Although the generation of large-scale eddies is well documented, how their energy is dissipated remains uncertain. Based on satellite observations of the sea surface and approximations to the dynamics of large-scale eddies, it has been suggested that they decay at western boundaries of oceanic basins, thereby closing their lifecycle. However, based on different data and approximations, a recent study has suggested that large-scale eddies are predominantly generated in a specific western boundary region, such as the Agulhas Current. Our study explains which of the data (sea surface observations) or the assumed leading order dynamics (approximations) explains the opposite eddy energy sources and sinks shown by the two studies in the Agulhas Current region. Our results show that the use of sea surface observations is valid for qualitatively inferring the regional eddy energy source, but not the assumed leading order dynamics. This has implications for (1) our understanding and (2) study strategies of the energetics of large-scale eddies.

1 Introduction

Mesoscale eddies account for 80 % of the surface kinetic energy and are a key component of the global ocean energy budget (Wunsch, 2007; Ferrari & Wunsch, 2009; Müller et al., 2005). They have horizontal scales of the order of the 1^{st} Rossby deformation radius (Rd) or larger (Chelton et al., 2011). At these scales, the velocity field can be decomposed into a leading order geostrophic and a weaker ageostrophic component, following the quasi-geostrophic theory (Gill, 1982). Geostrophic flows are horizontally divergence-free flows — in a local approximation — dominated by the effects of rotation compared to advection (Rossby number : $Ro \ll 1$) and stratification compared to vertical shear (Richardson number : $Ri \gg 1$). Ageostrophic flows account for variations in the geostrophically balanced system. They are characterized by a large vertical component and the increasing effects of advection.

Mesoscale eddies are easily tracked by satellite altimetry, which measures sea surface height (η) and whose low-frequency component is an indirect measure of surface geostrophic currents. Satellite altimetry has shown that mesoscale eddies are ubiquitous in the oceans and that they are most energetic in western boundary currents and in the Antarctic Circumpolar Current (Ducet et al., 2000; Chelton et al., 2007, 2011). This identifies these regions as key to the global ocean energy budget.

Using satellite altimetry data, Zhai et al. (2010) suggested western boundaries as mesoscale eddy kinetic energy (EKE) sinks. In the energy budget, sources and sinks of eddy kinetic energy (EKE) are accounted for by the EKE flux divergence term (Harrison & Robinson, 1978). This term represents the rate of EKE transport done by: the work of pressure fluctuations (eddy pressure work; usually interpreted as the linear contribution from waves) and the nonlinear advection of EKE by mean and eddy flows. When ocean dynamics are in equilibrium, the EKE flux divergence indicates a net EKE source (>0) or sink (<0).

Zhai et al. (2010) explicitly developed a η-based diagnostic of the mesoscale eddy pressure work (linear component of the EKE flux divergence) using several approximations. Their diagnosis reduces to the linear contribution of the β-effect, corresponding in particular to the propagation of long Rossby waves. Figure 1a shows Zhai et al. (2010)'s version of the eddy pressure work in the Agulhas Current region, which they suggested to be the largest mesoscale EKE sink. The approximated η-based eddy pressure work indicates an almost uniform mesoscale EKE sink (<0) at the western boundary (WB; black domain), whose cumulative value is of $O(1)$ GW (Figure 1a).

Their result would establish the following paradigm: mesoscale eddies originate almost everywhere in the ocean, propagate westward at about the speed of long baroclinic Rossby waves, and decay at western boundaries, probably through direct energy routes to dissipation, channeled by topography (Gill et al., 1974; Zhai et al., 2010; Chelton et al., 2011; Evans et al., 2022). This scenario is supported in regions free of western boundary currents, by *in situ* measurements and idealized numerical simulations (Evans et al., 2020; Z. Yang et al., 2021; Evans et al., 2022). However, in regions containing western boundary currents, model-based studies suggest more complex mesoscale eddy dynamics. Western boundaries are hotspots for mesoscale eddy generation due to instabilities of the western boundary currents (Halo et al., 2014; Kang & Curchitser, 2015; Gula et al., 2015; Y. Yang & Liang, 2016; Yan et al., 2019; Li et al., 2021; Jamet et al., 2021; Tedesco et al., 2022).

In particular, a recent study has shown that the Agulhas Current region is a mesoscale EKE source using an unapproximated EKE flux divergence performed from a model (Tedesco et al., 2022). Figure 1d,e shows the unapproximated eddy pressure work and advection of EKE (forming the EKE flux divergence) computed from 3-dimensional modeled mesoscale velocities (Tedesco et al., 2022). Both unapproximated terms differ significantly from the approximated η-based eddy pressure work, with their magnitudes being larger of an order and their scale patterns smaller (Figure 1d,e). In the WB region of the Agulhas

Current, the two unapproximated terms are the most intense on the shelf — over a band narrower than the WB width — and have locally comparable magnitudes. Their cumulative value represents a mesoscale EKE source (>0), whose main contribution is due to the advection of EKE.

The opposite mesoscale EKE sources and sinks supported in the Agulhas Current region by the different versions of the EKE flux divergence (Figure 1a,d,e reproducing Zhai et al., 2010; Tedesco et al., 2022), challenge (1) the hypothesis that long baroclinic Rossby waves are the main contributors to the mesoscale EKE flux divergence, and thus (2) the approximations used to derive the η-based term. In this study, we focus on explaining the differences between the approximated η-based and the unapproximated model-based EKE flux divergence in the Agulhas Current region. We discuss below the approximations used by Zhai et al. (2010) and their implications:

(i) **Mesoscale EKE flux divergence is mainly due to geostrophic flows**
The geostrophic approximation is required when using satellite altimetry data. Geostrophy is a good approximation to infer mesoscale eddy velocities, which have small Rossby numbers ($Ro = O(\ll 0.05)$; Chelton et al., 2011). However, the use of geostrophic velocities to infer the mesoscale EKE flux divergence — a tendency term of the EKE budget that represents the rate of spatial redistribution of the mesoscale EKE reservoir (Harrison & Robinson, 1978) — is a separate issue.

(ii) **The vertical structure of mesoscale eddies is represented by the 1^{st} baroclinic mode**
The sea surface height (η) is usually interpreted as primarily reflecting surface-intensified vertical structures represented by the 1^{st} baroclinic mode. However, the mesoscale EKE reservoir is represented by the combination of the barotropic and 1^{st} baroclinic modes (Wunsch, 1997; Smith & Vallis, 2001; Venaille et al., 2011). The partitioning between the two vertical modes varies regionally, from being close to equipartition to being dominated by one of the modes (Tedesco et al., 2022; Yankovsky et al., 2022). The contributions of the barotropic and 1^{st} baroclinic modes to the mesoscale EKE flux divergence remain unknown to our knowledge. Their individual contributions can possibly transport EKE in a decoupled (coupled) manner, which would then compensate (accumulate) when considering the EKE flux divergence for the mesoscale reservoir.

(iii) **Mesoscale EKE flux interactions with topography are weak**
The approximation of weak topographic interactions is equivalent to assuming that the mesoscale EKE flux has spatial variations larger than those of topography (Zhai et al., 2010). This approximation is challenged by (1) the large topographic gradients at western boundaries ($1 \cdot 10^{-2} \pm 2 \cdot 10^{-2}$ in the Agulhas Current region) and (2) the strong topographic control on mesoscale eddy dynamics at western boundaries. Topography controls the triggering of current' instabilities that generate mesoscale eddies (Lutjeharms, 2006; Gula et al., 2015) and helps to channel energy transfers between mesoscale eddies and other types of flow (Adcock & Marshall, 2000; Nikurashin & Ferrari, 2010; Evans et al., 2020; Perfect et al., 2020; Tedesco et al., 2022). The contribution of topography to the mesoscale EKE flux divergence remains, to our knowledge, an open question.

In summary, opposing paradigms of mesoscale eddy dynamics are supported by two versions of the diagnosis of the EKE flux divergence in the western boundary region of the Agulhas Current (Zhai et al., 2010; Tedesco et al., 2022). The two diagnoses differ in method (η field measured by satellite altimetry *vs.* modeled 3-dimensional velocities) and assumed leading order contribution to the EKE flux divergence (long baroclinic Rossby waves as a result of approximations (i), (ii) and (iii) *vs.* no approximations to account for geostrophic, ageostrophic and topographic contributions acting on the barotropic and 1^{st}

baroclinic mode). The two contradictory diagnoses of mesoscale EKE source and sink suggest that either the method or the approximations lead to a misestimation of the mesoscale EKE flux divergence. This raises questions about the main contributions to the dynamics of the mesoscale eddy energy reservoir, and consequently, about strategies for studying mesoscale eddies. Open questions include: What are the main contributions – among geostrophic and ageostrophic effects, barotropic and 1^{st} baroclinic modes, and topographic contribution – to the eddy pressure work and advection of EKE? What are the implications for inferring the mesoscale EKE flux divergence using the η field? We focus in particular on determining whether approximation (i) of geostrophy is valid, as it is the only one formally required for the use of satellite altimetry to infer the mesoscale EKE flux divergence.

In the present study, we use a numerical simulation to evaluate the validity of approximation (i) for inferring the mesoscale EKE flux divergence in the region of the Agulhas Current. Our study is organized as follows. Unapproximated and η-based expressions of the eddy pressure work and advection of EKE (which form the EKE flux divergence) are presented in section 2. The regional numerical simulation is presented in section 3. The unapproximated and η-based versions of the eddy pressure work and advection of EKE are evaluated in sections 4, 5 and 6. Finally, we discuss our results in the larger context of altimetry-based diagnosis of mesoscale eddy dynamics at western boundaries in section 7.

2 Theory

In this section we present the modal EKE flux divergence. First, we present the theoretical framework of the vertical modes. Then, we define the unapproximated expression of the modal EKE flux divergence, which consists of the eddy pressure work (EPW) and the advection of EKE ($AEKE$). Finally, we define the η-based expressions of EPW and $AEKE$.

2.1 Vertical modes

A convenient approach to describe the vertical structure of mesoscale motions is the modal decomposition using traditional vertical modes (Gill, 1982). The vertical structure of the mesoscale EKE reservoir corresponds to the combination of the barotropic and 1^{st} baroclinic modes (Wunsch, 1997; Smith & Vallis, 2001; Venaille et al., 2011; Tedesco et al., 2022), which represents surface-intensified vertical structures energised to the bottom.

The vertical modes ϕ_n for the horizontal velocity ($\mathbf{u}$) and the dynamical pressure (p) are the eigenfunctions solution of the Sturm-Liouville problem (Eq. 1), using linearized free-surface ($|\frac{\partial}{\partial z}\phi_n|_{z=\eta} = |\frac{-\overline{N^2}}{g}\phi_n|_{z=\eta}$) and flat-bottom boundary conditions ($|\frac{\partial}{\partial z}\phi_n|_{z=-H} = 0$) :

$$\frac{\partial}{\partial z}\left(\frac{1}{N^2}\frac{\partial}{\partial z}\phi_n\right) + \frac{1}{c_n^2}\phi_n = 0 \tag{1}$$

with N^2 the time-averaged buoyancy frequency, g the acceleration of gravity and $c_n^2 = \frac{1}{n\pi}\int_{-H}^{\eta} N(\mathbf{x}, z)\ dz$ the eigenvalues of the vertical modes.
The modal base ϕ_n satisfies the orthogonality condition :

$$\int_{-H}^{\eta} \phi_m \phi_n\ dz = \delta_{mn} h \tag{2}$$

with δ_{mn} the usual Kronecker symbol and $h = \eta + H$ the water column depth.
The dynamical variables are projected onto n vertical modes as follows :

$$[\mathbf{u}_n(\mathbf{x}, t), \frac{1}{\rho_0}p_n(\mathbf{x}, t)] = \frac{1}{h}\int_{-H}^{\eta}[\mathbf{u}(\mathbf{x}, z, t), \frac{1}{\rho_0}p(\mathbf{x}, z, t)]\phi_n(\mathbf{x}, z)\ dz \tag{3}$$

with $\mathbf{u}_n$ and p_n the modal amplitudes of the horizontal velocity ($\mathbf{u}$) and dynamical pressure (p) and ρ_0 the reference density value.
The vertical modes are related to horizontal scales via c_n^2, which are good approximations of the Rossby baroclinic deformation radii : $Rd_{n\geq 1} = \frac{c_n}{|f|}$ (Chelton et al., 1998), with f the Coriolis parameter.

2.2 Unapproximated modal *EKE* flux divergence

2.2.1 *EKE flux divergence in the EKE budget*

The modal EKE flux divergence is a term of the modal EKE budget. A comprehensive modal EKE budget has been derived in Tedesco et al. (2022), inspired from the budget derived in the context of internal tides (Kelly, 2016). The modal EKE budget reads as follows:

$$\underbrace{\mathbf{u}_n' \cdot (\rho_0 h \frac{\partial}{\partial_t}\mathbf{u}_n')}_{Time\ rate} + \underbrace{\underbrace{\nabla_H \cdot \int_{-H}^{\eta} \mathbf{u}_n' p_n' \phi_n^2\ dz}_{Eddy-pressure\ work\ (EPW)} + \underbrace{\frac{\rho_0}{2}\nabla_H \cdot \int_{-H}^{\eta} \mathbf{u}_n \phi_n ||\mathbf{u}_n' \phi_n||^2\ dz}_{Advection\ of\ EKE\ (AEKE)}}_{EKE\ flux\ divergence\ (EPW+AEKE)}$$

$$= \sum\left(\underbrace{S_n}_{EKE\ sources} + \underbrace{D_n}_{EKE\ sinks}\right) \tag{4}$$

Terms are time-averaged and the primes indicate fluctuations relative to the time-average. The dynamical pressure ($p(\mathbf{x}, z, t)$) is derived from the *in situ* density ($\rho(\mathbf{x}, z, t)$) from which the background density profile ($\widetilde{\rho}(z)$, defined as the spatial and temporal average of the *in situ* density) has been subtracted.

The EKE flux divergence corresponds to the rate of EKE spatial transport. When integrated over a domain, the EKE flux divergence corresponds to the transport across the domain boundaries. A positive (negative) sign indicates that outgoing (incoming) flux dominate the incoming (outgoing) flux. At equilibrium, the time rate of EKE (Eq. 4) is negligible. The EKE flux divergence is therefore equal to the sum of the EKE sources and sinks accounted for in the right-hand side of the modal EKE budget (S_n and D_n in Eq. 4). A positive (negative) EKE flux divergence thus represents a net EKE source (sink) that is then transported away (has been transported in).

The EKE flux divergence consists of two contributions: the eddy pressure work (EPW; Eq. 4) and the advection of EKE by the mean and eddy flows ($AEKE$; Eq. 4) (Harrison & Robinson, 1978). EPW is the only contribution to the EKE flux divergence in the context of linear theories of internal waves (Kelly et al., 2010, 2012; Kelly, 2016) and of Rossby waves (Masuda, 1978). It is also the main contribution for interior-ocean dynamics (Harrison & Robinson, 1978). $AEKE$ can contribute significantly to the EKE flux divergence and can be equivalent to EPW in regions of high variability (Harrison & Robinson, 1978; Capó et al., 2019; Tedesco et al., 2022).

Here, we study the EKE flux divergence for the mesoscale reservoir over the period 1995-2004. We define the mesoscale EKE flux divergence as the sum of the barotropic ($n = 0$) and 1^{st} baroclinic ($n = 1$) contributions: $EPW_{n=0-1}$ and $AEKE_{n=0-1}$. To simplify notations, we refer to the mesoscale terms as EPW and $AEKE$ in the following. The modeled mesoscale eddy dynamics over the period 1995-2004 is in equilibrium. The smallness of the time rate of EKE (Eq. 4) has been asserted for the period 1995-1999 in Tedesco et al. (2022). It is even smaller for the period 1995-2004 considered in this study.

2.2.2 Contributions to the EKE flux divergence

EPW and $AEKE$ (Eq. 4) can be written as the sum of the contributions of EKE flux ($A + B$ in Eq. 5, 6) and EKE flux interacting with topographic gradients (C in Eq. 5, 6) as follows:

$$EPW = \underbrace{\underbrace{\int_{-H}^{\eta} p'_n\phi_n \nabla_H \cdot (\mathbf{u}'_n\phi_n)\; dz}_{velocity\ divergence\ (\mathbf{A})} + \underbrace{\int_{-H}^{\eta} (\mathbf{u}'_n\phi_n) \cdot \nabla_H (p'_n\phi_n)\; dz}_{work\ of\ eddy\ pressure\ shear\ (\mathbf{B})}}_{EKE\ flux\ (\mathbf{A+B})} + \underbrace{\nabla_H \eta \cdot \left|\mathbf{u}'_n p'_n \phi_n^2\right|_{z=\eta} + \nabla_H H \cdot \left|\mathbf{u}'_n p'_n \phi_n^2\right|_{z=-H}}_{topographic-contribution\ (\mathbf{C})} \tag{5}$$

$$AEKE = \underbrace{\underbrace{\frac{\rho_0}{2}\int_{-H}^{\eta} ||\mathbf{u}'_n\phi_n||^2 \nabla_H \cdot (\mathbf{u}_n\phi_n)\; dz}_{velocity\ divergence\ (\mathbf{A})} + \underbrace{\frac{\rho_0}{2}\int_{-H}^{\eta} (\mathbf{u}_n\phi_n) \cdot \nabla_H ||\mathbf{u}'_n\phi_n||^2\; dz}_{work\ of\ EKE\ shear\ (\mathbf{B})}}_{EKE\ flux\ (\mathbf{A+B})} + \underbrace{\frac{\rho_0}{2}\nabla_H \eta \cdot \left|\mathbf{u}_n\phi_n||\mathbf{u}'_n\phi_n||^2\right|_{z=\eta} + \frac{\rho_0}{2}\nabla_H H \cdot \left|\mathbf{u}_n\phi_n||\mathbf{u}'_n\phi_n||^2\right|_{z=-H}}_{topographic-contribution\ (\mathbf{C})} \tag{6}$$

The EKE flux term ($A + B$; Eq. 5, 6) consists of a velocity divergence contribution (A) and an eddy pressure shear work for EPW (B in Eq. 5) and an EKE shear work for $AEKE$ (B in Eq. 6). From their analytical expressions, it can be deduced that the importance of geostrophic and ageostrophic effects varies between A and B. The velocity divergence contributions (A) mainly account for ageostrophic effects, since geostrophic velocities are horizontally divergent-free. The only geostrophic effects in A are due to geostrophic velocities expressed in the β-plan (Cushman-Roisin & Beckers, 2011). The geostrophic A-contributions acting on EPW and $AEKE$ are thus reduced to EKE flux driven by the β-effect. In the case of EPW (Eq. 5), the β-driven linear EKE flux corresponds to long baroclinic Rossby waves and was assumed by Zhai et al. (2010) to be the primary contributor to EPW, and subsequently to the EKE flux divergence. The work contribution (B) accounts for geostrophic and ageostrophic effects in different proportions for EPW and $AEKE$. For EPW (Eq. 5), the B-contribution is exclusively due to ageostrophic effects. Indeed, geostrophic velocities are orthogonal to the eddy pressure shear resulting in the cancellation of the eddy pressure shear work. For $AEKE$ (Eq. 6), the B-contribution accounts for both geostrophic and ageostrophic effects. Geostrophic velocities are in the same direction than the EKE shear, resulting in a non-null work.

The topographic-contribution (C; Eq. 5,6) acting on EPW and $AEKE$ represents the interactions of EKE flux with topography and sea surface height gradients. It can be reduced to the contribution of topography gradients, which are much larger than η gradients ($||\nabla_H \eta|| = O(10^{-4})||\nabla_H H||$). The analytical expression of C does not allow the contribution of geostrophic or ageostrophic effects to be readily separated.

2.3 Approximated η-based modal EKE flux divergence

In the following, we present the η-based expressions of EPW and $AEKE$ accounting for approximation (i). We also present two other η-based expressions of EPW accounting for approximations (ii) and (iii). The main expressions of EPW and $AEKE$ discussed in this study are listed in Tables 1 and 2.

2.3.1 Approximations (i) of geostrophic velocities ($EPW_{(i)}$ and $AEKE_{(i)}$)

Approximation (i) of geostrophy is required by the use of η to infer the EKE flux divergence. EPW and $AEKE$ are written as $EPW_{(i)}$ and $AEKE_{(i)}$ when using modal geostrophic velocities (Table 1, 2). Modal geostrophic velocities are expressed from η fields, modulated to account for the fraction of the different vertical modes with $\lambda_n = \frac{\eta_n}{\eta}$ and $\alpha_n = \frac{\eta'_n}{\eta'}$, as follows:

$$\mathbf{u}_{g,n}\phi_n = \mathbf{k} \wedge \frac{g}{f}\nabla_H \left(\frac{\phi_n}{|\phi_n|_{z=0}} \lambda_n \eta \right) \tag{7}$$

$$\mathbf{u}'_{g,n}\phi_n = \mathbf{k} \wedge \frac{g}{f}\nabla_H \left(\frac{\phi_n}{|\phi_n|_{z=0}} \alpha_n \eta' \right) \tag{8}$$

Approximation (i) of geostrophy has a larger impact on EPW than on $AEKE$. $EPW_{(i)}$ (Table 1) reduces to a linear EKE flux driven by the β-effect ($A1$) and two topographic contributions, one acting on the β-driven EKE flux ($A2$) and the other acting on geostrophic EKE flux (C). $AEKE_{(i)}$ (Table 2) includes the β-effect (A), the geostrophic EKE shear work (B) and a topographic contribution acting on the geostrophic EKE flux (C).

2.3.2 Approximations (ii) and (iii) ($EPW_{(i,ii)}$ and $EPW_{(i,ii,iii)}$)

The η-based version of EPW defined by Zhai et al. (2010) relies on the additional approximations (ii) and (iii), which are not formally required by the use of η to infer the EKE flux divergence. Approximations (ii) and (iii) therefore lead to approximated versions of the η-based EPW: $EPW_{(i,ii)}$ and $EPW_{(i,ii,iii)}$ (Table 1).

Table 1: Summary of the unapproximated and η-based versions of the eddy pressure work (EPW).

Acronyms	Analytical expressions	Descriptions
EPW	$\underbrace{\nabla_H \cdot \int_{-H}^{\eta} \mathbf{u}'_n p'_n \phi_n^2 \, dz}_{(A+B+C)}$	unapproximated mesoscale eddy pressure work
$EPW_{(i)}$	$\underbrace{-\frac{\beta\rho_0 g^2}{2f^2}\frac{\partial}{\partial x}\left(\frac{\int_{-H}^{\eta}\phi_n^2 \, dz}{\lvert\phi_n^2\rvert_{z=0}}\alpha_n^2\eta'^2\right)}_{\beta-contribution\ (A1)} + \underbrace{\frac{\beta\rho_0 g^2}{2f^2}\frac{\partial H}{\partial x}\frac{\lvert\phi_n^2\rvert_{z=-H}}{\lvert\phi_n^2\rvert_{z=0}}\alpha_n^2\eta'^2}_{\beta-driven\ topographic-contribution\ (A2)}$ $+\underbrace{\frac{\rho_0 g^2}{2f}\nabla_H H \cdot \mathbf{k} \wedge \nabla_H \left(\frac{\lvert\phi_n^2\rvert_{z=-H}}{\lvert\phi_n^2\rvert_{z=0}}\alpha_n^2\eta'^2\right)}_{topographic-contribution\ (C)}$, with $\alpha_n = \frac{\eta'_n}{\eta'}$	unapproximated η-based version of mesoscale eddy pressure work (use of approximation (i))
$EPW_{(i,ii)}$	$\underbrace{-\frac{\beta\rho_0 g^2}{2f^2}\frac{\partial}{\partial x}\left(\frac{\int_{-H}^{\eta}\phi_1^2 \, dz}{\lvert\phi_1^2\rvert_{z=0}}\eta'^2\right)}_{\beta-contribution\ (A1)} + \underbrace{\frac{\beta\rho_0 g^2}{2f^2}\frac{\partial H}{\partial x}\frac{\lvert\phi_1^2\rvert_{z=-H}}{\lvert\phi_1^2\rvert_{z=0}}\eta'^2}_{\beta-driven\ topographic-contribution\ (A2)}$ $+\underbrace{\frac{\rho_0 g^2}{2f}\nabla_H H \cdot \mathbf{k} \wedge \nabla_H \left(\frac{\lvert\phi_1^2\rvert_{z=-H}}{\lvert\phi_1^2\rvert_{z=0}}\eta'^2\right)}_{topographic-contribution\ (C)}$	approximated η- based version of mesoscale eddy pressure work (use of approximations (i) and (ii))
$EPW_{(i,ii,iii)}$	$\underbrace{-\frac{\beta\rho_0 g^2}{2f^2}\frac{\partial}{\partial x}\left(\frac{\int_{-H}^{\eta}\phi_1^2 \, dz}{\lvert\phi_1^2\rvert_{z=0}}\eta'^2\right)}_{\beta-contribution\ (A1)}$	approximated η-based version of mesoscale eddy pressure work defined by Zhai et al. (2010) (use of approximations (i), (ii) and (iii))

Table 2: Summary of the unapproximated and η-based versions of the advection of mesoscale EKE ($AEKE$).

Acronyms	Analytical expressions	Descriptions
$AEKE$	$\underbrace{\frac{\rho_0}{2}\nabla_H \cdot \int_{-H}^{\eta} \mathbf{u}_n\phi_n \|\|\mathbf{u}'_n\phi_n\|\|^2 \, dz}_{(A+B+C)}$	unapproximated advection of mesoscale EKE
$AEKE_{(i)}$	$\underbrace{-\frac{\beta\rho_0 g}{2f^2}\int_{-H}^{\eta} \|\|\mathbf{u}'_{g,n}\phi_n\|\|^2 \frac{\partial}{\partial x}\left(\frac{\phi_n}{\|\phi_n\|_{z=0}}\lambda_n\eta\right) \, dz}_{velocity\ divergence\ (A)} +$ $\underbrace{\frac{\rho_0}{2}\int_{-H}^{\eta} (\mathbf{u}_{g,n}\phi_n)\cdot\nabla_H \|\|\mathbf{u}'_{g,n}\phi_n\|\|^2 \, dz}_{work\ of\ EKE\ shear\ (B)}$ $+\underbrace{\frac{\rho_0}{2}\nabla_H H \cdot \left\|\mathbf{u}_{g,n}\phi_n\|\|\mathbf{u}'_{g,n}\phi_n\|\|^2\right\|_{z=-H}}_{topographic-contribution\ (C)}$, with $\lambda_n = \frac{\eta_n}{\eta}$	unapproximated η-based version of advection of mesoscale EKE (use of approximation (i))

2.3.2.1 Approximation (ii) of sea surface height primarily reflecting the 1^{st} baroclinic mode ($EPW_{(i,ii)}$)

$EPW_{(i,ii)}$ is written as $EPW_{(i)}$, but assumes that modal geostrophic velocities expressed from η reflect only the 1^{st} baroclinic mode (Table 1), using $\alpha_n \sim \alpha_1 \sim 1$, as follows:

$$\mathbf{u}'_{g,1}\phi_1 = \mathbf{k} \wedge \frac{g}{f}\nabla_H \left(\frac{\phi_1}{|\phi_1|_{z=0}}\eta' \right) \tag{9}$$

2.3.2.2 Approximation (iii) of weak topographic-contributions ($EPW_{(i,ii,iii)}$)

$EPW_{(i,ii,iii)}$ ($A1$; Eq. 10) is derived from $EPW_{(i,ii)}$ ($A1 + A2 + C$), assuming that topographic contributions ($A2$ and C) are negligible:

$$EPW_{(i,ii,iii)} = \underbrace{-\frac{\beta\rho_0 g^2}{2f^2}\frac{\partial}{\partial x}\left(\frac{\int_{-H}^{\eta} \phi_1^2 \, dz}{|\phi_1^2|_{z=0}}\eta'^2 \right)}_{\beta-contribution\ (\mathbf{A1})} \tag{10}$$

$EPW_{(i,ii,iii)}$ ($A1$; Table 1) corresponds to a β-driven linear EKE flux acting on the 1^{st} baroclinic mode, which represents the contribution of long baroclinic Rossby waves to the EKE flux divergence. $EPW_{(i,ii,iii)}$ is the approximated η-based version of EPW used in Zhai et al. (2010), which established the paradigm of mesoscale eddies decay at western boundaries.

This study focuses on evaluating the main contributions to EPW and $AEKE$ (which form the EKE flux divergence) in the Agulhas Current region (Figure 1d,e). To do this, we evaluate the impacts of approximations (i), (ii) and (iii) on EPW and of approximation (i) on $AEKE$. We start our analysis by EPW, which is the term explicitly discussed in Zhai et al. (2010). We first evaluate the validity of approximations (ii) and (iii) to infer the η-based EPW (*cf.* section 4). This allows us to define $EPW_{(i)}$ — the unapproximated η-based EPW — which we then use to evaluate the validity of approximation (i) of geostrophy to infer the unapproximated EPW (*cf.* section 5). We next expand our analysis to $AEKE$ (*cf.* section 6). This term dominates the cumulative value of the EKE flux divergence in the WB region (Figure 1e) and is not explicitly discussed in Zhai et al. (2010).

Evaluation of the effects of approximations (i), (ii) and (iii) on EPW provides information on the elements of mesoscale eddy dynamics that invalidate the paradigm of mesoscale eddy graveyard in the Agulhas Current region. In addition, evaluation of the effect of approximation (i) of geostrophy on EPW and $AEKE$ provides information on the possibility of using η to infer EKE flux divergence.

3 Method

In this section, we present and evaluate the regional numerical simulation of the Agulhas Current. We first present the numerical set-up and observations used in this study. We then evaluate the modeled mesoscale eddy dynamics against observations. The modeled mesoscale EKE in the Agulhas Current region has already been evaluated against satellite altimetry data in Tedesco et al. (2022). Here, we evaluate the η-based version of EKE flux divergence defined by Zhai et al. (2010) ($EPW_{(i,ii,iii)}$) derived from our numerical simulation against one derived from observations. The computation of $EPW_{(i,ii,iii)}$ ($A1$; Table 1) requires the computation of vertical modes — based on the time-averaged stratification (N^2) — and η.

3.1 Numerical model

The regional numerical simulation of the Agulhas Current was performed using the Coastal and Regional COmmunity (CROCO) model. It is a free surface model, based on ROMS (Shchepetkin & McWilliams, 2005), which solves the primitive equations in the Boussinesq and hydrostatic approximations using a terrain following coordinate system (Debreu et al., 2012). The numerical simulation is presented in details in Tedesco et al. (2022). The simulation has a horizontal resolution of dx $\sim$ 2.5 km and 60 vertical levels. It encompasses the Agulhas Current region from its source (north of the Natal Bight at 27°S) to the Agulhas Retroflection (at $\sim$ 37°S), from where it becomes the Agulhas Return Current.Boundary conditions are supplied by two lower-resolution grids (dx $\sim$ 22.5 km and 7.5 km, respectively covering most of the South Indian Ocean and its western part).

Vertical modes are derived from the time-averaged stratification over the period 1995-2004, computed from the modeled daily-averaged temperature and salinity.

3.2 Observations

The WOCE (World Ocean Circulation Experiment) climatology provides *in situ* temperature and salinity fields at a global scale for monthly compositing means at the horizontal resolution of 1° (Gouretski & Koltermann, 2004).

Altimetric data are mapped on a regular 1/4°-grid by AVISO (Archiving, Validation and Interpretation of Satellite Oceanographic data) and provide global scale η field for weekly compositing means. We focus on a subset of data over the Agulhas Current region (15°E - 34°E and 27°S - 40°S) for the period 1995-2004.

3.3 Observed and modeled mesoscale $\boldsymbol{EKE}$ sources and sinks from $\boldsymbol{EPW_{(i,ii,iii)}}$

Figure 1a-c shows $EPW_{(i,ii,iii)}$ (Table 1) in the Agulhas Current region calculated from observations and the model. Observed and modeled $EPW_{(i,ii,iii)}$ show patterns in fairly good agreement in the Agulhas Current region. $EPW_{(i,ii,iii)}$ is most intense at the Retroflection and along the Agulhas Return Current (O(0.1-0.5) W m^{-2}), where it has patterns alterning positive and negative signs. It is less intense along the Agulhas Current and in the Subgyre (O(0.01-0.1) W m^{-2}), where it has more uniform patterns.

We define the western boundary (WB) region as extending from north of the Natal Bight ($\sim$ 27°S) to the African tip ($\sim$ 37°S), over a typical width for a western boundary current of about 150 km (black region in Figure 1). In the WB region, $EPW_{(i,ii,iii)}$ is roughly uniformly negative, indicating an EKE sink of cumulative magnitude $O(1)$ GW. This is consistent with the EKE sink emphasised by Zhai et al. (2010) at the western boundary of the South Indian Ocean (poleward of $10°S$).

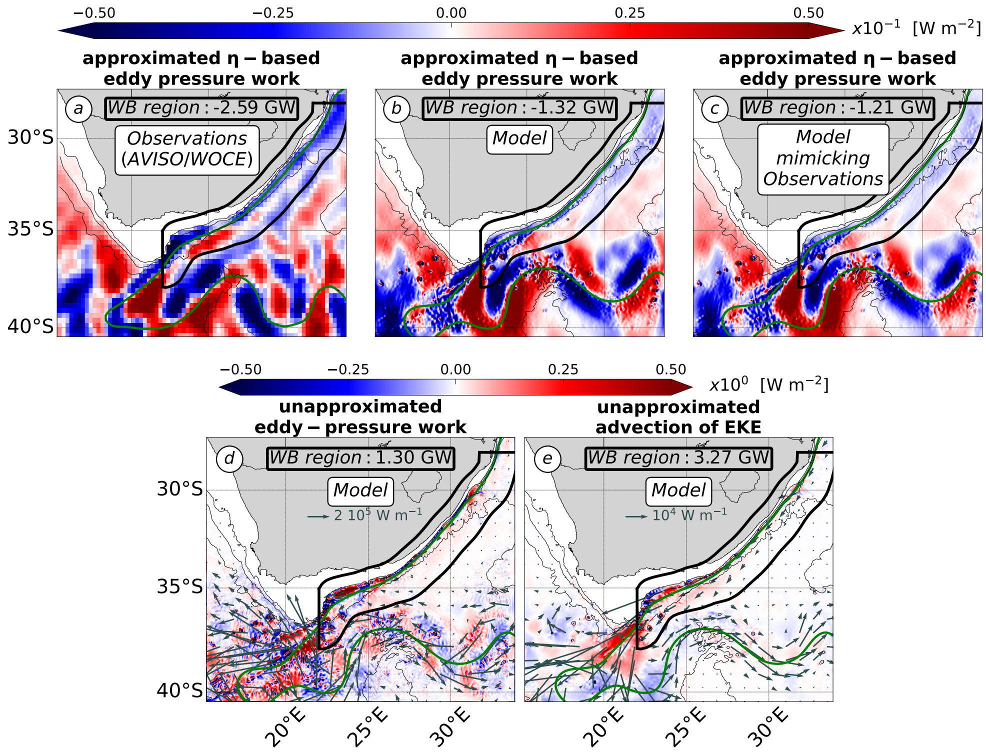

Figure 1: Different versions of the mesoscale EKE flux divergence (formed by eddy pressure work and advection of EKE) [W m^{-2}] in the Agulhas Current region. (a-c) Approximated η-based eddy pressure work performed from (a) observations (AVISO and WOCE data) following Zhai et al. (2010) and (b,c) a numerical simulation (built upon the CROCO model), at (b) the resolution of the simulation (dx $\sim$ 2.5 km) and (c) a coarsened resolution mimicking the resolution of observations.(d,e) Unapproximated model-based (d) eddy pressure work and (e) advection of EKE at the resolution of the simulation (dx $\sim$ 2.5 km). Note the different colorbar ranges between panels (a, b, c) and panels (d, e). Black area denotes the WB region. The cumulative terms in the WB region are in [GW] (10^9 W). Green contours denote the 0.25 m isoline of time-averaged η and black contours denote 1000 m and 3000 m isobaths.

Observed and modeled $EPW_{(i,ii,iii)}$s differ mainly in the magnitude of the EKE sinks that they depict in the WB region. There is about a twofold decrease in the model compared to the observations (Figure 1a-c). The difference in magnitude is not explained by the coarser horizontal resolution of AVISO data (effective horizontal resolution of $O(100)$ km; Chelton et al., 2011) compared to the model (effective horizontal resolution of 25 km; following Soufflet et al., 2016). The twofold decrease in the model is also present when using smoothed modeled η, with a length scale of 100 km to mimic the altimetry data processing done by AVISO (Figure 1c). This indicates that the net EKE sink in the WB region is robust to altimetry data processing and that horizontal scales $< O(100)$ km do not contribute significantly to $EPW_{(i,ii,iii)}$. The difference in magnitude could be explained by too weak a forcing of remotely generated eddies in the model. The numerical simulation is forced at the boundaries by a parent simulation (dx $\sim$ 7.5 km), which resolves mesoscale eddies of scales 50 km–100 km, but underestimate their amplitude. See Appendix A for details of the evaluation of the amplitude of the modeled mesoscale eddy field against satellite altimetry data. This underestimation in the model is likely due to a too weak inverse cascade at smaller scales, which have been shown to substantially energize the mesoscale eddy energy reservoir in the Agulhas Current region (Schubert et al., 2020). Note that the magnitude of the cumulative EKE flux is sensitive to the definition of the WB region. Our definition of the WB region best captures the EKE sink shown by the modeled and observed $EPW_{(i,ii,iii)}$. However, the observed EKE sink extends further south of the WB region (Figure 1a), while the modeled one is fully encompassed by the WB region — with its southern face closely following the 0 W m^{-2} isoline — (Figure 1c,d).

The fairly good agreement between modeled and observed EKE reservoirs (Tedesco et al., 2022) and $EPWs_{(i,ii,iii)}$ (Figure 1a-c), indicates that our numerical simulation reliably represents the mesoscale eddy dynamics, at least as inferred from satellite altimetry data. Our numerical simulation is therefore suitable to evaluate the leading order contribution of the EKE flux divergence, and subsequently to explain the opposing paradigms between η-based and unapproximated diagnoses in this region.

4 Approximated and unapproximated η-based EPWs ($EPW_{(i,ii,iii)}$ and $EPW_{(i)}$)

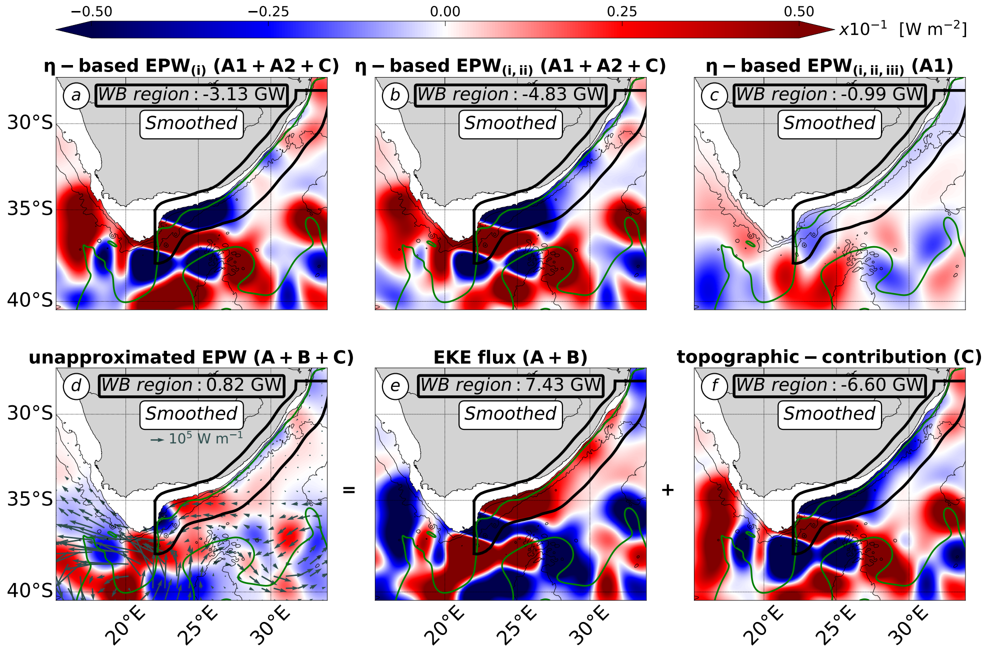

Figure 2: η-based and unapproximated EPWs [W m^{-2}] (Table 1). (a-c) Versions of η-based EPW, including (a) $EPW_{(i)}$, (b) $EPW_{(i,ii)}$, and (c) $EPW_{(i,ii,iii)}$. (d) Unapproximated EPW (A+B+C) split into the contributions of (e) EKE flux (A+B) and (c) topographic-contribution (C). Terms are smoothed with a 75 km-radius Gaussian kernel. (*cf.* Figure 1 for a detailed caption).

In this section, we evaluate the validity of approximations (ii) and (iii) to reliably infer the η-based $EPW_{(i)}$. We first compare $EPW_{(i)}$ (unapproximated η-based EPW) and $EPW_{(i,ii,iii)}$ (approximated η-based EPW used by Zhai et al., 2010). Next, we detail separately the differences due to approximations (ii) and (iii).

Note that most of the figures discussed in the study show smoothed terms (Figures 2, 4, B1). Smoothed terms highlight the large-scale patterns driving the cumulative contributions in the WB region. Smoothing also facilitates comparison between $EPW_{(i,ii,iii)}$ (Figure 1a-c) and the other EPW versions. The smoothing length scale corresponds to a typical mesoscale eddy radius at mid-latitudes (75 km), as inferred from satellite altimetry (Chelton et al., 2011). See Appendix B for details on the sensitivity of EPW to the smoothing length scale.

4.1 Mesoscale EKE sources and sinks from the unapproximated and approximated η-based EPWs ($EPW_{(i)}$ *vs.* $EPW_{(i,ii,iii)}$)

Figure 2a-c shows the different versions of the η-based EPW in the Agulhas Current region ($EPW_{(i)}$, $EPW_{(i,ii)}$ and $EPW_{(i,ii,iii)}$). $EPW_{(i)}$ and $EPW_{(i,ii,iii)}$ have different local patterns and magnitudes in the Agulhas Current region (Figure 2a,c). In the WB region, $EPW_{(i)}$ is predominantly negative, but shows patterns of varying magnitude and sign (Figure 2a). This contrasts with $EPW_{(i,ii,iii)}$ which is almost uniformly negative (Figure

2c). Both EPWs show an EKE sink in the WB region, but that of $EPW_{(i)}$ (-3.13 GW) is significantly larger than that of $EPW_{(i,ii,iii)}$ (-0.99 GW).

The differences between $EPW_{(i)}$ and $EPW_{(i,ii,iii)}$ show that $EPW_{(i,ii,iii)}$ — the approximated η-based version of EPW defined by Zhai et al. (2010) — is not a good estimate of the unapproximated η-based $EPW_{(i)}$ in the Agulhas Current region (Figure 2a,c). This indicates that one or both of the approximations (ii) and (iii) are not valid for inferring the η-based $EPW_{(i)}$.

4.2 Bias due to approximation (ii)

Approximation (ii) of η primarily reflecting the 1^{st} baroclinic mode can bias the η-based $EPW_{(i,ii)}$ in two ways. It can bias the accurate estimate of the contribution of the 1^{st} baroclinic mode to the η-based $EPW_{(i)}$. η does not exclusively reflect eddies (η variance) of the 1^{st} baroclinic mode. In the WB region of the Agulhas Current, the variance of the modeled η accounts for about $16 \pm 4\%$ of the barotropic mode, $38 \pm 4\%$ of the 1^{st} baroclinic mode and $36 \pm 2\%$ of a coupling between the first 10 vertical modes (Figure C1). See Appendix C for details on the partitioning of the η variance into the 10 first vertical modes in the Agulhas Current region. Approximation (ii) may also bias the estimate of the EKE flux divergence for the mesoscale reservoir, because $EPW_{(i,ii)}$ does not include the barotropic contribution. Contributions from the barotropic and 1^{st} baroclinic $EPW_{(i)}s$ can transport EKE in a decoupled (coupled) manner, which would then compensate (accumulate) when considering the EKE flux divergence for the mesoscale reservoir.

$EPW_{(i,ii)}$ and $EPW_{(i)}$ have similar local patterns and magnitudes in the Agulhas Current region (Figure 2a,b). However, their cumulative EKE sinks differ slightly in the WB region. $EPW_{(i,ii)}$ denotes a larger EKE sink (-4.83 GW; Figure 2b) than $EPW_{(i)}$ (-3.13 GW; Figure 2a). $EPW_{(i,ii)}$ includes only the contribution from the 1^{st} baroclinic mode, while $EPW_{(i)}$ can be split into the contributions of the barotropic mode (-1.01 GW in the WB region; not shown) and the 1^{st} baroclinic mode (-2.12 GW in the WB region; not shown).

The large similarities between $EPW_{(i)}$ and $EPW_{(i,ii)}$ patterns (Figure 2a,b) indicate that approximation (ii) is not the main reason for the large discrepancies between $EPW_{(i)}$ and $EPW_{(i,ii,iii)}$ in the Agulhas Current region (Figure 2a,c). However, approximation (ii) leads to an overestimation of (1) the EKE sink in the WB region (overestimation by 154%) and (2) the contribution of the 1^{st} baroclinic mode (overestimation by 228%).

4.3 Bias due to approximation (iii)

The topography acts on $EPW_{(i,ii)}$ ($A1 + A2 + C$; Table 1) via two contributions: the β-driven flux ($A2$) and the geostrophic EKE flux (C). Approximation (iii) of weak topographic contribution is equivalent to assuming that the mesoscale EKE flux ($A1$) has larger spatial variations than that of the topography ($A2$ and C) (Zhai et al., 2010).

$EPW_{(i,ii)}$ and $EPW_{(i,ii,iii)}$ have very different patterns and magnitudes in the Agulhas Current region (Figure 2b,c). These differences are the same as those for $EPW_{(i)}$ and $EPW_{(i,ii,iii)}$ (*cf.* section 4.1). This confirms that approximation (iii) is the one that limits the estimate of the η-based $EPW_{(i)}$ in the Agulhas Current region (Figures 2a,b,c). This also indicates that the topographic contributions ($A2$ and C in $EPW_{(i)}$ and $EPW_{(i,ii)}$; Table 1) dominate the η-based EPWs ($EPW_{(i)}$ and $EPW_{(i,ii)}$; Figures 2a,b). In particular, the topographic contribution to the geostrophic EKE flux (C: -4.54 GW in the WB region; not shown) is the dominant contribution, compared to the β-driven topographic contribution ($A2$: 0.70 GW in the WB region; not shown).

In summary, $EPW_{(i,ii,iii)}$ — the EPW version defined by Zhai et al. (2010) — is not a good estimate of $EPW_{(i)}$ — the unapproximated η-based EPW — in the Agulhas Current region, because approximation (iii) is not valid (Figure 2a-c). In other words, the β-driven linear EKE flux acting on the 1^{st} baroclinic mode ($EPW_{(i,ii,iii)}$) is not the leading order contribution to the η-based $EPW_{(i)}$. $EPW(i)$ ($A1 + A + 2 + C$; Figure 1a) is dominated by interactions between the geostrophic EKE flux of the barotropic and 1^{st} baroclinic modes with topographic gradients (C).

However, the η-based $EPW_{(i)}$ still shows an EKE sink in the WB region (<0; Figure 2a) in contrast with the unapproximated EPW (>0; Figure 1d). This suggests that approximation (i) of geostrophy is the one at the origin of the opposing paradigms supported by η-based and unapproximated EPW.

5 η-based $EPW_{(i)}$ and unapproximated EPW

In this section, we inform about the invalidity of approximation (i) of geostrophy for a reliable inference of the unapproximated EPW. We first evaluate the mesoscale EKE sources and sinks represented by the unapproximated EPW. We then characterize the main contributions to the unapproximated EPW.

5.1 Mesoscale EKE sources and sinks from the η-based $EPW_{(i)}$ and the unapproximated EPW

$EPW_{(i)}$ and EPW show no similarity over the whole Agulhas Current region (Figure 2a,d). In the WB region, they have similar patterns of locally opposite signs. These local differences are reflected in their cumulative values, which amount to an EKE sink (< 0) and an EKE source (> 0), for $EPW_{(i)}$ and EPW respectively. This confirms that approximation (i) of geostrophy is not valid for inferring EPW in the Agulhas Current region (Figure 2a,d).

The unapproximated EPW indicates a source of EKE in the WB region (0.82 GW; Figure 2d). The locally gained EKE is then exported downstream of the Agulhas Current, eventually towards the South Atlantic, or recirculated into the Indian Ocean along the Agulhas Return Current (vector field in Figure 2d). Locally, the unapproximated EPW shows patterns and magnitudes consistent with the documented variability of the Agulhas Current (Lutjeharms, 2006; Tedesco et al., 2022).

Along the northern branch of the WB region (31°E – 26°E), where the Agulhas Current is stable, the unapproximated EPW is weak compared to the rest of the domain and have patterns of contrasting sign (Figure 2d). EPW is negative upstream of the Natal Bight (31°E) and between the Natal Bight and the Agulhas Bank over a narrow band along the straight part of the shelf (26°E-30.5°E). In these areas, EPW (<0) therefore indicates that the eddy dynamics are mainly acting to deplete the mesoscale reservoir. This is consistent with the northern Agulhas Current being stable due to the topographic constraint (Lutjeharms, 2006; Tedesco et al., 2022). EPW is locally positive at the Natal Bight. This is consistent with the punctual generation (4–5 times per year) of Natal Pulses: mesoscale eddies that are the main source of variability of the Northern Agulhas Current (Lutjeharms, 2006; Elipot & Beal, 2015).

Along the southern branch of the WB region (26°E – 23°E), where the shelf curvature increases and the Agulhas Current is unstable, the mesoscale EPW is large and positive (Figure 2d). In this area, EPW shows the largest EKE source of the WB region. This shows that eddy dynamics are mainly energising the mesoscale reservoir there. This is consistent with the highly unstable nature of the southern Agulhas Current and the documented generation of quasi-permanent meanders there (Lutjeharms, Penven, & Roy, 2003; Lutjeharms, Boebel, & Rossby, 2003; Schubert et al., 2021). Note that the mesoscale EPW locally changes sign and becomes negative at the tip of the shelf (24°E – 23°E). There, the shelf curvature decreases and the current is constrained by the topography, locally enhancing EKE dissipation and preventing mixed barotropic-baroclinic instability to trigger (energy conversion terms of barotropic and baroclinic instability are negative, indicating a kinetic energy loss from mesoscale eddies in favor of the mean circulation; Tedesco et al., 2022).

5.2 Main contributions to the unapproximated EPW

Geostrophic effects are not the leading contribution to EPW in the Agulhas Current region. We therefore characterize the main contributions to the unapproximated mesoscale EPW below. We first evaluate the main contributions to the unapproximated EPW and then discuss their range of validity.

5.2.1 Contributions of ageostrophic and topographic effects

The unapproximated EPW ($A + B + C$; Table 1; Figure 2d) consists of an EKE flux contribution ($A + B$; Figure 2b) and a topographic contribution (C; Figure 2c). Both are large and largely compensate in the Agulhas Current region. In the WB region, the cumulative value of EPW is dominated by the positive EKE flux contribution ($A + B$). However, it can be locally dominated by the negative topographic contribution (C), as for example along the straight part of the shelf, where a narrow band of negative EPW is visible (30.5°E – 26°E; Figure 2d).

The EKE flux contribution ($A + B$) and the topographic contribution (C) do not account for geostrophic and ageostrophic effects to the same extent. Approximation (i) of geostrophy limits the estimate of the EKE flux contribution ($A + B$), because the unapproximated $A + B$ (Figure 2e) is very different from its geostrophic analogue ($A1$; Figure 2c). The velocity divergence contribution to the EKE flux (A) accounts for ageostrophic effects and the β-effect. While the eddy pressure shear work (B) exclusively accounts for ageostrophic effects (*cf.* section 2.2.2). The geostrophic EKE flux is thus reduced to a linear β-effect ($A1$; Figure 2c), which we have shown to be negligible for the η-based $EPW_{(i)}$ ($A1 + A2 + C$; Figure 2a).

On the other hand, approximation (i) of geostrophy allows to derive a qualitatively good estimate of the topographic contribution (C). The unapproximated C-contribution (Figure 2f) is similar to the η-based $EPW_{(i)}$ ($A1 + A2 + C$; Figure 2a), which we have seen to be dominated by the geostrophic C-contribution (*cf.* section 4).

Note that the EKE source shown by the unapproximated EPW in the WB region (0.82 GW; Figure 2d) is mainly due to the barotropic EPW (1.56 GW; not shown), while the 1^{st} baroclinic EPW represents an EKE sink (-0.74 GW; not shown) and acts against the barotropic EPW. This emphasises the importance of properly defining the unapproximated mesoscale EPW as the sum of barotropic and 1^{st} baroclinic EPWs. In the case of the unapproximated EPW, both vertical modes compensate each other, while in the case of the η-based $EPW_{(i)}$, both vertical modes amplify each other (*cf. section 4*). The different contributions of barotropic and 1^{st} baroclinic modes to the different versions of EPW is therefore non-trivial.

In summary, the η-based $EPW_{(i)}$ and the unapproximated EPW support opposite paradigms in the Agulhas Current region, because they have different leading order contributions. We first showed that the η-based $EPW_{(i)}$ is dominated by the topographic contribution acting on the geostrophic EKE flux. We then showed that the unapproximated EPW is dominated overall by ageostrophic effects and locally by the topographic contribution. In the following section, we characterize the range of validity for the dominance of ageostrophic effects.

5.2.2 Scale analysis argument for large ageostrophic effects and weak β-effect

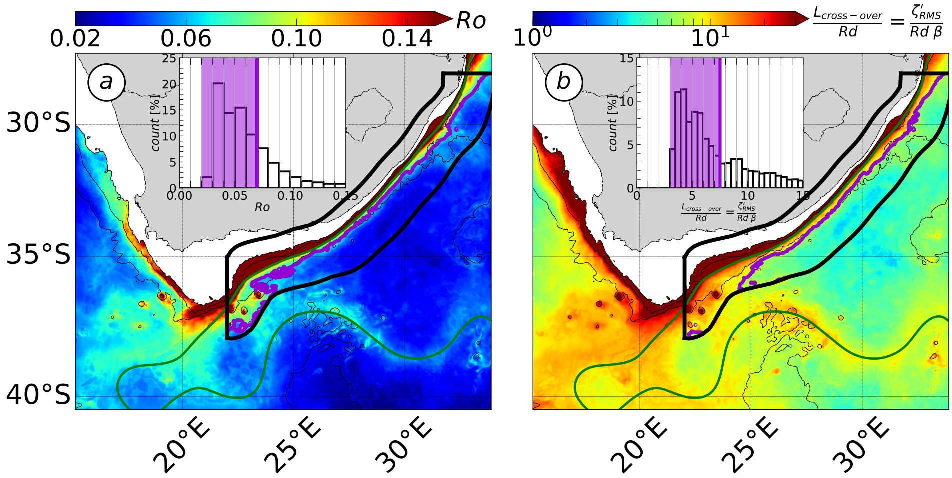

Figure 3: Adimensional metrics measuring the contribution of ageostrophic effects to EPW. (a) Rossby number for mesoscale eddies ($Ro = \frac{\zeta'_{RMS}}{f}$) and (b) ratio between the cross-over scale ($L_{g,ag} = \frac{\zeta'}{\beta}$; Eq. 15) and the characteristics length scale of mesoscale eddies (Rossby deformation radius; Rd). In the barplots, counts of (a) and (b) in the WB region are expressed in [%] and shaded areas show the 70 % percentile. In the maps, purple contours show (a) and (b) 70 % percentiles in the physical space. (*cf.* Figure 1 for a detailed caption)

5.2.2.1 Definition of a cross-over scale

The founding hypothesis of the paradigm of mesoscale eddies graveyard at western boundaries was that long baroclinic Rossby waves are the main contributor to the EKE flux divergence (Zhai et al., 2010). This hypothesis favours one contribution of EPW — the β-effect ($A1$ in $EPW_{(i)}$; Table 1) — over others, which include ageostrophic effects and the topographic contribution. We have seen that for the EKE flux contribution $(A + B)$ acting on the unapproximated EPW (Table 1), ageostrophic effects overcome the β-effect in the WB region of the Agulhas Current (*cf.* section 5). Here, we use a scale analysis to evaluate in which regimes we can expect ageostrophic effects to dominate over the β-effect for the unapproximated EPW.

Ageostrophic effects acting on the EKE flux contribution ($A+B$; Table 1) take the form either of (1) both ageostrophic velocities and pressure ($EPW_{(ag)}$) or (2) coupled ageostrophic velocities to geostrophic pressure ($EPW_{(g,ag)}$). Using quasi-geostrophic scalings of velocity and pressure, we perform the scaling of $EPW_{(ag)}$ (Eq. 11), $EPW_{(g,ag)}$ (Eq. 12), and of the β-effect (Eq. 13), as follows:

$$\left| \int_{-H}^{\eta} \nabla_H \cdot \left(\mathbf{u}'_{ag,n} p'_{ag,n} \phi_n^2 \right) \, dz \right| \sim \frac{Ro^2 U'_g P'_g H}{L} \tag{11}$$

$$\left| \int_{-H}^{\eta} \nabla_H \cdot \left(\mathbf{u}'_{ag,n} p'_{g,n} \phi_n^2 \right) \, dz \right| \sim \frac{Ro U'_g P'_g H}{L} \tag{12}$$

$$\left| \frac{\beta \rho_0 g^2}{2f^2} \int_{H}^{\eta} \frac{\partial}{\partial x} \left(\frac{\phi_n^2}{|\phi_n^2|_{z=0}} \alpha_n^2 \eta'^2 \right) \, dz \right| \sim \frac{\widehat{\beta} P' U'_g H}{\widehat{f}} \tag{13}$$

We use the following adimensionalized variables $\left|\nabla_H, \frac{\partial}{\partial x}\right| \sim \frac{1}{L}$, $\left|\int_{-H}^{\eta} <.> dz\right| \sim H$, $|\beta| \sim \widehat{\beta}$, $|f| \sim \widehat{f}$. Using the expansion of velocity and eddy pressure with Ro the small parameter, we define $\left|\mathbf{u}'_{ag,n}\right| \sim RoU'_g$ and $\left|p'_{ag,n}\right| \sim RoP'_g$, with $Ro = \left|\frac{1}{H}\int_{-H}^{\eta}\left(\frac{\zeta'_{RMS}}{f}\right) dz\right| \sim \widehat{\frac{\zeta'_{RMS}}{f}}$ the vertical average of the root mean square of the normalized relative vorticity for mesoscale eddies ($\zeta' = \partial_x v' - \partial_y u'$). Using geostrophy, we define $|p'_{g,n}| \sim P'_g \sim \rho_0 \widehat{f} U'_g L$. Using the hydrostatic approximation and geostrophy, we define $\left|\frac{\phi_n^2 \alpha_n^2 \eta'^2}{|\phi_n^2|_{z=0}}\right| \sim \frac{P'_g U'_g L \widehat{f}}{\rho_0 g^2}$.

The scale analysis is used to define two cross-over scales ($L_{g,ag}$ in Eq. 15 and L_{ag} in Eq. 14), at which the contributions to EPW of the two forms of ageostrophic EKE flux ($EPW_{(g,ag)}$ and $EPW_{(ag)}$) have the same order of magnitude as the contribution of the β-effect:

$$\frac{(11)}{(13)} = \frac{Ro^2 \widehat{f}}{L\widehat{\beta}} = \frac{\widehat{\zeta'_{RMS}}^2}{L\widehat{f}\widehat{\beta}} = \frac{L_{ag}}{L}, \text{ with } L_{ag} = \frac{\widehat{\zeta'_{RMS}}^2}{\widehat{f}\widehat{\beta}} \tag{14}$$

$$\frac{(12)}{(13)} = \frac{Ro\widehat{f}}{L\widehat{\beta}} = \frac{\widehat{\zeta'_{RMS}}}{L\widehat{\beta}} = \frac{L_{g,ag}}{L}, \text{ with } L_{g,ag} = \frac{\widehat{\zeta'_{RMS}}}{\widehat{\beta}} \tag{15}$$

$L_{g,ag}$ is the ratio of the eddy vorticity and of the β parameter (Eq. 15). $L_{g,ag}$ is greater than L_{ag} if the eddy Rossby number is <1, which is the case for mesoscale eddies. $L_{g,ag}$ will thus generally impose the most restrictive condition. Note that the definition of the cross-over scales is not unique. An equivalent definition involving the Rhines scale can be defined using another scaling of the eddy Rossby number($Ro = \frac{U'}{fL}$). See appendix D for details on the alternative definition of $L_{g,ag}$ for the mesoscale EPW in the Agulhas Current region.

5.2.2.2 *Cross-over scale performed in the Agulhas Current region*

We compare $L_{g,ag}$ (Eq. 15) with the characteristic length scale of mesoscale eddies — the Rossby deformation radius (Rd) of about 30 km in the region of the Agulhas Current — (Figure 3). The typical values of Ro confirm that mesoscale eddies are mainly geostrophic in the WB region (Ro in $O(0.02–0.07)$ in 70% of the WB region and Ro in $O(0.07–0.65)$ at the inner front; Figure 3a). However, the typical values of $L_{g,ag}$ show that coupled geostrophic-ageostrophic effects dominate over the β-effect at mesoscale ($L_{g,ag}$ in $O(3–7)Rd$ in 70% of the WB region and $L_{g,ag}$ in $O(7–19)Rd$ at the inner front; Figure 3b). On the other hand, the purely ageostrophic effects are weaker than the contribution of the β-effect (L_{ag} in $O(0.1–0.5)Rd$ in the WB region; not shown).

Typical values of $L_{g,ag}$ (Eq. 15) are about $O(105\text{-}256)$ km in the region of the Agulhas Current (not shown). This sets the upper limit of the scale range where coupled geostrophic-ageostrophic effects are expected to dominate over the β-effect. This scale range is consistent with the result of the idealized numerical simulations shown in Zhai et al. (2010), where an eddy of 500 km-diameter was used to illustrate the validity of the approximated η-based version of EPW.

In summary, approximation (i) of geostrophy is not valid to infer the unapproximated EPW in the Agulhas Current region, because the coupled geostrophic-ageostrophic EKE flux overall dominate the EPW at the mesoscale range (105 km>L> $Rd \sim 30$ km). We evaluate in the next section, the use of approximation (i) of geostrophy to infer $AEKE$ (Table 2), the nonlinear component of EKE flux divergence.

6 η-based $AEKE_{(i)}$ and unapproximated $AEKE$

We first evaluate the mesoscale EKE sources and sinks represented by the η-based and the unapproximated $AEKE$. We then characterize the main contributions of the two $AEKE$s.

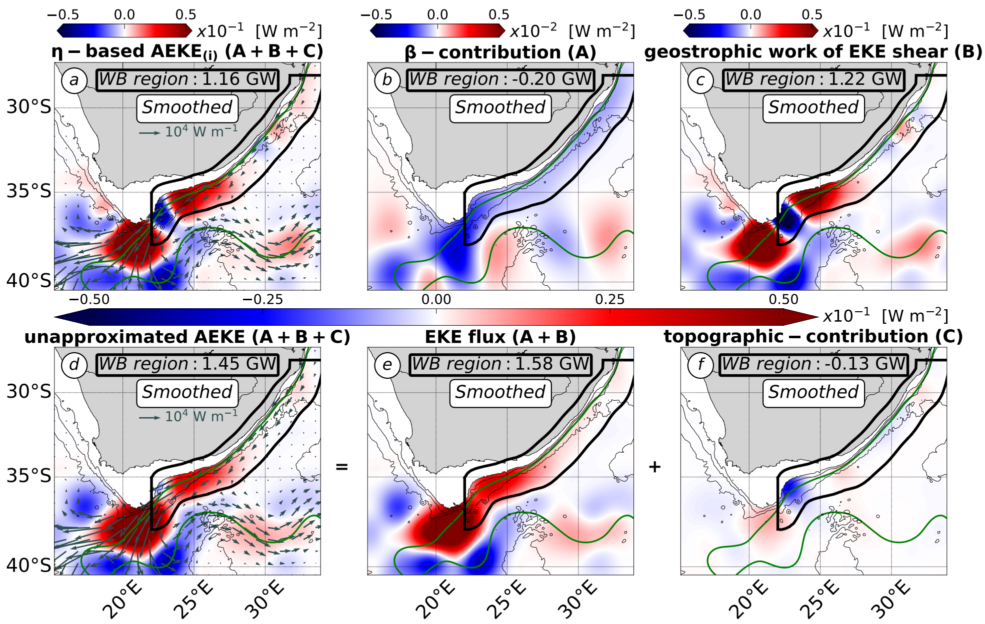

Figure 4: η-based $AEKE_{(i)}$ and unapproximated $AEKE$ [W m^{-2}] (Table 2). (a) η-based $AEKE_{(i)}$ $(A+B+C)$ split into the contributions of (b) β-effect (A) and (c) work of EKE shear (B). (d) Unapproximated $AEKE$ $(A+B+C)$ split into the contributions of (e) EKE flux $(A+B)$ and (f) topographic-contribution (C). (a,d) Vector fields show (a) geostrophic EKE flux ($\frac{\rho_0}{2}\int_{-H}^{\eta} \mathbf{u}_{g,n}\phi_n||\mathbf{u}'_{g,n}\phi_n||^2\ dz$, with $n=0-1$) and (b) unapproximated EKE flux ($\frac{\rho_0}{2}\int_{-H}^{\eta} \mathbf{u}_{n}\phi_n||\mathbf{u}'_{n}\phi_n||^2\ dz$, with $n=0-1$) [W m^{-1}]. Note the different colorbar ranges between (b) and the other panels. All terms are smoothed with a 75 km-radius Gaussian kernel. (*cf.* Figure 1 for a detailed caption).

6.1 Mesoscale EKE sources and sinks from the η-based $AEKE_{(i)}$ and the unapproximated $AEKE$

Figure 4a,d shows the η-based $AEKE_{(i)}$ and unapproximated $AEKE$ in the Agulhas Current region. In the WB region, $AEKE_{(i)}$ and $AEKE$ are in fairly good agreement. Both $AEKE$s show a net EKE source (>0; Figure 4a,d). The η-based $AEKE_{(i)}$ accounts for 73% of the cumulative EKE source shown by the unapproximated $AEKE$ (the remaining 27% being accounted for by ageostrophic effects). The locally gained EKE is then exported out of the WB region, eventually into the South Atlantic Ocean or recirculated in the South Indian Ocean (vector field in Figure 4a,d). The large similarities between $AEKE_{(i)}$ and $AEKE$ indicate that approximation (i) of geostrophy is valid for qualitatively inferring $AEKE$.

The two $AEKE$s show patterns and magnitudes consistent with the documented variability of the Agulhas Current (Lutjeharms, 2006; Tedesco et al., 2022). Along the northern branch of the WB region (31°E – 26°E), where the Agulhas Current is stable, both $AEKE$s are weak (one order of magnitude smaller than in the rest of the domain; Figure 4a,d). Along the southern branch of the WB region (26°E – 23°E), both $AEKE$s are large and generally positive where the shelf curvature increases and the current is documented to be unstable (Lutjeharms, 2006; Tedesco et al., 2022) (Figure 4a,d). In this area, the $AEKE$s indicate that the eddy dynamics mainly act to energise the mesoscale reservoir, similar to the unapproximated EPW (Figure 2d). Note that $AEKE_{(i)}$, and $AEKE$ in a lesser extend, locally change sign and becomes negative at the tip of the shelf (24°E – 23°E), where the topographic constraint on the current is large. This local magnitude difference between the EKE sinks shown by $AEKE_{(i)}$ and $AEKE$ suggests that ageostrophic effects substantially contribute to the mesoscale eddy dynamics at this location.

6.2 Main contributions to the η-based $AEKE_{(i)}$

The η-based $AEKE_{(i)}$ ($A + B + C$; Table 2; Figure 4a) consists of a geostrophic EKE flux contribution ($A + B$; Figures 4b,c) and a topographic contribution acting on the geostrophic EKE flux (C; not shown), which are of different importance in the Agulhas Current region. The geostrophic $A + B$-contribution accounts for 61% of the net $AEKE_{(i)}$, while the geostrophic topographic contribution accounts for the remaining 39% . Within the geostrophic EKE flux ($A + B$), the geostrophic EKE shear work (B) is the main contribution (Figure 4c). The geostrophic EKE shear work (B; Figure 4c) has locally similar patterns and magnitudes than $AEKE_{(i)}$ ($A + B + C$; Figure 4a) in the Agulhas Current region. The velocity divergence contribution (A) corresponds to a negligible nonlinear β-effect (Figure 4b). It represents a weak EKE sink in the WB region (<0; Figure 4b), similar to its linear analogue acting on $EPW_{(i)}$ ($A1$; Figure 2c). In a nutshell, the η-based $AEKE_{(i)}$ ($A + B + C$; Table 2) is dominated by geostrophic effects in the form of the EKE shear work (B).

6.3 Main contributions to the unapproximated $AEKE$

Similar to the η-based $AEKE_{(i)}$, the unapproximated $AEKE$ ($A + B + C$; Table 2) consists in an EKE flux contribution ($A + B$) and a topographic contribution (C), which are of different importance in the Agulhas Current region. In the WB region, $AEKE$ ($A + B + C$; Figure 4d) is overall dominated by the positive EKE flux contribution ($A + B$; Figure 4e), except at the shelf tip (24°E – 23°E) where it is locally dominated by the negative topographic contribution (C; Figure 4f).

The EKE flux contribution ($A + B$) and the topographic contribution (C) do not account for geostrophic and ageostrophic effects in the same proportions. Approximation (i) of geostrophy allows to infer a qualitative estimate of the patterns of the EKE flux contribution ($A + B$; the leading order contribution of $AEKE = A + B + C$). However, note that the ageostrophic effects acting on A and B are significant. The geostrophic EKE flux ($A + B$; Figure 4b,c) underestimates the EKE source shown by the unapproximated analogue ($A + B$; Figure 4e) (underestimation of 35%).

On the other hand, approximation (i) of geostrophy limits the estimation of the patterns and magnitude of the topographic contribution (C; a secondary contribution to $AEKE = A + B + C$). Geostrophic and unapproximated C-contributions have cumulative values of opposite sign in the WB region (geostrophic C: 0.65 GW, not shown and unapproximated C: -0.38 GW in Figure 4f). This indicates that the topographic contribution (C) acting on $AEKE$ is largely influenced by ageostrophic effects.

Note that the EKE source shown by the unapproximated $AEKE$ (2.29 GW; Figure 4d) is due to the accumulation of the barotropic $AEKE$ (0.79 GW; not shown) and 1^{st} baroclinic $AEKE$ (1.50 GW; not shown). This suggests that the mesoscale $AEKE$ could be approximated from the contribution of the 1^{st} baroclinic mode. Similar contributions of the barotropic and 1^{st} baroclinic modes are found for the η-based $AEKE_{(i)}$ (mesoscale $AEKE_{(i)}$: 1.67 GW in Figure 4a and barotropic $AEKE_{(i)}$: 0.57 GW and 1^{st} baroclinic $AEKE_{(i)}$: 1.10 GW; not shown).

In summary, the η-based $AEKE_{(i)}$ and the unapproximated $AEKE$ support similar paradigms in the Agulhas Current region, because geostrophic effects are a major contributor to $AEKE$ (via the EKE shear work B). However, the accurate estimation of its magnitude using η is less reliable. Indeed, ageostrophic effects also make a significant contribution to $AEKE$ $(A + B + C)$, via all its sub-contributions (A, B and C).

7 Summary and Discussion

In this study, we have investigated the main contributions to the mesoscale EKE flux divergence in the Agulhas Current region. Motivated by opposing η-based and model-based paradigms of mesoscale eddy dynamics, we aimed to evaluate the validity of the approximation (i) of geostrophy to infer the mesoscale EKE flux divergence in this region. Geostrophy is a good approximation for inferring mesoscale eddy velocities, but it is a different matter to use it to infer the EKE flux divergence (a tendency term of the EKE budget representing net EKE sources and sinks for ocean dynamics in equilibrium; Harrison & Robinson, 1978). Our analysis used a regional numerical simulation to evaluate the main contributions of the components of the EKE flux divergence, consisting of the eddy pressure work (EPW) and the advection of EKE ($AEKE$). In this section, we summarise our main findings and discuss their implications for the understanding of mesoscale eddy dynamics.

7.1 On the use of sea surface height (η) to infer the mesoscale EKE flux divergence

7.1.1 Eddy pressure work (EPW)

Based on an approximate calculation of EPW using sea surface height (η), Zhai et al. (2010) showed that western boundaries are mesoscale EKE sinks. The η-based diagnosis of EPW is by definition geostrophic. It reduces to the contribution of long baroclinic Rossby waves (linear β-contribution acting on the 1^{st} baroclinic mode) with additional approximations to (ii) the vertical structures of mesoscale eddies and (iii) the contribution of topography. Our results show that none of the approximations (i), (ii) and (iii) are valid to infer the mesoscale EPW in the Agulhas Current region.

We first showed that the η-based $EPW_{(i)}$ (considering only approximation (i); Table 1) is dominated by a topographic contribution acting on the barotropic and 1^{st} baroclinic modes (Figure 2a-d). While the Rossby waves contribution is negligible ($A1$; Figure 2c). This invalidates the use of approximations (ii) and (iii). We then showed that the unapproximated EPW (Table 1) is dominated overall by the coupled geostrophic-ageostrophic EKE flux and locally by topographic interactions (Figures 2d-f,3b). A scale analysis emphasised that the coupled geostrophic-ageostrophic EKE flux dominates EPW at mesoscale ($L > O(30)$ km), while the β-effect could potentially dominate EPW at larger scales ($L > O(105\text{–}256)$ km).

The dominance of ageostrophic effects explains the opposite paradigms supported by the η-based $EPW_{(i)}$ and the unapproximated EPW in the Agulhas Current region. This also invalidates the use of approximation (i) of geostrophy to infer the mesoscale EPW in this region.

7.1.2 Advection of eddy kinetic energy ($AEKE$)

We have defined and performed an unapproximated η-based version of the $AEKE$ component ($AEKE_{(i)}$; Table 2) in the Agulhas Current region. Our results show that approximation (i) of geostrophy is valid to infer a qualitative mesoscale $AEKE$. Unapproximated $AEKE$ and η-based $AEKE_{(i)}$ support similar paradigms in the Agulhas Current region (Figure 4a,d), because geostrophic effects largely contribute to $AEKE$ ($A+B+C$; Figure 4a), via the term of the EKE shear work (B; Figure 4c).

Our results support the use of η to qualitatively infer the mesoscale EKE source represented by the $AEKE$ component in the western boundary region of the Agulhas Current. This is furtherly supported by the η-based $AEKE_{(i)}$ performed using observations (Figure 5). The observed η-based $AEKE_{(i)}$ (Table 2) is calculated by combining: (1) η measured by satellite altimetry, (2) vertical modes calculated from time-averaged stratification derived from the WOCE climatology, and (3) $\lambda_n = \frac{\eta_n}{\eta}$ (Eq. 2.3.1) and $\alpha_n = \frac{\eta_n'}{\eta'}$ (Eq. 2.3.1) parameters — modulating η according to vertical modes — derived from our numerical simulation at each time step and spatially averaged over the WB region. The observed η-based $AEKE_{(i)}$ shows a mesoscale EKE source in the WB region in fairly good agreement with the modeled η-based $AEKE_{(i)}$ and the modeled unapproximated $AEKE$ (Figures 5a and 4a,d). It shows a large EKE source extending from about 26°E to the Retroflection (20°E), whose cumulative value is 43% and 32% of that of the modeled η-based $AEKE_{(i)}$ and the unapproximated $AEKE$, respectively.

Note that the fairly good qualitative agreement between observed η-based $AEKE$ and modeled versions of $AEKE$ (Figures 5a and 4a,d) highlights a reliable alternative to approximation (ii). The contribution of the barotropic and 1^{st} baroclinic modes to η, and hence to $AEKE$, can be reliably approximated in small regions using spatially averaged model-based partitioning of the modal η.

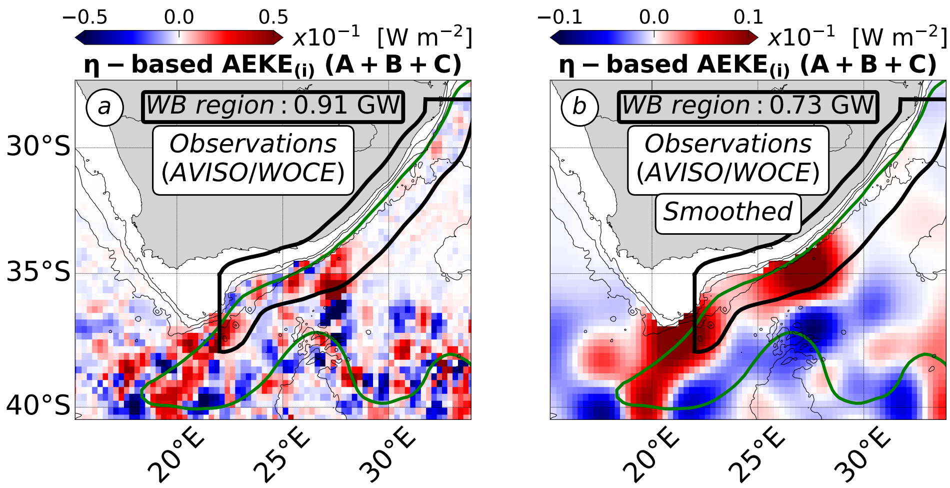

Figure 5: Observed η-based $AEKE_{(i)}$ [W m^{-2}] (Table 2). (a) Unsmoothed and (b) smoothed version of the observed η-based $AEKE_{(i)}$ performed using a combination of satellite altimetry data (AVISO), climatological data (WOCE) and model-based parameter (Eq. 7, 8). For (b), the smoothing radius is 75 km as for Figures 2, 4. Note the different colorbar range between the two panels. (*cf.* Figure 1 for a detailed caption).

7.1.3 Conclusion on the mesoscale EKE flux divergence (EPW and $AEKE$)

Our thorough analysis of the contributions to EPW and $AEKE$ (forming the EKE flux divergence) allows us to conclude on the use of η to infer mesoscale EKE sources and sinks in the Agulhas Current region. $AEKE$ represents the larger cumulative contribution ($AEKE$: 2.29 GW) to the EKE flux divergence in the WB region ($EPW + AEKE$: 3.12 GW; Figures 2d, 4d). Although, the approximation of geostrophy (i) does not allow to infer EPW (Figures 2a,d), it does allow to infer a qualitative estimate of $AEKE$ (73%; Figure 4a,d). This indicates that a qualitative estimate of the EKE flux divergence can be inferred from η, via the $AEKE$ component. In the model, using the η-based $AEKE_{(i)}$ as a proxy for the EKE flux divergence would lead to an underestimation of 46% of the EKE source in the WB region of the Agulhas Current (Figure 4a,d). From observations, however, the underestimation appears to be significantly larger (76%; Figure 5b and 4d).

Further investigation would therefore be required to conclude on the use of η measured by satellite altimetry to reliably infer the magnitude of the EKE source in this region.

Our results support the use of η to infer a qualitative estimate of the mesoscale $AEKE$, and subsequently of the mesoscale EKE flux divergence, but for fundamentally different reasons than Zhai et al. (2010). Zhai et al. (2010) used approximation (i) of geostrophy based on the hypothesis that long baroclinic Rossby waves are the main contributor to the EKE flux divergence. We show in this study that geostrophic effects make a significant contribution to the EKE flux divergence in the Agulhas Current region, via the advection of geostrophic EKE by geostrophic mean and eddy flows ($AEKE$).

7.2 On the mesoscale eddy energy budget at western boundaries

7.2.1 Main contributions acting on the mesoscale EKE flux divergence

The paradigm of a mesoscale eddies graveyard at western boundaries supported by Zhai et al. (2010) relies on long baroclinic Rossby waves (β-effect) as the main contributor to the mesoscale EKE flux divergence. Our results suggest that the mesoscale EKE flux divergence may not be dominated by the β-effect in western boundary regions.

Our scaling analysis showed that the magnitude of the linear β-contribution to EPW depends on metrics that provide a measure of dynamical and regional characteristics (Ro: mesoscale eddy Rossby number and the β parameter, respectively). The β parameter is usually low compared to Ro at mid-latitudes, resulting in a weak β-contribution to EPW. However, the β parameter is larger at low latitudes, suggesting that these regions may be more conducive to a large linear β-contribution to the EKE flux divergence. However, topographic interactions are large at western boundaries regardless of latitude. The topographic contribution may therefore be as large or larger than the β-effect contribution to the EKE flux divergence at western boundaries of all latitudes.

7.2.2 Main sources and sinks of EKE

The positive EKE flux divergence indicates that the mesoscale eddy dynamics in the WB region of the Agulhas Current are locally dominated by processes energising the mesoscale EKE reservoir. A recent study characterized the processes contributing to the mesoscale EKE source in this region (Tedesco et al., 2022). They showed that the local generation of mesoscale eddies — due to barotropic and mixed barotropic-baroclinic instabilities of the Agulhas Current — overcomes the local decay of locally- and remotely generated mesoscale eddies — mainly due to bottom stress and topographically channeled processes — . Our current study complements the process study of Tedesco et al. (2022), by showing (1) that the local mesoscale EKE source is largely redistributed in space by the advection done by geostrophic mean and eddy flows and (2) that this net spatial redistribution can be qualitatively inferred from η fields.

We suggest that the EKE flux divergence at western boundaries may vary with the presence or absence of a western boundary current. However, additional studies of other western boundary regions — with or without a western boundary current and for a broad latitudinal range — would be required to draw conclusions about the mesoscale eddy dynamics at each western boundary. The mesoscale EKE flux divergence could represent an EKE sink in the western boundary regions without a western boundary current, as topographically channeled processes damping mesoscale eddies would locally dominate. This is supported by studies based on *in situ* observations and idealized numerical simulations, for western boundary regions without a western boundary current (Evans et al., 2020; Z. Yang et al., 2021; Evans et al., 2022). The mesoscale EKE flux divergence could represent an EKE source in western boundary regions with a western boundary current, as the local generation of mesoscale eddies would dominate the damping effect of topographic interactions, similar to the Agulhas Current region (Tedesco et al., 2022). This is supported by the intense generation of mesoscale eddies by flow instabilities documented in several western boundary currents (Halo et al., 2014; Kang & Curchitser, 2015; Gula et al., 2015; Y. Yang & Liang, 2016; Yan et al., 2019; Li et al., 2021; Jamet et al., 2021; Tedesco et al., 2022). Furthermore, an exhaustive description of the processes contributing to mesoscale eddy decay in western boundary regions including a western boundary current, should include eddy-mean interactions in addition to topographic interactions (Holloway, 1987; Adcock & Marshall, 2000; Chen et al., 2014; Tedesco et al., 2022).

Appendix A Observed and modeled sea surface height (η) variance in the Agulhas Current region

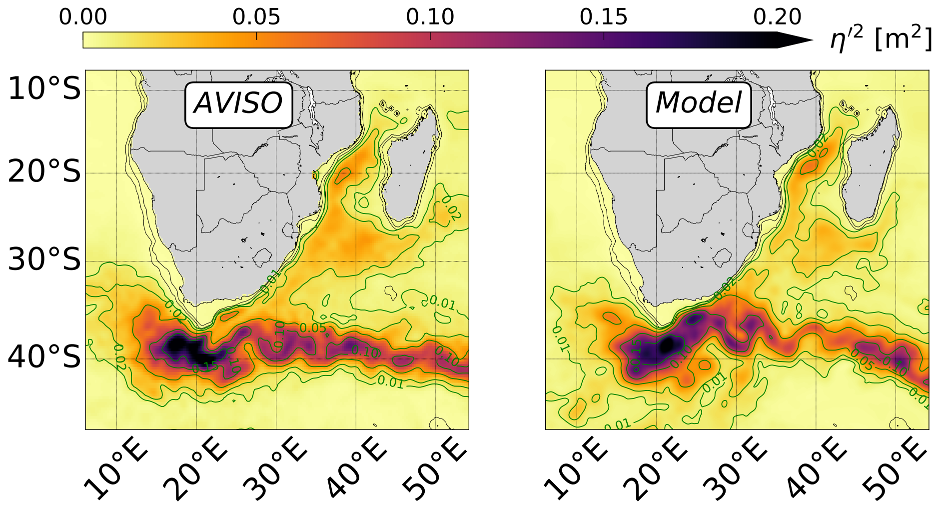

Figure A1: Observed and modeled mesoscale variability at the surface in the Agulhas Current system. η variance (η'^2) [m^2] performed from (a) a numerical simulation (dx $\sim$ 7.5 km) and (b) satellite altimetry data (AVISO). Green contours denote isolines of η variance and black contours denote 300 m and 1000 m isobaths.

The evaluation of the η-based version of the EKE flux divergence defined by Zhai et al. (2010) ($EPW_{(i,ii,iii)}$) in the model and observations, suggest that the modeled mesoscale eddy field might be weaker compared to observations (*cf.* section 3.3). The model of horizontal resolution of dx $\sim$ 2.5 km, used in this study, is forced at the boundaries at each time step by a parent model of dx $\sim$ 7.5 km. The parent simulation resolve mesoscale eddies of scales 50 km–100 km, but may underestimate their magnitude due to a too weak inverse turbulent cascade at smaller scales. This process has been shown to be of importance in the Subgyre regions of the Agulhas Current system (Schubert et al., 2020).

Based on this assumption, we evaluate the modeled mesoscale variability (η variance) simulated by the parent simulation (dx $\sim$ 7.5 km) against satellite altimetry data (Figure A1). The parent simulation covers the western part of the subtropical gyre of the Indian Ocean. The Agulhas Current originates from the lower end of the Mozambique Channel (32.5°E), where it feeds upon the Mozambique Current and the East Madagascar Current. The Agulhas Current flows along the South African coastline to the South African tip (20°E). From there, it Retroflects and become the Agulhas Return Current flowing eastward into the South Indian Ocean.

Modeled η variance represents the variability of the Agulhas Current system in overall good agreement with observations. The Mozambique Current, the East Madagascar Current and the Agulhas Current show moderate value of η variance (O(0.02–0.03) m^2). The Agulhas Retroflection and the Agulhas Return Current show the largest η variance (O(0.05–0.15) m^2). In the context of our study, a relevant difference is the weaker modeled η variance in the Subgyre region (35°E – 45°E and 25°S – 35°S). There, the model shows moderate value of smaller extend than in observations. This confirms that the modeled mesoscale eddies propagating westward through the Subgyre toward the Agulhas Current region have a weaker amplitude than in observations. This supports the weaker amplitude of the EKE sink in the WB region shown by the modeled $EPW_{(i,ii,iii)}$compared to observed one, to be due to a weaker modeled mesoscale eddy field forced at the boundaries.

Appendix B Sensitivity of the unapproximated *EPW* to spatial smoothing

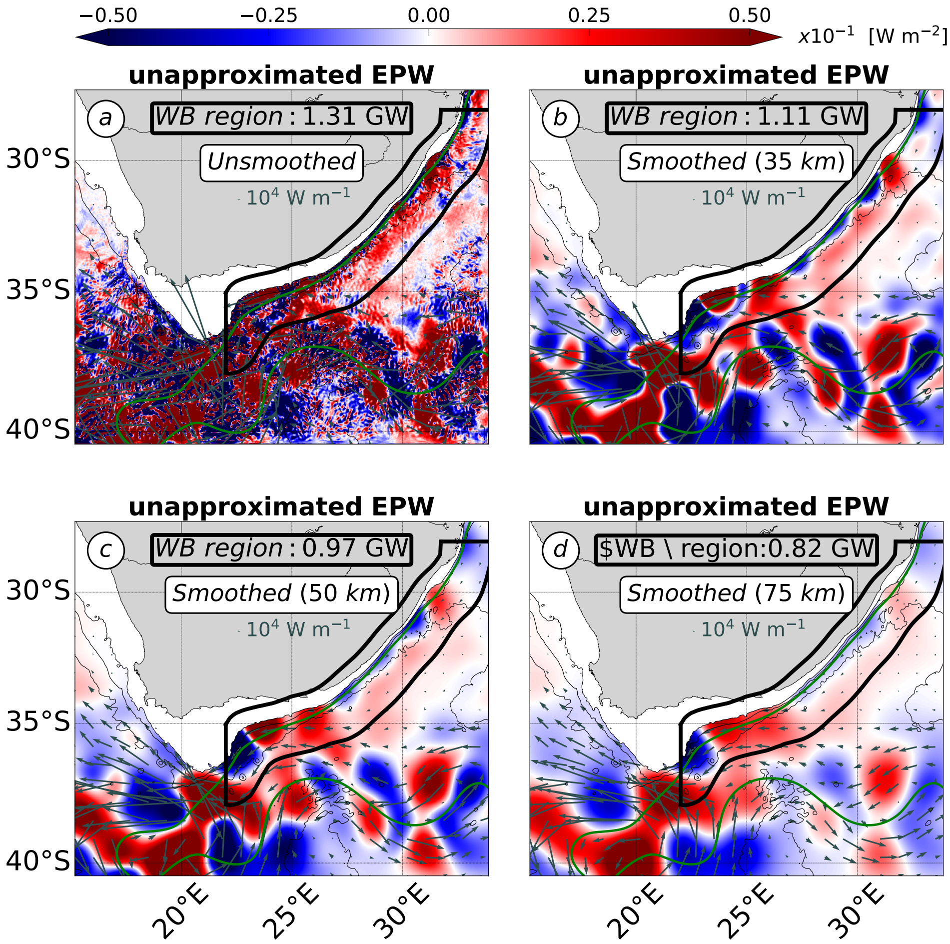

Figure B1: Sensitivity of the unapproximated EPW [W m^{-2}] (Table 1) to spatial smoothing. EPW shown for (a) no spatial smoothing and (b,c,d) spatial smoothing of different radius from (b) 35 km, (c) 50 km to (d) 75 km. Vector fields show the corresponding smoothed EKE flux ($\int_{-H}^{\eta} \mathbf{u}_n' p_n' \phi_n^2 \, dz$, with $n = 0-1$) [W m^{-1}]. (*cf.* Figure 1 for a detailed caption).

The unapproximated EPW (Table 1) is spatially smoothed to emphasise the large-scale patterns driving its cumulative contribution in the WB region (Figure B1). The unsmoothed EPW is characterized by small-scales patterns that are the most intense at topographic features — shelf slope (1000 m isobath), seamounts, canyons, roughness, among others — locally peaking at $O(2.5$ - $10)$ W m^{-2} (Figure B1a). In the WB region, the intense small-scales patterns of the unapproximated EPW are larger by one or two order of magnitude than the unsmoothed $EPW_{(i,ii,iii)}$ ($O(0.01)$ W m^{-2}; Figure 2a). However, the magnitude of the cumulative contribution of EPW (1.31 GW; Figure B1a) is close to the one of $EPW_{(i,ii,iii)}$ (-1.32 GW; Figure 1b) in this region, regardless of the intense small-scale patterns. It indicates that the intense small-scale patterns locally compensate and do not significantly contribute to the cumulative EPW in the WB region.

The sensitivity of the unapproximated EPW to the smoothing is shown using a Gaussian kernel of progressively increasing length scale: from 35 km (the spatially-averaged Rossby deformation radius in region the modeled region) to 50 km and 75 km (two typical mesoscale eddies radii at mid-latitudes; Chelton et al., 2011). The patterns of EPW change with the different smoothing length scales, but the order of magnitude of the cumulative contribution in the WB region is reasonably unchanged ($\leq$ 30%; Figure B1). A similar sensitivity to the smoothing is found for the unapproximated $AEKE$ ($\leq$ 20%; not shown).

In the study, the label 'smoothed' in Figures refers to the Gaussian kernel using a 75 km-radius. The smoothings using 50 km- and 75 km-radius result in fairly close cumulative EPW in the WB region (Figures B1c,d). However, the 75 km-radius smoothing provides smoother patterns, emphasizing the most the large-scale patterns driving the EPW cumulative in the WB region, and facilitating the most its comparison with $EPW_{(i,ii,iii)}$ (Table 1; Figures 1b).

Appendix C Partitioning of sea surface height (η) variance into the barotropic and 9 first baroclinic vertical modes

In order to assess the validity of approximations (ii) and (iii) to infer EPW, we progressively relax the use of the approximations when inferring the η-based EPW term (*cf.* section 4). Relaxing the use of approximation (ii) of η primarily reflecting the 1^{st} baroclinic mode, requires to evaluate the partitioning of the η variance into the different vertical modes ($\alpha_n^2 = \frac{\eta_n'^2}{\eta'^2}$; Eq. 8 in section 2.3.1). η is a 2-dimensional field and cannot be straightforwardly projected onto the vertical mode base. However, the modal coefficient for η (η_n) can be inferred such as: $\eta_n' = \frac{p_n'(z=0)}{\rho_0 g}$, using the modal pressure at z =0 m and the hydrostatic relationship.

The modal expression of the η variance (η'^2) and α_n^2 are defined as follows:

$$\eta'^2 = \sum_{n=0}^{\infty} \eta_n' \sum_{m=0}^{\infty} \eta_m'$$

$$\eta'^2 = \sum_{n=0}^{\infty} \eta_n'^2 + \underbrace{\sum_{n=0}^{\infty} \sum_{m \neq n}^{\infty} \eta_n' \eta_m'}_{Intermodal\ coupling\ (C_{nm})}$$

$$\eta'^2 = \sum_{n=0}^{\infty} \eta_n'^2 + C_{nm} \tag{C1}$$

$$\alpha_n^2 = \frac{\eta_n'^2}{\eta'^2} \text{ and } \alpha_{nm} = \frac{C_{nm}}{\eta'^2} \tag{C2}$$

The modal expression of the variance of η (Eq. C1) involves an intermodal coupling term(C_{nm}). It corresponds to a phase-locked combination of vertical modes at the surface due to the modal correlation in time (Wunsch, 1997; Scott & Furnival, 2012). The degree of the surface modal correlation ($\frac{\sum_{n=0}^{9} \eta_n'^2}{\sum_{n=0}^{9} \eta_n'^2 + C_{nm}}$) is 1.8 in average in our numerical simulation, which is consistent with the 2-3 factor determined at global-scale from *in situ* data (Wunsch, 1997). However, it must be noted that the unapproximated EPW (Table 1) only accounts for the contribution of individual modes ($n = 0$ and $n = 1$). The coupling term C_{nm} is of importance for accurately decomposing η into vertical modes, but it does not contribute to the vertically-integrated form of the mesoscale EKE flux divergence considered in this study. Indeed, EPW involves the orthogonality condition resulting in canceling out the contribution of C_{nm} to EPW.

Using our numerical simulation of the Agulhas Current, we inferred α_n^2 the partitioning of the η variance into the barotropic and 9 first baroclinic modes (Figure C1). The barotropic and 10 first baroclinic modes account for 85-100% of the modeled η variance in the region (not shown).

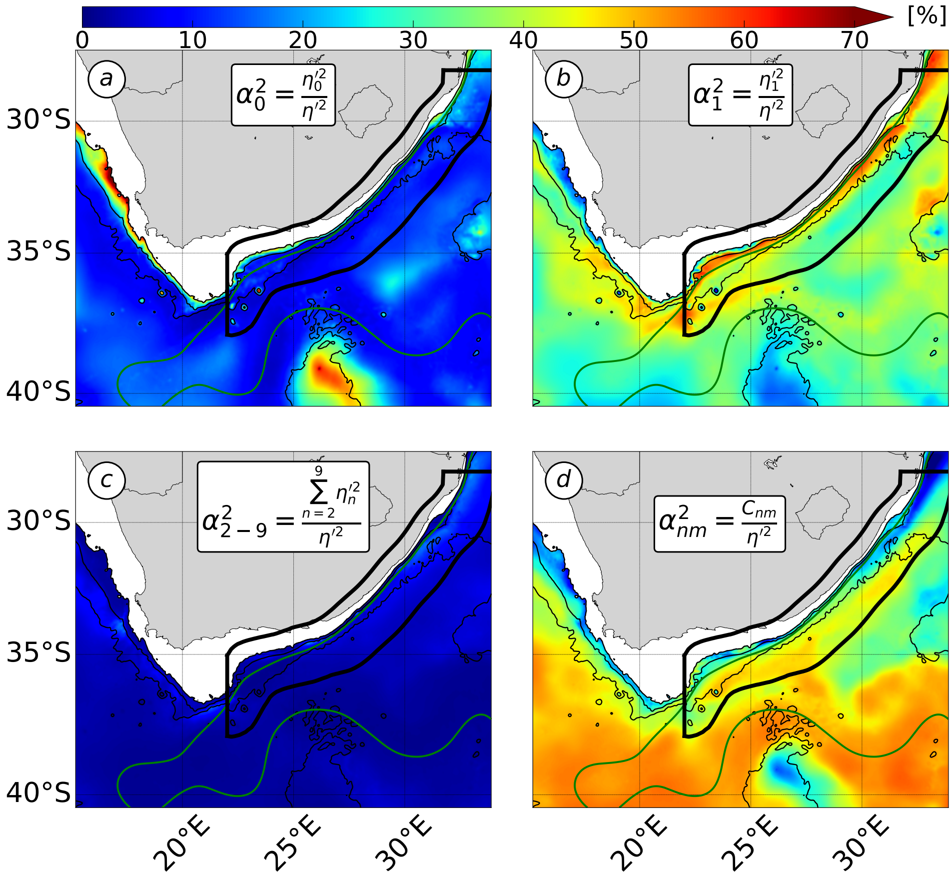

Figure C1: Partitioning of the sea surface height variance into categories of vertical modes ($\alpha_n^2 = \frac{\eta_n'^2}{\eta'^2}$) [%], including (a) the barotropic mode ($n = 0$), (b) the 1^{st} baroclinic mode ($n = 1$), (c) higher baroclinic modes ($n = 2 - 9$) and (d) the intermodal coupling at the surface (C_{nm}). (*cf.* Figure 1 for a detailed caption).

In the WB region, The η variance mainly partitions into the 1^{st} baroclinic mode (38 $\pm$ 2%; Figure C1b) and C_{nm} the intermodal coupling term (36 $\pm$ 2%; Figure C1d). It partitions more weakly, but still significantly into the barotropic mode (16 $\pm$ 4%) (Figure C1a). This is partially consistent with the usual interpretation of η primarily reflecting the 1^{st} baroclinic mode (Wunsch, 1997; Smith & Vallis, 2001). However, it also indicates that the vertical structure of mesoscale eddies — formally represented by the combination of the barotropic ($n = 0$) and 1^{st} baroclinic modes ($n = 1$) (Wunsch, 2007; Smith & Vallis, 2001; Venaille et al., 2011; Tedesco et al., 2022) — can be accurately inferred from η field. This enables us to relax approximation (ii) and compute the unapproximated η-based $EPW_{(i)}$ (defined as the sum of the barotropic and 1^{st} baroclinic contributions) from the modeled η field (*cf.* section 4).

Appendix D Alternative definition of the cross-over scale based on the Rhines scale

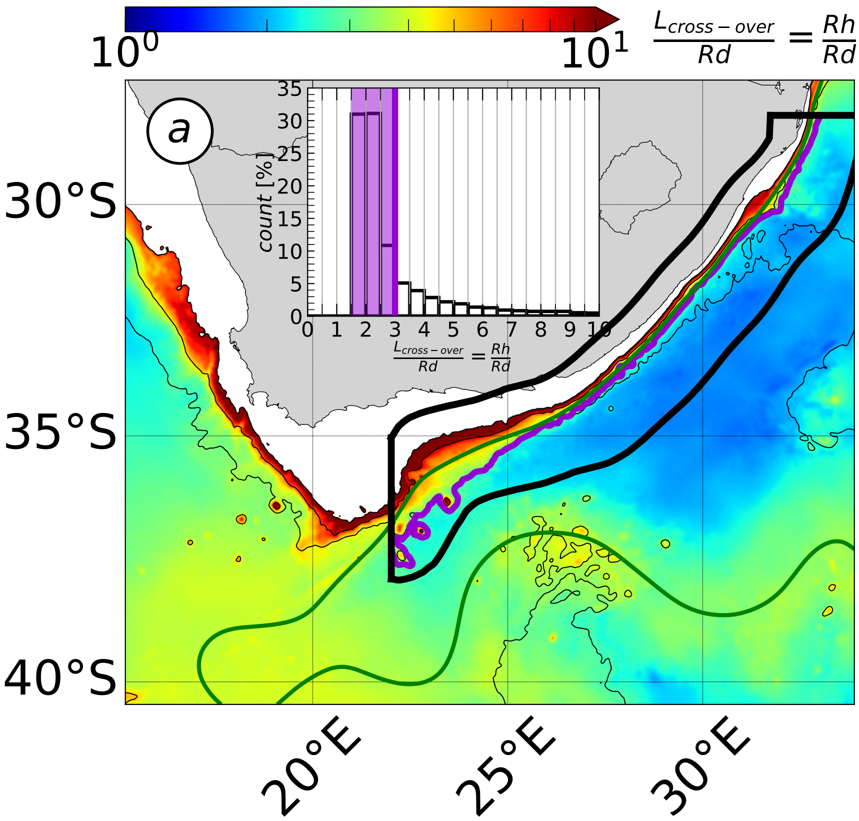

Figure D1: Alternative cross-over scale ($L_{g,ag} = Rh = \frac{1}{H}\int_{-H}^{\eta}\left(\sqrt{\frac{||\mathbf{u'}||}{\beta}}\right) dz$, with $||\mathbf{u'}||$ the magnitude of mesoscale eddies velocity) in the Agulhas Current region. (a) Ratio between the alternative cross-over scale and the characterisitc length scale of mesoscale eddies (Rossby deformation radius; Rd). In the barplot, counts of (a) in the WB region are in [%] and shaded area shows the 70 % percentile. In the map, purple contours show 70 % percentile of (a) in the physical space. (*cf.* Figure 1 for a detailed caption)

Our scale analysis allows us to define a cross-over scale, marking the transition between regimes of large ageostrophic effects and large β-effect acting on the unapproximated EPW (*cf.* section 5.2.2). Using quasi-geostrophic scalings for horizontal velocity and pressure, the cross-over scale is determined by the magnitude of the mesoscale eddies Rossby number (Ro) with respect to the β-parameter (Eq. 15). The definition of the cross-over scale is not unique and changes with the scaling of Ro. Using $Ro = \frac{U'}{fL}$ (instead of $Ro = \zeta'_{RMS} f$ in section 5.2.2), we define an alternative cross-over scale, which corresponds to the Rhines scale ($Rh = \frac{1}{H}\int_{-H}^{\eta}\left(\sqrt{\frac{||\mathbf{u'}||}{\beta}}\right) dz$, with $||\mathbf{u'}||$ the magnitude of mesoscale eddies velocity).

In the quasi-geostrophic theory, the Rhines scale marks the transition from an advectively-dominated (nonlinear) dynamical regime ($Rh >> L$; with L the characteristic length scale of eddies) to a Rossby waves-dominated (linear) dynamical regime ($Rh << L$) (Rhines, 1975). This definition of the cross-over scale shows that evaluating the dominant regime of the mesoscale EPW is therefore similar to evaluating the mesoscale eddies dynamical regime.

In the Agulhas Current region, the typical values of the Rhines scale support the conclusions arising from the version of the cross-over scale presented in the study (Eq. 15 and Figure 3b). The Rhines scale indicates that mesoscale eddies fall in the range of large coupled geostrophic-ageostrophic EPW with respect to the linear β-contribution (Rh in $O(1.5\text{–}3)Rd$ in 70% of the WB region and larger values at the inner front; Figure D1). This results shows that in the WB region of the Agulhas Current, mesoscale eddies fall in the range of large coupled geostrophic-ageostrophic flux — with respect to linear β-effect — as a result of mesoscale eddies being characterized by a nonlinear dynamical regime ($Rh >> Rd$) — and not a linear wave dynamical regime ($Rh << L$) —. Nonlinear dynamics of mesoscale eddies has been characterized from satellite altimetry data, as documented by Chelton et al. (2011).

Open Research Section

WOES36 model outputs are available online at http://dap.saeon.ac.za/thredds/catalog/SAEON.EGAGASINI/2019.Penven/DAILY_MEANS/1_36_degree/catalog.html The AVISO data are available at www.aviso.altimetry.fr, the WOA18 and WOCE climatologies are available at www.nodc.noaa.gov/OC5/woa18/ and https://icdc.cen.uni-hamburg.de/thredds/catalog/ftpthredds/woce/catalog.htm.

Acknowledgments

This work was granted access to the HPC resources of IDRIS under the allocation A0040107630 made by GENCI at Paris, France, and of the HPC facilities DATARMOR of "Pôle de Calcul Intensif pour la Mer" at Ifremer, Brest, France. This work was supported by the Ifremer and the Brittany region for PhD funding. We also gratefully acknowledge support from the French National Agency for Research (ANR) through the projects DEEPER (ANR-19-CE01-0002-01) and the project DIEGO of the CNES/TOSCA SWOT program.

References

Adcock, S., & Marshall, D. (2000). Interactions between geostrophic eddies and the mean circulation over large-scale bottom topography. *Journal of physical oceanography*, *30*(12), 3223–3238.

Capó, E., Orfila, A., Mason, E., & Ruiz, S. (2019). Energy conversion routes in the western mediterranean sea estimated from eddy–mean flow interactions. *Journal of Physical Oceanography*, *49*(1), 247–267.

Chelton, D., Deszoeke, R., Schlax, M., El Naggar, K., & Siwertz, N. (1998). Geographical variability of the first baroclinic Rossby radius of deformation. *Journal of Physical Oceanography*, *28*(3), 433–460.

Chelton, D., Schlax, M., & Samelson, R. (2011). Global observations of nonlinear mesoscale eddies. *Progress in oceanography*, *91*(2), 167–216.

Chelton, D., Schlax, M., Samelson, R., & de Szoeke, R. (2007). Global observations of large oceanic eddies. *Geophysical Research Letters*, *34*(15).

Chen, R., Flierl, G., & Wunsch, C. (2014). A description of local and nonlocal eddy–mean flow interaction in a global eddy-permitting state estimate. *Journal of Physical Oceanography*, *44*(9), 2336–2352.

Cushman-Roisin, B., & Beckers, J.-M. (2011). *Introduction to geophysical fluid dynamics: physical and numerical aspects.* Academic press.

Debreu, L., Marchesiello, P., Penven, P., & Chambon, G. (2012). Two-way nesting in split-explicit ocean models: Algorithms, implementation and validation. *Ocean Modelling*, *49-50*, 1-21.

Ducet, N., Traon, P.-Y. L., & Reverdin, G. (2000). Global high-resolution mapping of ocean circulation from TOPEX/Poseidon and ERS-1 and-2. *Journal of Geophysical Research: Oceans*, *105*(C8), 19477–19498.

Elipot, S., & Beal, L. M. (2015). Characteristics, Energetics, and Origins of Agulhas Current Meanders and Their Limited Influence on Ring Shedding. *Journal of Physical Oceanography*, *45*(9), 2294-2314. doi: 10.1175/JPO-D-14-0254.1

Evans, D., Frajka-Williams, E., & Garabato, A. N. (2022). Dissipation of mesoscale eddies at a western boundary via a direct energy cascade. *Scientific Reports*, *12*(1), 1–13.

Evans, D., Frajka-Williams, E., Garabato, A. N., Polzin, K., & Forryan, A. (2020). Mesoscale eddy dissipation by a 'zoo' of submesoscale processes at a western boundary. *Journal of Geophysical Research: Oceans*, e2020JC016246.

Ferrari, R., & Wunsch, C. (2009). Ocean circulation kinetic energy: Reservoirs, sources, and sinks. *Annual Review of Fluid Mechanics*, *41*.

Gill, A. (1982). *Atmosphere-ocean dynamics (international geophysics series).* academic press.

Gill, A., Green, J., & Simmons, A. (1974). Energy partition in the large-scale ocean circulation and the production of mid-ocean eddies. *Deep sea research and oceanographic abstracts*, *21*(7), 499–528.

Gouretski, V., & Koltermann, K. (2004). WOCE global hydrographic climatology. *Berichte des BSH*, *35*, 1–52.

Gula, J., Molemaker, M., & McWilliams, J. (2015). Gulf Stream dynamics along the Southeastern U.S. Seaboard. *J. Phys. Oceanogr.*, *45*(3), 690-715.

Halo, I., Penven, P., Backeberg, B., Ansorge, I., Shillington, F., & Roman, R. (2014). Mesoscale eddy variability in the southern extension of the East Madagascar Current: Seasonal cycle, energy conversion terms, and eddy mean properties. *Journal of Geophysical Research: Oceans*, *119*(10), 7324–7356.

Harrison, D. E., & Robinson, A. R. (1978). Energy analysis of open regions of turbulent flows—Mean eddy energetics of a numerical ocean circulation experiment. *Dynamics of Atmospheres and Oceans*, *2*(2), 185–211.

Holloway, G. (1987). Systematic forcing of large-scale geophysical flows by eddy-topography interaction. *Journal of Fluid Mechanics*, *184*, 463–476.

Jamet, Q., Deremble, B., Wienders, N., Uchida, T., & Dewar, W. (2021). On wind-driven energetics of subtropical gyres. *Journal of Advances in Modeling Earth Systems*, *13*(4), e2020MS002329.

Kang, D., & Curchitser, E. (2015). Energetics of eddy–mean flow interactions in the Gulf Stream region. *Journal of Physical Oceanography*, *45*(4), 1103–1120.

Kelly, S. (2016). The vertical mode decomposition of surface and internal tides in the presence of a free surface and arbitrary topography. *Journal of Physical Oceanography*, *46*(12), 3777–3788.

Kelly, S., Nash, J., & Kunze, E. (2010). Internal-tide energy over topography. *Journal of Geophysical Research: Oceans*, *115*(C6).

Kelly, S., Nash, J., Martini, K., Alford, H. M., & Kunze, E. (2012). The cascade of tidal energy from low to high modes on a continental slope. *Journal of physical oceanography*, *42*(7), 1217–1232.

Li, J., Roughan, M., & Kerry, C. (2021). Dynamics of interannual eddy kinetic energy modulations in a western boundary current. *Geophysical Research Letters*, e2021GL094115.

Lutjeharms, J. (2006). *The Agulhas Current* (Vol. 2). Springer.

Lutjeharms, J., Boebel, O., & Rossby, H. (2003). Agulhas cyclones. *Deep Sea Research Part II: Topical Studies in Oceanography*, *50*(1), 13–34.

Lutjeharms, J., Penven, P., & Roy, C. (2003). Modelling the shear edge eddies of the southern agulhas current. *Continental Shelf Research*, *23*(11-13), 1099–1115.

Masuda, A. (1978). Group velocity and energy transport by Rossby waves. *Journal of Oceanography*, *34*(1), 1–7.

Müller, P., McWilliams, J., & Molemaker, M. (2005). *Routes to dissipation in the ocean: The 2D/3D turbulence conundrum.* Cambridge University Press Cambridge.

Nikurashin, M., & Ferrari, R. (2010). Radiation and dissipation of internal waves generated by geostrophic motions impinging on small-scale topography: Theory. *Journal of Physical Oceanography*, *40*(5), 1055–1074.

Perfect, B., Kumar, N., & Riley, J. (2020). Energetics of Seamount Wakes. Part I: Energy Exchange. *Journal of Physical Oceanography*, *50*(5), 1365–1382.

Rhines, P. (1975). Waves and turbulence on a beta-plane. *Journal of Fluid Mechanics*, *69*(3), 417–443.

Schubert, R., Gula, J., & Biastoch, A. (2021). Submesoscale flows impact Agulhas leakage in ocean simulations. *Communications Earth & Environment*, *2*(1), 1–8.

Schubert, R., Gula, J., Greatbatch, R., Baschek, B., & Biastoch, A. (2020). The Submesoscale Kinetic Energy Cascade: Mesoscale Absorption of submesoscale Mixed Layer Eddies and Frontal Downscale Fluxes. *Journal of Physical Oceanography*, *50*(9), 2573–2589.

Scott, R., & Furnival, D. (2012). Assessment of traditional and new eigenfunction bases applied to extrapolation of surface geostrophic current time series to below the surface in an idealized primitive equation simulation. *Journal of physical oceanography*, *42*(1), 165–178.

Shchepetkin, A., & McWilliams, J. (2005). The Regional Oceanic Modeling System (ROMS): A split-explicit, free-surface, topography-following- coordinate ocean model. *Ocean Modelling*, *9*, 347-404.

Smith, K., & Vallis, G. (2001). The scales and equilibration of midocean eddies: Freely evolving flow. *Journal of Physical Oceanography*, *31*(2), 554–571.

Soufflet, Y., Marchesiello, P., Lemarié, F., Jouanno, J., Capet, X., Debreu, L., & Benshila, R. (2016). On effective resolution in ocean models. *Ocean Modelling*, *98*, 36–50.

Tedesco, P., Gula, J., Penven, P., & Ménesguen, C. (2022). Mesoscale Eddy Kinetic Energy budgets and transfers between vertical modes in the Agulhas Current. *Journal of Physical Oceanography*.

Venaille, A., Vallis, G., & Smith, K. (2011). Baroclinic turbulence in the ocean: Analysis with primitive equation and quasigeostrophic simulations. *Journal of Physical Oceanography*, *41*(9), 1605–1623.

Wunsch, C. (1997). The vertical partition of oceanic horizontal kinetic energy. *Journal of Physical Oceanography*, *27*(8), 1770–1794.

Wunsch, C. (2007). The past and future ocean circulation from a contemporary perspective. *Geophysical Monograph-American Geophysical Union*, *173*, 53.

Yan, X., Kang, D., Curchitser, E., & Pang, C. (2019). Energetics of eddy–mean flow interactions along the western boundary currents in the North Pacific. *Journal of Physical Oceanography*, *49*(3), 789–810.

Yang, Y., & Liang, X. S. (2016). The instabilities and multiscale energetics underlying the mean–interannual–eddy interactions in the Kuroshio Extension region. *Journal of Physical Oceanography*, *46*(5), 1477–1494.

Yang, Z., X., Z., Marshall, D., & Wang, G. (2021). An Idealized Model Study of Eddy Energetics in the Western Boundary "Graveyard". *Journal of Physical Oceanography*, *51*(4), 1265–1282.

Yankovsky, E., Zanna, L., & Smith, K. (2022). Influences of Mesoscale Ocean Eddies on Flow Vertical Structure in a Resolution-Based Model Hierarchy. *Earth and Space Science Open Archive*, 60. Retrieved from `https://doi.org/10.1002/essoar.10511501.1` doi: 10.1002/essoar.10511501.1

Zhai, X., Johnson, H., & Marshall, D. (2010). Significant sink of ocean-eddy energy near western boundaries. *Nature Geoscience*, *3*(9), 608.